Off-Shell Effects for Top Quark Production at Hadron Colliders.

PAPANASTASIOU, ANDREW,SOFRONIS

Off-Shell Effects for Top Quark Production at Hadron Colliders

Andrew Sofronis Papanastasiou

A thesis submitted to Durham University for the degree of

Doctor of Philosophy

2012

Abstract

A good description of processes involving the production and decay of top quarks is crucial to phenomenology at the Tevatron and LHC. In this thesis, a general method constructed using ideas from Effective Theories is presented, allowing predictions to be made for differential observables that importantly include the effects of non-zero top quark virtuality. Calculations using this method can be significantly simpler than those in standard perturbation theory and its use enables the identification of potentially important structures in the amplitudes. The method is applied to the example of top-pair production for a realistic experimental setup at the Tevatron. A number of observables are studied and an evaluation of off-shell effects is given. The latter tend to be small in general but do become enhanced in regions near kinematical boundaries for distributions that are sensitive to the invariant mass of top quarks.

Contents

List of Figures

Declaration

I declare that no material presented in this thesis has previously been submitted for a degree at this or any other university. The research presented in this thesis has been carried out in collaboration with Dr. Adrian Signer, Dr. Pietro Falgari and Dr. Paul Mellor.

The work in this thesis was funded by an STFC studentship.

Acknowledgements

First and foremost I would like to thank my supervisor, Adrian Signer, for all his guidance, support and advice over these past three years. You have been an inspiring mentor to me and I wish you only the best for the future.

Special acknowledgement must be given to my collaborators Pietro Falgari and Paul Mellor who kindly took time out of their own research to explain many technical aspects relating to this work. I have learnt a great deal from them and for this I am very grateful.

In addition, I would like to thank Gudrid Moortgat-Pick for her support during my first year at Durham and continued interest in my research from afar.

Furthermore, I am thankful to Daniel Maître and Emmanuel Stamou for their valuable comments on a preliminary draft of this thesis.

Many thanks must be extended to my office mates in OC118 - working in the same office as them has been a very enjoyable experience. I am hugely grateful to my collegues Adam Berlie, James Currie, Ilan Fridman Rojas, Katy Morgan and Dave Winn for the many coffee breaks and trips to the pub that kept me sane when work was tough.

I would also like to say a big thank you to Ellie; for putting up with me all these years, for always putting a smile on my face and for all the little things I probably haven't appreciated enough.

Finally, I would like to thank Mum, Dad and Natalie whose constant love and support has played a defining role in getting me to where I am today.

Chapter 1

Introduction

Since the discovery of the top quark by the CDF [1] and D0 [2] experiments at the Tevatron in 1996, the final ingredient of the Standard Model (SM) yet to be found has been the Higgs Boson. The very recent announcements by the Atlas and CMS experiments at CERN indicate the existence of a Higgs-like scalar [3, 4], however much work is still required to establish whether or not this really is the missing piece of the SM. Despite this discovery, the role of the top quark for LHC (and Tevatron) physics still remains very strong. As the heaviest known fundamental particle, it is expected to couple strongly to the Electro-Weak-Symmetry-Breaking (EWSB) sector and can therefore be regarded as a promising avenue to understanding EWSB as well as to potential hints of physics beyond the Standard Model.

The top quark is unique amongst the known coloured particles because, due to its relatively large width, Γ_t, it decays in a timescale smaller than $1/\Lambda_{\mathrm{QCD}}$. As such it provides us with the unique opportunity to study its properties with high precision without having to deal with the unpleasantly difficult to handle non-perturbative effects of hadronization.

At the Tevatron and LHC copious numbers of top quarks are produced. In order to fully exploit this opportunity it is of vital importance to have available as accurate as possible predictions for processes involving tops. The work presented in this thesis attempts to provide an effective method to obtain predictions when the often-made assumption of on-shell top quarks is relaxed.

1.1 The Top Quark in QCD and the Standard Model

Given that the top quark is a coloured particle, and given that we are now well and truly in the 'era of the LHC' which has been aptly termed a 'QCD machine' by some, it is only right that a few words are said about Quantum-Chromodynamics (QCD). Similarly, other parts of the Standard Model of particle physics play crucial roles in shaping the character of the top quark as well as dictating the style of its appearance at collider experiments. QCD and the SM in general have been the subject of a huge body of research and numerous textbooks, the bulk of which is beyond the scope of this work. What follows will be a snippet of some of the important aspects of these theories for the phenomenology of top quarks at hadron colliders.

QCD is a non-abelian quantum-field theory with a local $SU(3)$ symmetry, whose fermions and gauge bosons are the quarks and gluons. It is described by the simple-looking Lagrangian

$$\mathcal{L}_{QCD} = -\frac{1}{4} F^{\mu\nu,a} F^a_{\mu\nu} + \sum_f \bar{\psi}^f_i \left(i\not{D} - M_f \right)_{ij} \psi^f_j \tag{1.1}$$

$$+ \mathcal{L}_{\text{gauge-fixing}} + \mathcal{L}_{\text{Fadeev-Poppov}}, \tag{1.2}$$

where ψ^f_i are fermion fields[1], in the fundamental representation, describing quarks of flavour f carrying colour quantum number $i \in \{r,\, g,\, b\}$ and the sum runs over the possible flavours of quarks. $F^a_{\mu\nu}$ is the gluon field-strength tensor and takes the form

$$F^a_{\mu\nu} = \partial_\mu A^a_\nu - \partial_\nu A^a_\mu + g_s\, f^{abc} A^b_\mu A^c_\nu \tag{1.3}$$

which involves the gauge vector fields A^a_μ, in the adjoint representation, that describe gluons carrying colour a ($a = 1, \ldots, 8$). The covariant derivative is

[1] These are in the mass basis when considering the QCD Lagrangian as part of the full SM Lagrangian.

given by the expression

$$D^{\mu}_{ij} = \delta_{ij}\partial_{\mu} + i\, g_s\, T^a_{ij}\, A^a_{\mu}. \tag{1.4}$$

The matrices T^a_{ij} are the generators of $SU(3)$ in the fundamental representation whilst f^{abc} are the generators in the adjoint representation (and the structure constants of the $SU(3)$ algebra). The strong coupling constant, g_s, present in the covariant derivative allows for the interaction of quarks and gluons. In the work presented here we will assume that all quarks apart from the top quark are massless, leading to some simplification of (1.1).

The terms of (1.2) are required for the correct quantization of the classical QCD Lagrangian (1.1). A consistent definition of the gauge boson propagator is only possible if the bilinear operator in the gauge fields is invertible. This is achieved through the insertion of a gauge-fixing term; a common choice (the Lorentz gauge) being:

$$\mathcal{L}_{\text{gauge-fixing}} = -\frac{1}{2\xi}\left(\partial_{\mu}A^{a,\,\mu}\right)\left(\partial_{\mu}A^{a,\,\mu}\right), \tag{1.5}$$

where ξ is the gauge-fixing parameter. In general, individual diagrams involving gluon propagators will depend on ξ, however in physical, gauge-invariant sets of diagrams this dependence will cancel. The introduction of the gauge-fixing constraint in the functional integral of a non-Abelian gauge theory entails the addition of $\mathcal{L}_{\text{Fadeev-Poppov}}$ to the overall Lagrangian via the Fadeev-Poppov method. For QCD this takes the form

$$\mathcal{L}_{\text{Fadeev-Poppov}} = -\overline{u}^a\,\partial^{\mu}\left(\partial^{\mu}\,\delta^{ab} - g_s\, f^{abc}\, A^c_{\mu}\right) u^b. \tag{1.6}$$

The fields u^a are known as the Fadeev-Poppov ghost fields and do not give rise to physical particles. These appear in perturbative calculations only as internal lines in loop diagrams but serve to cancel unphysical contributions from longitudinal polarizations of gauge bosons. For many more details of this we refer to, for example, the textbooks [5, 6].

The QCD Lagrangian forms only part of the full SM Lagrangian and though QCD is a perfectly good theory on its own, other terms of the full SM should be

activated if important features of top quark physics are to be accounted for. The SM is a renormalizable theory described by a Lagrangian, in four dimensions, invariant under local $SU(3)_c \otimes SU(2)_L \otimes U(1)_Y$ symmetry (here c, L and Y stand for 'colour,' 'isospin' and 'weak-hypercharge' respectively). Some of the key contributions to the SM as far as top quarks are concerned are the quark and lepton weak charged-currents:

$$\begin{aligned}\mathcal{L}_{SM} &\supset \mathcal{L}_W^{\text{quark}} + \mathcal{L}_W^{\text{lepton}} \\ &= -\frac{g_{\text{ew}}}{\sqrt{2}}\left(\mathcal{J}_{\text{q}}^{\mu} W^{\mu} + \mathcal{J}_{\text{q}}^{\mu\dagger} W^{\mu\dagger}\right) - \frac{g_{\text{ew}}}{\sqrt{2}}\left(\mathcal{J}_{\text{l}}^{\mu} W^{\mu} + \mathcal{J}_{\text{l}}^{\mu\dagger} W^{\mu\dagger}\right) \end{aligned} \tag{1.7}$$

where

$$\mathcal{J}_{q,\,l}^{\mu} = \bar{\psi}_M^{q,\,l}\,\gamma^{\mu}\frac{1-\gamma_5}{2}\,V_{MN}\,\psi_N^{q,\,l}. \tag{1.8}$$

Here q and l indicate charged quark and lepton fermion fields, M and N are flavour indices and W^{μ} describes the W-boson field. For quark fields V_{MN} is the Cabibbo-Kobayashi-Maskawa (CKM) matrix which allows for flavour changes between 'up' and 'down' type quarks via the weak interaction. This arises when the fields are rotated from the flavour basis to the mass basis after the spontaneous symmetry-breaking of $SU(2)_L \otimes U(1)_Y$. If right-handed neutrinos are included as part of the SM then a similar non-trivial matrix is present in the lepton current, however, this reduces to the identity if these are not present. It is precisely these weak charged-currents of the SM Lagrangian together with the large value of the top mass that prevent the top quark forming bound states.

From the highlighted parts of $\mathcal{L}_{SM}$ it is possible to derive Feynman rules and construct an order by order perturbation theory expansion in the couplings g_s and g_{ew} for scattering amplitudes describing processes involving top quarks. The expansion in couplings forms an important part of this thesis and will be discussed at length later.

At hadron colliders top quarks are produced either singly or in pairs. As indicated in Figures 1.1 and 1.2, single-top production proceeds via three channels (t-, s- and associated production), whilst top-pair production occurs (at lead-

σ [pb]	Tevatron, 1.96 TeV	LHC, 8 TeV	LHC, 14 TeV
$t\bar{t}$	7.08	234	920
s-channel single-top	0.523	3.79	7.93
t-channel single-top	1.04	56.4	154
associated $t\,W$	0.14	11.1	41.8

Table 1.1: Approximate-NNLO cross-sections of top-pair and s-, t- and associated single-top production at the Tevatron and LHC [7, 8] for $M_t = 173\,\text{GeV}$.

ing order) via quark-anti-quark or gluon-gluon partonic initial states. The work presented in this thesis will be focused on top-pair production, although the formalism discussed in the forthcoming chapters is also applicable to the single-top process. Approximate cross-sections for single-top and top-pair production at the Tevatron and LHC are included in Table 1.1.

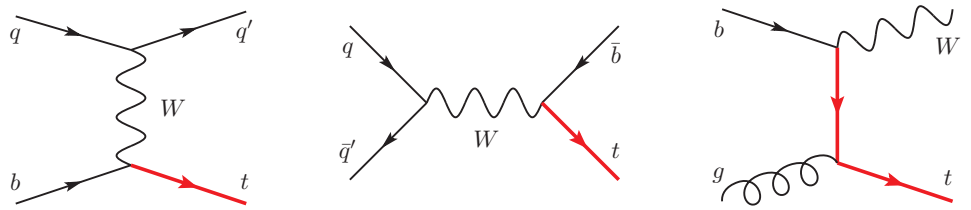

Figure 1.1: Single top production channels at hadron colliders

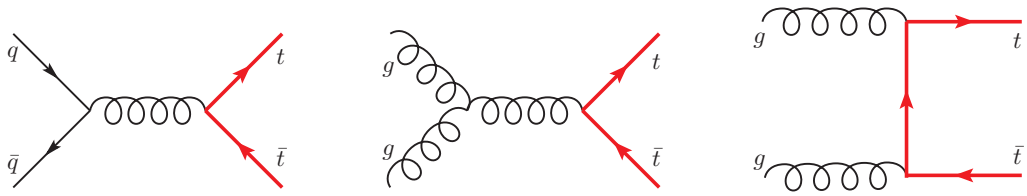

Figure 1.2: Top pair production channels at hadron colliders

The top quark decays before it has a chance to undergo hadronization. In the SM this occurs via the weak current, where the possible decays of the top are: $t \to W^+b$, W^+s, W^+d. Due to the structure of the CKM matrix determined by experimental data, the first of these decays, $t \to W^+b$, occurs almost 100% of

the time, the others being hugely suppressed by the CKM elements V_{ts} and V_{td}. Consequently, it is this dominant decay of the top quark that will be assumed for this thesis (similarly, the anti-top decay $\bar{t} \to W^- \bar{b}$ will be assumed). The W-bosons can either decay leptonically, $W^+ \to l^+ \nu_l$ ($W^- \to l^- \bar{\nu}_l$)[2] or hadronically $W^+ \to u\bar{d}$ (jets) ($W^- \to \bar{u}d$). This splits possible top-pair signals into three channels, the di-lepton channel, the single lepton plus jets channel and the fully hadronic channel, according to whether the W's originating from the top or anti-top quarks decay leptonically or hadronically.

Top quarks are of great interest from a theory point of view and have been studied in great detail, partly driven by their importance to phenomenology at the Tevatron and LHC. Not only are processes involving top quarks important backgrounds to undiscovered physics searches (which typically involve leptons, missing energy plus jets signals), but also, top quark parameters such as its mass, M_t, provide important constraints to parameters of New Physics such as the mass of the Higgs boson.

The relevance of top quark parameters at the fundamental level can be highlighted with a physics example related to the Higgs boson. A key question that may be asked is whether or not the SM, as a renormalizable quantum field theory, can be run up to very high energy scales (around the Plank mass) whilst maintaining stability of the Electro-weak vacuum. This is an entire area of research in itself and we won't delve into details, however, it is worth underlining that the answer to this elementary question depends strongly on the mass of the top quark. In fact, it has been recently pointed out [9] that it is actually the current uncertainty on the top quark mass, more than that on any other parameter of the SM, that is hindering a definite answer!

Fully exploiting the precision at which the experiments at the Tevatron and LHC are capable of measuring top quark properties requires an equivalent or better level of accuracy in the theoretical description of top quark processes. Treating the top quark as heavy as well as unstable is clearly of vital importance. Moreover, the development of theoretical tools where the final states are the decay products of the tops (and not the tops themselves) and where it is possible to impose cuts similar to an experimental analysis is highly desirable. Beginning

[2]The leptonic decay of the W-boson occurs with branching ratio, BR($W^- \to l^- \bar{\nu}_l$) $\simeq 0.108$.

with these requirements it is still possible to make several approximations that ease both the difficulty and complexity of the computations. In particular, when making predictions at Next-to-Leading Order (NLO) in perturbative QCD, the assumption that the top quark is on-shell ($p_t^2 = M_t^2$) is often made. This not only captures a lot of the important physics, but also simplifies the NLO calculations significantly. However, since the LHC will be doing precision top quark physics, it is of great interest to assess the effects of relaxing this assumption and quantifying exactly where the *off-shell* effects play an important role, as well as controlling the impact these may potentially have on measuring parameters linked with the top quark.

1.2 Effective Theory

A persistent undercurrent to much of the material presented here is the notion of efficiently identifying and describing the important features of processes involving unstable top quarks by making full use of the physical information provided. By focusing on the dominant contributions it will be shown that the computations are greatly simplified and also, importantly, much structure to the calculation is revealed.

A key concept in Effective Field Theories (ETs) is the calculation of an *expansion* of scattering amplitudes rather than the full scattering amplitudes, or alternatively working with an expanded form of the Lagrangian or Hamiltonian describing a theory, rather than with the full theory itself. Such an expansion is one in small parameters consisting of ratios of widely-separated scales (momentum scales, mass scales, etc). Admittedly, ETs are limited in validity to regions where these ratios remain small. However, within these regions it is straightforward to make powerful predictions using only the first few terms of the expansion and safely neglect the suppressed higher terms. This makes one's task much easier than when working with the full scattering amplitudes or the full theory. Moreover, the use of ETs can be instructive in highlighting structures or patterns in predictions and calculations that would otherwise perhaps be clouded by the complexity of a full theory computation. This is to be expected as ETs are constructed to describe the key physics in their region of validity.

Motivated by the power as well as the convenience of using ETs, this thesis aims to adopt some ideas and apply them to the computations of quantities relevant for making predictions in a collider physics environment. Making predictions of a fully differential nature, it will be necessary to adapt and further develop such concepts. For processes involving unstable top quarks, the widely-separated scales are M_t and Γ_t and the region which we shall be interested in, the one dominating the cross-section, is the resonant region where $p_t^2 \sim M_t^2$. The key physics captured by an ET approach is that of the factorization of heavy top quark production, propagation and decay subprocesses in addition to the role played by soft gluons in such processes. Much more will be said of all this in the forthcoming chapters.

Talking about an expansion when making predictions for collider processes might sound a little strange at this point since almost all computations of scattering amplitudes are performed in perturbation theory - an expansion in itself. What an ET approach accomplishes here is a provision of a framework for the computation of the series in powers of the small 'kinematic' variables present, essentially achieving a re-arranging or re-organisation of the full perturbation theory amplitudes.

1.3 Thesis Structure

Following this brief introduction, the focus turns to providing the background and presenting the methods used for the study of unstable top-pair production in the resonant phase-space regions. In Chapter 2 we introduce some of the key tools used in the computation of the required scattering amplitudes for this work. Ultra-violet and infra-red divergences arising in perturbation theory are also discussed along with relevant aspects of renormalization. Chapter 3 gives a short excursion into how NLO calculations are realised, with particular attention on the treatment of the real corrections, and how predictions made are related to experimental observables. Details of some of the main methods used in the description of heavy unstable particles are given in Chapter 4, where we also highlight some of the corresponding results and calculations in the literature for top-pair production. In Chapter 5 we explain and discuss at length the main methods developed

to make predictions for processes with unstable heavy particles, presenting the methods using the example of top-pair production at hadron colliders. Here ideas from ETs are developed for use in a differential setup for arbitrary observables. Chapter 6 features the application of the methods of Chapter 5 to a basic experimental setup for the Tevatron, with emphasis on the assessment of the effects of treating the top quarks as off-shell in a broad range of observables. Finally, we arrive at our conclusions and give a short outlook of possible future extensions and improvements to this work in Chapter 7.

Chapter 2

QCD Amplitudes and Field Theory Divergences

In this chapter we describe techniques essential for the computation of scattering amplitudes presented in later chapters. Divergences encountered in higher order corrections are also discussed along with a few aspects of renormalization relevant to the material of this thesis.

2.1 QCD Tools

A plethora of useful tools for calculating field theory amplitudes has been developed over the last two decades. Examples of good reviews on modern approaches can be found in [10, 11]. In this section a few key tools that have been extensively employed throughout the calculations presented in this work are outlined.

2.1.1 Colour Decomposition

Amplitudes in QCD can in general be written as a linear combination of colour factors multiplied by so-called subamplitudes; expressions which are separately gauge invariant and independent of colour,

$$\mathcal{A}_{\text{QCD}} = \sum_i \mathcal{C}_i(a_1, \ldots, a_n)^{\alpha_1 \ldots \alpha_m} A_i(a_1, \ldots, a_n)^{\alpha_1 \ldots \alpha_m}, \tag{2.1}$$

where $a_1, \ldots, a_n$ and $\alpha_1, \ldots, \alpha_m$ are the colour indices of external gluons and (anti-)quarks respectively (see, for example [12]). The colour factors can be written solely in terms of generators of $SU(3)$ in the fundamental representation by replacing structure the constants, f^{abc}, which enter amplitudes through the Feynman rules for gluon 3- and 4- vertices. This can be done by making use of the identity[1]

$$if^{abc} = 2\left[\mathrm{Tr}\left(T^a T^b T^c\right) - \mathrm{Tr}\left(T^b T^a T^c\right)\right] \tag{2.2}$$

with further simplification of colour factors achieved via application of the Fierz Identity:

$$T^a_{ij} T^a_{kl} = \frac{1}{2}\left(\delta_{il}\delta_{jk} - \frac{1}{N_c}\delta_{ij}\delta_{kl}\right). \tag{2.3}$$

Arranging amplitudes in this form is often a convenient way of reducing one's work. By calculating the subamplitudes for a particular ordering of the external partons one can then use the resulting expressions to obtain expressions for all required orderings by permuting and crossing momenta (and helicities - see below).

2.1.2 The Spinor Helicity Method

For processes of interest with massless external states, amplitudes for fixed external-leg-helicity configurations may be calculated. The squared amplitude of the full process is then given by the incoherent sum over all possible amplitudes (interferences between different helicity states are forbidden by Quantum Mechanics). The advantage of calculating matrix elements in this fashion lies in the fact that frequently, out of a potentially large number of helicity configurations, only a small number are actually independent - the rest being obtained from this small set via charge and/or parity flips or momentum swaps. It is also often the case that the individual helicity amplitudes are quite compact which leads to much simpler expressions (and code) for the full matrix elements.

[1]Note: we are using the normalization $\mathrm{Tr}\left(T^a T^b\right) = \frac{1}{2}\delta^{ab}$.

A comprehensive review on this method of calculating scattering amplitudes is given in [12], here we outline only the basic notation.

If $\psi(p)$ is a Dirac Spinor, then its chiral projections are given by

$$\psi_{\pm}(p) := \frac{1}{2}(1 \pm \gamma_5)\psi(p). \tag{2.4}$$

For massless states, helicity is a good quantum number and it is useful to label states with it. The standard notation for fermion states of definite helicity is

$$|p\pm\rangle := \psi_{\pm}(p), \qquad \langle p\pm| := \overline{\psi_{\pm}}(p) \tag{2.5}$$

with spinor products denoted by

$$\langle p\, q\rangle := \langle p - |q+\rangle\,, \qquad [p\, q] := \langle p + |q-\rangle \tag{2.6}$$

and normalization given by

$$\langle p \pm |\gamma^{\mu}|\, p\pm\rangle = 2p^{\mu}. \tag{2.7}$$

The representation of $SU(3)$ polarization vectors with momentum, p, is given by

$$\varepsilon^{\pm}_{\mu}(p,k) = \pm\frac{\langle p \pm |\gamma_{\mu}|\, k\pm\rangle}{\sqrt{2}\,\langle k \mp |p\pm\rangle}, \tag{2.8}$$

where k is an arbitrary light-light vector and represents the freedom to pick a reference momentum when using the axial gauge[2]. In many cases, certain choices of k significantly simplify the helicity amplitudes. Moreover, one is free to pick different k's for different sub-amplitudes, thus making this approach an even more powerful one to calculate scattering amplitudes.

[2]In axial gauge we have $\sum_{\lambda=\pm}\varepsilon^{\lambda}_{\mu}\varepsilon^{\lambda}_{\nu}{}^{*} = -\eta_{\mu\nu} + \frac{p_{\mu}k_{\nu}+p_{\nu}k_{\mu}}{p.k}$.

2.1.2.1 Massive Extension

For massive states, helicity is no longer a good quantum number as it becomes a frame-dependent quantity. However, the spin information carried by massive particles can still be used to construct a helicity basis in a defined frame. This has been used to extend the spinor-helicity method for use when dealing with external massive particles [13]. The latter is particularly useful for this work since top quarks must be treated as massive. The idea is to decompose a massive momentum p ($p^2 = m^2$) into two light-like momenta

$$p = \alpha p^\flat + \beta\eta \tag{2.9}$$

where α and β must satisfy $\alpha\beta = \frac{m^2}{2p^\flat.\eta}$. The choice

$$\alpha = 1, \qquad \beta = \frac{m^2}{2p^\flat.\eta} \tag{2.10}$$

is made in this work (following the choice made in [14, 15]). Following this, u and v spinors may be defined as

$$u_\pm(p, m;\, p^\flat, \eta) := \frac{\not{p} + m}{\langle p^\flat \mp |\eta\pm\rangle} |\eta\pm\rangle\,, \quad \bar{u}_\pm(p, m;\, p^\flat, \eta) := \langle\eta\mp| \frac{\not{p} + m}{\langle\eta \mp |p^\flat\pm\rangle} \tag{2.11}$$

$$v_\pm(p, m;\, p^\flat, \eta) := \frac{\not{p} - m}{\langle p^\flat \mp |\eta\pm\rangle} |\eta\pm\rangle\,, \quad \bar{v}_\pm(p, m;\, p^\flat, \eta) := \langle\eta\mp| \frac{\not{p} - m}{\langle\eta \mp |p^\flat\pm\rangle}. \tag{2.12}$$

The arbitrariness of the momentum η (or $p^\flat$) essentially parametrises the freedom we have to pick a frame in which to define helicity states for massive momenta. The dependence on η must cancel in physical observables.

We finally note that keeping the dependence on $p^\flat$ and η explicit in expressions for helicity amplitudes allows one to relate different massive 'helicity' states via

the relations:

$$u_{\pm}(p,m;\ p^{\flat},\eta) = -\frac{\langle p^{\flat} \pm |\eta\mp\rangle}{m} u_{\mp}(p,m;\ \eta,p^{\flat}),$$

$$\bar{u}_{\pm}(p,m;\ p^{\flat},\eta) = \frac{\langle p^{\flat} \pm |\eta\mp\rangle}{m} \bar{u}_{\mp}(p,m;\ \eta,p^{\flat}),$$

$$v_{\pm}(p,m;\ p^{\flat},\eta) = \frac{\langle p^{\flat} \pm |\eta\mp\rangle}{m} v_{\mp}(p,m;\ \eta,p^{\flat}),$$

$$\bar{v}_{\pm}(p,m;\ p^{\flat},\eta) = -\frac{\langle p^{\flat} \pm |\eta\mp\rangle}{m} \bar{v}_{\mp}(p,m;\ \eta,p^{\flat}).$$

These are particularly useful as they reduce the number of helicity configurations one has to calculate by a factor of two for each massive external parton.

2.1.3 Dimensional Regularization

A convenient way of handling divergences in loop or phase-space integrals required to compute the virtual and real corrections respectively is to isolate or regularise the singularities. The most widely-used method is that of Dimensional Regularization due to 't Hooft and Veltmann [16], in which the space-time dimension is analytically continued to $d = 4-2\epsilon$ dimensions. This renders the loop integrals finite, with the singularities present in $d = 4$ now appearing as poles in ϵ (ϵ^{-2} and ϵ^{-1} poles at NLO).

2.1.3.1 Dimensional Regularization Schemes

Dimensional regularization requires that unobserved momenta be analytically continued away from $d = 4$ dimensions. Therefore, in principle, the gamma matrices, including γ_5, need to be defined in $d \neq 4$ dimensions.

This poses some difficulties as the consistent construction of an anti-commuting γ_5 in d-dimensions is not possible [17]. However, practical schemes do exist where some properties are kept and allow calculations to be made. The accompanying caveat is that, as explained formally in [17], some inconsistencies are introduced. These lead to violations of Ward identities and must be corrected by hand. Con-

sequently, virtual loop or real phase space integrals pick up a dependence on the particular regularization scheme used. However, for physical observables this dependence must disappear. We will parametrize the scheme dependence by η_{sc}, where $\eta_{sc} = 0$ will correspond to the *'t Hooft-Veltmann* (HV) scheme and $\eta_{sc} = 1$ will correspond to the *four dimensional helicity* (FDH) scheme (the use of other schemes is of course also possible). Cancellation of the dependence on η_{sc} in physical quantities will be made explicit where applicable.

Virtual and real corrections are often calculated in different schemes for convenience. Cancellation of η_{sc} in physical quantities requires the use of the same scheme in both sets of corrections and therefore it is necessary to be able to convert expressions between the two schemes. For details of how this is achieved we refer to [18, 19].

2.1.4 The Method Of Regions

Standard methods of evaluating loop integrals such as via Feynman Parametrization or Mellin Barnes are widely reported in the literature and will not be mentioned here. However, one technique that is key to much of the work presented is the method of regions; a method of computing asymptotic expansions of loop integrals that involve hierarchies of scales. The original paper [20] on this method is due to M. Beneke and V.A. Smirnov, whilst its formal mathematical formulation has recently been presented in [21]. The content of the latter goes well beyond anything that will be required here.

The aim of this subsection is to introduce the method via an example relevant for the processes of interest in this thesis. For full details and mathematical rigour we refer to [21].

Closely following the route suggested in the original paper, the steps to applying the method of regions to an integral are as follows. Once the hierarchy of scales has been determined, the loop integration range is split up into regions, according to this hierarchy. In each of these regions the integrand is then Taylor expanded in the relevant small parameters. The integration of the resulting expressions is performed over the *full* integration range and the original integral is given by the sum of terms from each region. It may appear that the last step

will lead to a double counting of regions. This is not the case as integrating the Taylor expansions outside their region of validity leads to scaleless integrals which vanish in dimensional regularization.

On the face of it, this method may appear much more complicated than actually evaluating the original integral. However, integration of the integrands post Taylor expansion is usually much simpler due to fewer scales being present there. Furthermore, if only the first few terms of the asymptotic series of the original integral are required, then these are often reproduced by the sum of the leading term from each region. This turns out to be a significant simplification, and will be the case in this work.

The steps outlined above will now be applied to the example of the scalar integral arising from the top quark decay vertex depicted in Figure 2.1. The conditions on the momenta are $p_b^2 = 0$, $p_W^2 = M_W^2$, $p_t^2 \neq M_t^2$ and $D_t := p_t^2 - M_t^2 \ll M_t^2$. This final condition essentially means the top quark is resonant and provides the hierarchy of scales necessary to apply the method of regions successfully.

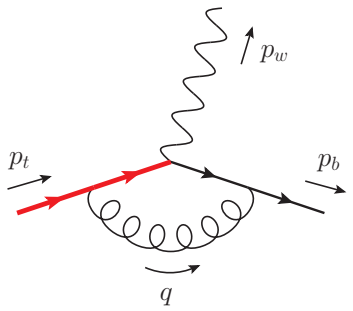

Figure 2.1: Method of Regions example: tWb vertex correction

The original scalar integral is given by [3]

$$I_{\text{full}} = \int [dq] \, \frac{1}{q^2 + i0_+} \, \frac{1}{(q - p_b)^2 + i0_+} \, \frac{1}{(q - p_t)^2 - M_t^2 + i0_+} \tag{2.13}$$

$$= \int [dq] \, \frac{1}{q^2} \, \frac{1}{q^2 - 2q.p_b} \, \frac{1}{q^2 - 2q.p_t + D_t} \tag{2.14}$$

(the $+i0_+$ prescription is assumed in the second line above and for the remainder

[3] $[dq] = e^{\epsilon \gamma_E} \, \Gamma(1 - \epsilon) \, \frac{d^{4-2\epsilon}q}{(2\pi)^{4-2\epsilon}}$

of this section). This can be evaluated directly [22] to give

$$I_{\rm full} = \frac{1}{M_W^2 - p_t^2}\left[\frac{1}{\epsilon}\ln\left(\frac{M_t^2 - p_t^2}{M_t^2 - M_W^2}\right) + \ln^2\left(\frac{M_t^2 - M_W^2}{M_t^2}\right) - \ln^2\left(\frac{M_t^2 - p_t^2}{M_t^2}\right) + {\rm Li}_2\left(\frac{M_W^2}{M_t^2}\right) - {\rm Li}_2\left(\frac{p_t^2}{M_t^2}\right)\right] + \mathcal{O}(\epsilon). \tag{2.15}$$

Expanding this exact expression in $D_t/M_t^2 \ll 1$ yields

$$I_{\rm full} = \frac{1}{M_W^2 - M_t^2}\left[\frac{1}{\epsilon}\ln\left(\frac{-D_t}{M_t^2 - M_W^2}\right) - \frac{\pi^2}{6} + \ln^2\left(\frac{M_t^2 - M_W^2}{M_t^2}\right) - \ln^2\left(\frac{-D_t}{M_t^2}\right) + {\rm Li}_2\left(\frac{M_W^2}{M_t^2}\right)\right] + \mathcal{O}(\epsilon,\ \frac{D_t}{M_t^2}). \tag{2.16}$$

Now we proceed to evaluate the same integral via the Method of Regions. The two regions are identified as

$$\text{hard: } q \sim M_t^2 \quad \text{and} \quad \text{soft: } q \sim D_t,$$

in which the integrand can be expanded respectively as

$$\frac{1}{q^2}\,\frac{1}{q^2 - 2q.p_b}\left(\frac{1}{q^2 - 2q.p_t}\sum_{j=0}^{\infty}\left(\frac{-D_t}{q^2 - 2q.p_t}\right)^j\right) \tag{2.17}$$

(in the hard region $|q^2 - 2q.p_t| \gg |D_t|$) and

$$\frac{1}{q^2}\left(\frac{1}{-2q.p_b}\sum_{k=0}^{\infty}\left(\frac{q^2}{2q.p_b}\right)^k\right)\left(\frac{1}{-2q.p_t + D_t}\sum_{l=0}^{\infty}\left(\frac{q^2}{-2q.p_t + D_t}\right)^l\right) \tag{2.18}$$

(in the soft region $|2q.p_b| \gg |q^2|$ and $|-2q.p_t + D_t| \gg |q^2|$).

The leading terms of the expansion in each region can now be integrated (over the full loop phase-space) to give

$$I_{\rm hard}^{(0)} = \frac{1}{M_W^2 - M_t^2}\left[\frac{1}{2\epsilon^2} + \frac{1}{\epsilon}\ln\left(\frac{M_t^2}{M_t^2 - M_W^2}\right) + \frac{\pi^2}{24} + \ln^2\left(\frac{M_t^2}{M_t^2 - M_W^2}\right) + {\rm Li}_2\left(\frac{M_W^2}{M_t^2}\right)\right] + \mathcal{O}(\epsilon). \tag{2.19}$$

and

$$I^{(0)}_{\text{soft}} = \frac{1}{M_W^2 - M_t^2}\left[-\frac{1}{2\epsilon^2} - \frac{1}{\epsilon}\left(\ln\left(M_t^2\right) - \ln\left(-D_t\right)\right) - \frac{5\pi^2}{24} - \ln^2\left(\frac{M_t^2}{-D_t}\right)\right] + \mathcal{O}(\epsilon). \tag{2.20}$$

As desired, adding the two expressions, $I_{\text{hard}} + I_{\text{soft}}$ (together with some simple manipulations of logarithms), reproduces the leading term in the expansion of I_{full}. It is apparent that compared to the integral, I_{full}, the hard and soft contributions contain additional singularities which must cancel when the two are summed. This is due to the fact that Taylor-expanding in the hard (soft) region results in integrals that are more UV- (IR) divergent because of the additional powers of q in the denominator (numerator) of the integrands. This behaviour will show up again later when the method of regions is applied to a hadron collider process.

2.2 Next-to-Leading Order Calculations and Divergences

Observables such as the differential cross-section can be expanded in the (small) coupling constants of the SM. The focus in the work presented here will be higher order QCD corrections, i.e. the computation of terms in an expansion in the strong coupling constant, $\alpha_s = g_s^2/(4\pi)$,

$$d\sigma = d\sigma^{LO} + \alpha_s\, d\sigma^{NLO} + \alpha_s^2\, d\sigma^{NNLO} + \dots. \tag{2.21}$$

We will confine ourselves to next-to-leading order in perturbation theory, where one is required to calculate the terms $d\sigma^{LO}$ and $d\sigma^{NLO}$ in the series expansion. The main ingredient to $d\sigma^{LO}$ is the Born level matrix element, $|\mathcal{A}^B|^2$, composed of tree-level Feynman diagrams[4]. Radiative corrections to this can be split into two sets, *virtual* and *real* contributions. Virtual corrections contribute to $d\sigma^{NLO}$ via $2\text{Re}\left(\mathcal{A}^B \mathcal{A}^{1-loop\,*}\right)$, where $\mathcal{A}^{1-loop}$ is made of diagrams with closed loop corrections to the Born-level Feynman diagrams. The real corrections enter as $|\mathcal{A}^{real}|^2$ where

[4]This is not strictly true, as there are examples of loop-induced Born-level processes, for example Higgs boson production via gluon fusion.

$\mathcal{A}^{real}$ involves diagrams with an emission of an additional parton from the Born-level configuration.

Both these sets of corrections contain divergences which are potentially disastrous. Fortunately, for properly defined physical observables, the singularities present in the virtual pieces cancel those coming from the real contributions. This key physical result is the subject of the Bloch-Nordsieck [23] and Kinoshita-Lee-Nauenberg [24, 25] theorems.

It should be noted that the virtual terms contain singularities of different origin: Ultra-Violet (UV) singularities from regions where the loop momentum $k \to \infty$ and Infra-Red (IR) singularities from regions where $k \to 0$. The UV singularities are removed by a redefinition of the fields and parameters of the QCD (and EW) Lagrangian in a procedure known as renormalization. Once renormalization has been carried out the IR singularities present in the virtual pieces are exactly cancelled by the singularities in the real corrections (which are of IR origin only).

2.2.1 UV divergences and Renormalization of QCD

When computing loop corrections (tensor) integrals of the form

$$I_n^{\mu_1 \cdots \mu_m}(\{p_i\}) = \int [dk] \, \frac{k^{\mu_1} \ldots k^{\mu_m}}{\prod_{j=1}^{n} \left((k - q_j)^2 - m_j^2 \right)} \tag{2.22}$$

(where $q_i = \sum_{j=0}^{i} p_j$) are often encountered. Taking the limit $k \to \infty$, this takes the form

$$\int d^d k \, \frac{k^{\mu_1} \ldots k^{\mu_m}}{(k^2)^n} \tag{2.23}$$

and the integrand now behaves as $\sim k^{m-2n}$ [5]. When $d + m - 2n \geq -1$, the integral (2.23) has a singularity where $k \to \infty$. Such singularities are the UV singularities commonly found in loop integrals.

Here the process by which UV singularities are removed from scattering amplitudes will be discussed. The focus will be on renormalization of the Lagrangian

[5] $k = \sqrt{k^2} = \sqrt{k^\mu k_\mu}$

of QCD as this is most relevant to this work. The key point is that the parameters and fields in the Lagrangian written down initially (known as the *bare* parameters) do not correspond to the physical or *renormalized* parameters and fields in nature once higher order corrections from perturbation theory are included. Bare parameters have to be related in a systematic way to the corresponding renormalized parameters. It is only predictions making use of finite renormalized quantities that make physical sense and the process of renormalization provides a systematic way of defining these physical quantities.

The bare quantities $A_0^{\mu\,a}$, $\psi_{q,0}$, $m_{q,0}$ and $g_{s,0}$ are related to the renormalized ones via the relations

$$A_0^{\mu\,a} = Z_G^{\frac{1}{2}}\, A_r^{\mu\,a}, \qquad \psi_{q,0} = Z_q^{\frac{1}{2}}\, \psi_{q,r} \tag{2.24}$$

$$m_0 = Z_m\, m_r, \qquad g_{s,0}^2 = Z_{g_s^2}\, g_{s,r}^2 \tag{2.25}$$

with $Z_i = 1 + \delta Z_i$[6]. Equations (2.24) are known as the wavefunction renormalization of the gluon and quark fields, whilst (2.25) describe mass and strong coupling-constant renormalization.

Plugging these equations into the QCD Lagrangian results in

$$\mathcal{L}_{\text{QCD},0} = \mathcal{L}_{\text{QCD},r} + \mathcal{L}_{\text{QCD, ct}} \tag{2.26}$$

where $\mathcal{L}_{\text{QCD},r}$ is identical to $\mathcal{L}_{\text{QCD},0}$ with bare fields and parameters replaced by renormalized ones and $\mathcal{L}_{\text{QCD, ct}}$ contain the effects of the δZ_i in expressions known as *counter-terms*. The latter lead to new Feynman rules which should be included in perturbation theory calculations. An example of how this follows is outlined

[6]Note that δZ_i is $\mathcal{O}(\alpha)$.

here for the gluon-quark vertex:

$$\mathcal{L}_{\text{QCD},0} \supset\ g_{s,0}\, A_0^{\mu\, a}\, \bar{\psi}_{q,0}\, \gamma_\mu\, t^a\, \psi_{q,0} \tag{2.27}$$

$$= Z_{g_s^2}^{\frac{1}{2}}\, Z_G^{\frac{1}{2}}\, Z_q\, g_{s,r} A_r^{\mu\, a}\, \bar{\psi}_{q,r} \gamma_\mu t^a\, \psi_{q,r} \tag{2.28}$$

$$= g_{s,r}\, A_r^{\mu\, a}\, \bar{\psi}_{q,r}\, \gamma_\mu\, t^a\, \psi_{q,r}$$

$$+ \left(\frac{1}{2} \delta Z_{g_s^2} + \frac{1}{2} \delta Z_G + \delta Z_q \right)\, g_{s,r}\, A_r^{\mu\, a}\, \bar{\psi}_{q,r}\, \gamma_\mu\, t^a\, \psi_{q,r} \tag{2.29}$$

These terms yield the standard gluon-quark vertex Feynman rule and, in addition, the vertex counterterm Feynman rule (diagram (c) in Figure 2.2). We note that at NLO it is safe to ignore terms of order $\mathcal{O}(\delta Z_i^2,\, \delta Z_i \delta Z_j)$ as they only contribute at NNLO. The relevant set of counter-term Feynman rules for this work is given in Figure 2.2. The counter-term for the $t\,W\,b$-vertex is also included, despite not technically forming part of the QCD Lagrangian, as this is required to renormalize the top quark decay vertex.

The final aspect of renormalization that is required is to give meaning to the term 'physical' quantity. What this means is that a precise definition or set of (renormalization) conditions must be provided; these define the *renormalization scheme*. The three physical quantities that will be of primary interest here are the mass of heavy quarks, the strong coupling and the normalization of the gluon, light quark and heavy quark fields. The conditions on these arise by interpreting the complete propagators of the fields as descriptions of the propagation of single particle states. This requires individual full propagators to have a simple pole of residue i at the physical mass of the particle.

The widely-used modified-minimal-subtraction scheme, or $\overline{MS}$-scheme, will be employed for the strong coupling; this will not be discussed further here[7]. For the quark and gluon fields as well as the heavy quark mass, the *pole* or *on-shell* scheme will be used.

It is appropriate at this point to consider the propagator of the heavy quark,

[7]Renormalization of the electroweak coupling, g_{ew}, is not required in this work as this is not renormalized at $\mathcal{O}(\alpha_s)$, which is the target accuracy in this work.

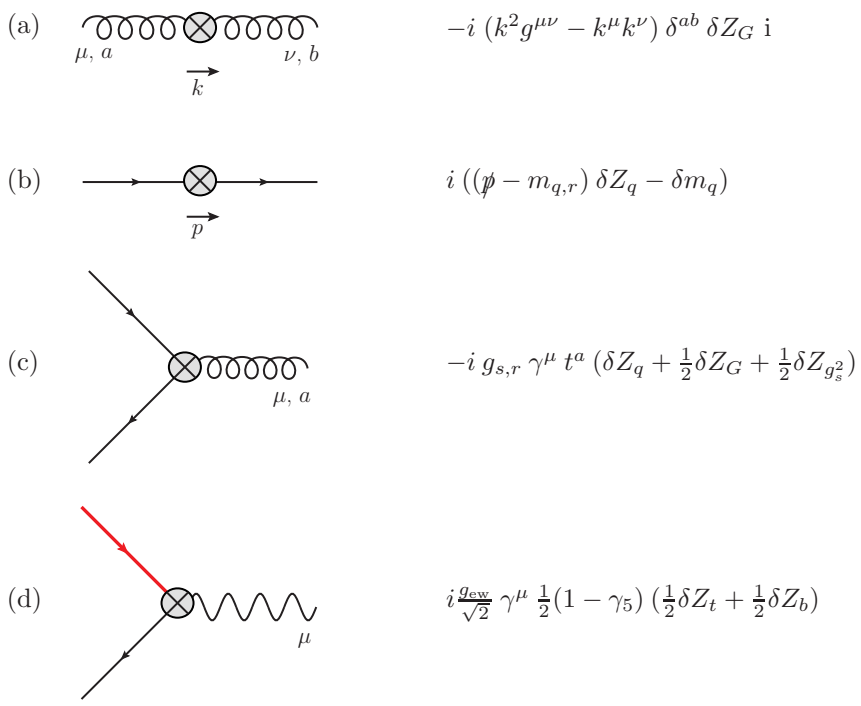

Figure 2.2: QCD and EW counter-term diagrams

Q. The complex pole, μ_Q, of the full propagator is given by the solution to $\overline{\Gamma}_Q(\mu_Q) = 0$, where

$$\overline{\Gamma}_Q(\not{p}) = \not{p} - M_Q - \overline{\Sigma}_Q(\not{p}). \tag{2.30}$$

Here M_Q and $\overline{\Sigma}_Q$ are the renormalized heavy quark mass and self-energy. It should be noted that the pole and on-shell schemes are slightly different. The on-shell scheme defines the renormalized mass, M_Q^{OS} to be the solution to $\mathrm{Re}\left[\overline{\Gamma}_Q(M_Q^{OS})\right] = 0$, whereas in the pole scheme the renormalized mass, M_Q^{pole}, is defined to be

$$M_Q^{pole} = \mathrm{Re}\left[\mu_Q\right]. \tag{2.31}$$

However, at the order to which we will work in this thesis, the pole scheme is equivalent to the on-shell scheme[8], so we choose to call the renormalized mass in

[8]The differences manifest themselves at NNLO, where the on-shell mass becomes a gauge-dependent quantity. The pole mass, being defined as the real part of a physical parameter,

any of these two schemes the pole mass.

In addition to this, the conditions for the normalization of the quark and gluon fields are that the residues of the respective complete propagators are fixed to unity, in accordance with the choice of condition for the renormalized mass.

The above mass and quark field conditions relate δm and δZ_q to the quark (unrenormalized) self-energy $\Sigma(\not{p})$ via

$$\delta M_q^{OS} = \Sigma(M_q^{OS}) \tag{2.32a}$$

$$\delta Z_q^{OS} = \frac{\partial \Sigma}{\partial \not{p}}(M_q^{OS}). \tag{2.32b}$$

The equations 2.30, 2.32a and 2.32a are solved order by order in perturbation theory to identify the relevant structure of counter-terms. For massless fermions the on-shell scheme implies that $\delta m_q = 0$ as well as $\delta Z_q = 0$, thus we need only consider mass and wavefunction renormalization for the top quark, which is always treated as massive. For the gluon field the on-shell scheme implies

$$\delta Z_G^{OS} = -\frac{\partial \Pi_T'(0)}{\partial q^2}, \tag{2.33}$$

with $\Pi_T(q^2)$ the gluon transverse self-energy.

It is well known that the pole and on-shell mass definition for quark masses suffer from non-perturbative ambiguities which do not allow for the determination of these masses with an accuracy of better than $\mathcal{O}(\Lambda_{\mathrm{QCD}})$ [28, 29]. Avoiding such ambiguities requires the use of a mass scheme that is ideally not sensitive to long-distance scale physics, such as the $\overline{MS}$-mass (such masses are known as 'short-distance' masses). However, as will be shown later on, the $\overline{MS}$-mass is poorly suited for use with the ET approaches employed in this work, which require the renormalized mass used to be close to the pole mass. A better choice of mass scheme here is, for example, the 'Potential-Subtracted' (PS) mass scheme [30][9], which is well defined at all orders in perturbation theory as well as yielding

remains gauge-independent. These arguments were first discussed in [26, 27].

[9]This was introduced along with other so-called 'threshold masses' to aid the precise extraction of a well defined top-mass parameter from a threshold scan at a linear collider.

renormalized masses close to the pole mass. The PS-mass is related to the pole mass via the equation

$$\begin{aligned} M^{PS}(\mu_{ps}) &= M^{\text{pole}} - \Delta M(\mu_{ps}) \\ &= M^{\text{pole}} + \frac{1}{2}\int_{|\vec{q}|<\mu_{ps}} \frac{d^3q}{(2\pi)^3}\tilde{V}(q), \end{aligned} \tag{2.34}$$

where $\tilde{V}(q)$ is the static heavy-quark potential in momentum space. An important aspect to highlight here is the appearance of the scale μ_{ps}, which restricts the above momentum space integral to the region containing long-distance effects. It has been shown [30] that the behaviour of the perturbative expansion of M^{pole} leading to the undesirable ambiguities matches that in the expansion of $\Delta M(\mu_{ps})$ and therefore renders $M^{PS}(\mu_{ps})$ free of these non-perturbative effects. More will be said about the choice of μ_{ps} in Chapter 5.

Finally it is important to point out that the use of dimensional regularization will, in general, result in a shift in the dimension of the parameters of the Largrangian in order to maintain that $\dim[\mathcal{L}] = d$. The couplings are shifted to $g \to \mu_R^{\epsilon} g$ where μ_R is an arbitrary mass scale, to account for the change in dimension from 4 to $4 - 2\epsilon$. Quantities in nature do not depend on this scale (it is inserted for consistency in the method used for evaluation of loop and phase space integrals), thus a prediction made to all orders should be independent of this. In contrast, calculations at fixed order in perturbation theory maintain a dependence on this artificial scale.

After renormalization, one loop amplitudes still contain IR divergences, manifested as poles in ϵ. These are cancelled exactly by the divergences in the real corrections once the latter are consistently included. This cancellation is guaranteed by the Bloch-Nordsieck [23] and Kinoshita-Lee-Nauenberg [24, 25] theorems for infra-red safe observables (this class of observables will be discussed further in §3.1.1). The singularities from real corrections will be discussed next.

2.2.2 Divergences from Real Emissions

To illustrate the origin of the divergences we shall examine the case of a gluon radiated off an external fermion line. The scenario is pictured in Figure 2.3.

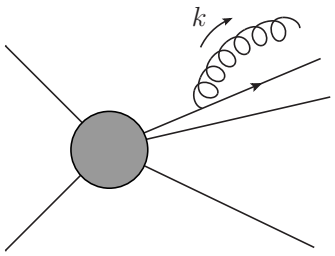

Figure 2.3: Gluon emission from a final state fermion leg.

The amplitude for this process (dropping coupling and colour factors for simplicity) is given by

$$\sim \bar{u}(p)\gamma^{\mu}\,\frac{(\not{p}+\not{k}+M_f)}{(p+k)^2-M_f^2}\,A(p,k,\ldots)\,\varepsilon_{\mu}(k)$$

$$=\bar{u}(p)\gamma^{\mu}\,\frac{(\not{p}+\not{k}+M_f)}{2p.k}\,A(p,k,\ldots)\,\varepsilon_{\mu}(k), \tag{2.35}$$

where A simply collects together the expression of the grey blob. In the soft limit, $k \to 0$, this reduces, with the help of the Dirac equation, to

$$\frac{p^{\mu}}{p.k}\,\bar{u}(p)\,A(p,0,\ldots)\,\varepsilon_{\mu}(k). \tag{2.36}$$

The important observation to make is that now there is a $1/k_0$ singularity at the amplitude level; this is known as a *soft* singularity. In the case that the fermion is massless, $M_f = 0$, then $p.k = p_0\,k_0(1-\cos\theta)$, where θ is the angle between the fermion and the gluon. In the limit $\theta \to 0$ the scalar product $p.k \to 0$ as well, and (2.35) displays an additional divergence - a *collinear* singularity.

This infra-red behaviour of amplitudes is universal, in the sense that in the soft and collinear limits, the squared amplitude or matrix element factorizes into a function describing the singular behaviour multiplied by a tree-level matrix

element. The tree-level parts of this encode all the dependence on the particular process being studied, whilst the singular function is process independent.

Following the arguments of [31] (see also [19]), we consider the Born process with two incoming partons a and b and n outgoing partons. The matrix elements (squared amplitudes) for the Born and real processes are denoted by $\mathcal{M}_n$ and $\mathcal{M}_{n+1}$, and the flavour of the partons involved by a_i. There are three basic limits one has to consider; the soft limit and the limits where the additional parton becomes collinear to either a final or initial state parton. In the emission of a soft gluon, g_k, the real matrix element behaves as

$$\mathcal{M}_{n+1}(a_a, a_b; \ldots g_k, \ldots) \to g_s^2 \sum_{i,j} \frac{s_{ij}}{s_{i\,k}\, s_{j\,k}} \mathcal{M}_n^{ij}(a_a, a_b; a_1, \ldots, a_n), \tag{2.37}$$

where $s_{ij} = 2p_i \cdot p_j$. $\mathcal{M}_n^{ij}$ denotes a colour-correlated square of Born amplitudes (for further details, see for example [32]), and the sum is over all possible pairs of external partons i and j the soft gluon can be emitted from. It is clear that this structure arises when squaring expressions of the form of (2.36). The term $s_{ij}/(s_{ik}\, s_{jk})$ is known as an Eikonal factor and is singular for $p_k \to 0$.

In the case when a final state parton, k, becomes collinear to another final state parton, j, their respective momenta can be written as $p_j = z(p_j + p_k)$ and $p_k = (1-z)(p_j + p_k)$, where $z \to 1$ is the extreme collinear limit. The behaviour then is

$$\mathcal{M}_{n+1}(\ldots, a_j, \ldots, a_k, \ldots) \to \frac{g_s^2}{p_j.p_k} \tilde{P}_{(jk)^* \to jk}(z)\, \mathcal{M}_n(\ldots, a_{(jk)}, \ldots). \tag{2.38}$$

$\tilde{P}_{(jk)^* \to jk}(z)$ is a universal splitting function which only depends on the flavours of partons j and k. The $*$ simply indicates that the splitting function is slightly off-shell to maintain momentum conservation.

Finally, in the case where a final state parton, k, becomes collinear to an initial state parton, a, the momentum of k can be written as $(1-z)p_a$. The factorization is a little more involved

$$\mathcal{M}_{n+1}(a_a, a_b; \ldots, a_k, \ldots) \to \frac{g_s^2}{p_a.p_k} \tilde{P}_{a \to (ak)^*\, k}(z)\, \mathcal{M}_n(a_{(ai)}(z\, p_a), a_b; \ldots) \tag{2.39}$$

as the momentum fraction z now appears in the Born matrix element in the factorized expression. Once more, $\tilde{P}_{a\to(ak)^*\,k}(z)$ is a process independent splitting function completely determined by the flavours of partons a and k[10].

In all limits discussed above the singular terms result in poles in ϵ when integrated over phase space. IR-singularities from the virtual corrections are cancelled by these.

[10]The tildes on $\tilde{P}_{(jk)^*\to jk}$ and $\tilde{P}_{a\to(ak)^*\,k}$ indicate that these are not the full splitting functions, but splitting functions valid only for $z < 1$. They are related to the full splitting functions via + distributions and delta functions. For details we refer to [19].

Chapter 3

Collider Predictions at NLO

3.1 Cross-sections at Hadron Colliders

Computations of hadronic cross-sections are made possible because of the Factorization Theorem [33, 34], which states that these can be written as a convolution of partonic cross-sections with non-perturbative functions describing the extraction of partons from hadrons. This is illustrated in Figure 3.1. More precisely, cross-sections for two hadrons, $h_1(P_1)$, $h_2(P_2)$ interacting to produce a final state, X, can be written as

$$\sigma_{h_1,\,h_2\to X(Q^2)} = \sum_{a,b} \int_0^1 dx \int_0^1 dy\; f_{a/h_1}(x;\mu_F^2) f_{b/h_2}(y;\mu_F^2) \sigma_{ab\to X}(p_a, p_b; \mu_F^2, \mu_R^2), \tag{3.1}$$

with $p_a = xP_1$ and $p_b = yP_2$.

The term $\sigma_{a,\,b\to X}$ is the partonic cross-section for the process $a\,b \to X$, also called the 'hard-interaction' cross-section. The sum is performed over all possible initial partonic states a and b that can give the final state X. This part describes the short-distance physics and can be computed in perturbation theory. The connection to the long-distance physics of the initial state hadrons is given through the functions $f_{i/h_k}(x;\mu_F^2)$. These are the *Parton Distribution Functions* (PDFs) which describe the probability of finding a parton i inside the hadron h_k, with a given momentum fraction, x, of the hadron's momentum. Though

non-perturbative, they are universal functions that can be extracted from experiments (e.g. Deep Inelastic Scattering) and used in cross-section calculations. μ_F is the *factorization scale*; an artificial scale inserted to separate short- and long-distance physics. The cross-section in nature must once again be independent

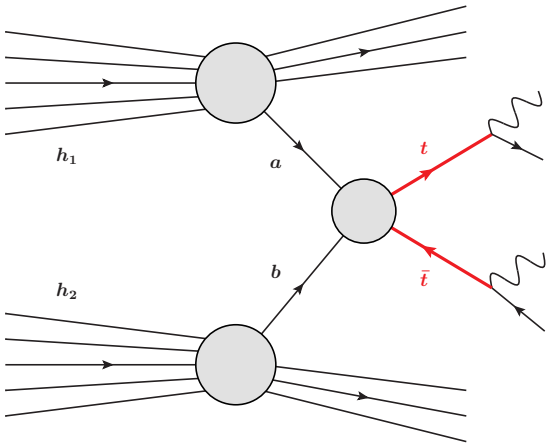

Figure 3.1: Visualisation of the Factorization Theorem

of this scale. However, as one works to finite order in perturbation theory, the resulting approximation of the physical cross-section carries a dependence on μ_F (and μ_R). A variation of the unphysical parameters μ_F and μ_R, present in a fixed order calculation, is often performed to obtain a rough handle on the size of uncalculated higher order corrections.

Many groups are actively involved in the extraction of these PDFs from experimental data (see for example [35, 36, 37]). The PDF set chosen for the results presented in this work is the MSTW2008 PDF set [36].

The quantities in 3.1 can be expanded in perturbation theory and in particular the hard interaction part takes the form

$$\sigma_{ab\to X} = \sigma_{ab}^{LO} + \sigma_{ab}^{NLO} + \dots \tag{3.2}$$

where σ^{LO} is the Born-level partonic cross-section and σ_{ab}^{NLO} is the NLO correction. When the final state X contains m partons, we have (using notation similar

to that in [32])

$$\sigma_{ab}^{LO} = \int_m d\sigma_{ab}^B(p_a, p_b) \tag{3.3}$$

$$\sigma_{ab}^{NLO} = \int_m d\sigma_{ab}^V(p_a, p_b) + \int_{m+1} d\sigma_{ab}^R(p_a, p_b) + \int_m d\sigma_{ab}^C(p_a, p_b; \mu_F^2). \tag{3.4}$$

The terms $d\sigma_{ab}^V$ and $d\sigma_{ab}^R$ involve the virtual (one-loop) and real (single gluon emission) corrections to the Born-level process. $d\sigma_{ab}^C$ is the collinear counter-term and arises from NLO corrections to the PDFs. Like the virtual and real corrections, these are divergent and are collected in the collinear counter-term. Although the terms above are individually divergent, their sum is finite and well defined. Precisely how these are combined to give sensible results will be looked at in detail in §3.2.

3.1.1 Measurement Functions and Infra-Red Safety

The coloured partons discussed in the context of perturbation theory are never observed as final states due to QCD confinement. Quarks and gluons instead manifest themselves in experimental final states as sprays of hadrons known as jets. Correctly linking partonic calculations with physical observables (including the cross-section) requires the introduction of a Measurement (or Jet) Function, $\mathcal{F}$, which defines measured quantities in terms of partonic momenta. In general this will be composed of multiple theta functions, imposing conditions and cuts on the final state X. With this introduction, the terms in 3.4 appear as

$$\int_m d\sigma_{ab}^{B,V} = \frac{1}{2s_{ab}} \frac{1}{\bar{n}_a \bar{n}_b} \int d\Phi_m \, \mathcal{M}_{ab}^{B,V,C}(p_a, p_b, \{p_i\}) \, \mathcal{F}^m(p_a, p_b, \{p_i\}) \tag{3.5}$$

$$\int_m d\sigma_{ab}^{C} = \frac{1}{2s_{ab}} \frac{1}{\bar{n}_a \bar{n}_b} \int_0^1 dx \int d\Phi_m(x) \, \mathcal{M}_{ab}^{C}(xp_a, p_b, \{p_i\}) \, \mathcal{F}^m(xp_a, p_b, \{p_i\}) \tag{3.6}$$

$$\int_{m+1} d\sigma_{ab}^{R} = \frac{1}{2s_{ab}} \frac{1}{\bar{n}_a \bar{n}_b} \int d\Phi_{m+1} \, \mathcal{M}_{ab}^{R}(p_a, p_b, \{p_i\}) \, \mathcal{F}^{m+1}(p_a, p_b, \{p_i\}). \tag{3.7}$$

in a cross-section calculation. $\mathcal{M}_{ab}^{B,V,C,R}$ are the Born, virtual, collinear counter-term and real matrix elements for the process[1]. $\mathcal{F}^m$ behaves as

$$\mathcal{F}^m(p_a, \ldots, p_m) \to 0, \quad \text{for } p_i.p_j \to 0, \tag{3.8}$$

thus properly defining the Born process of interest, ensuring the constituents of X are physically distinguishable and each with a measurable momentum.

$\mathcal{F}$ does not only serve to define our process, but also plays a crucial role when higher order corrections are included. As previously mentioned, the cancellation of singularities between virtual and real corrections at higher orders in perturbation theory is guaranteed by the KLN theorem for appropriately defined quantities. The property that observables must have to guarantee this vital cancellation is infra-red safety. This restriction essentially means that observables must remain unchanged upon radiation of soft and (or) collinear massless partons. If not, observables are liable to receive large (infinite) corrections from every order in perturbation theory.

The tool that ensures we calculate infra-red safe observables is $\mathcal{F}$. The properties this must posses in the soft and collinear limits are (see for example [31, 32])

$$\mathcal{F}^{m+1}(p_1, \ldots, p_m, p_{m+1} = \lambda q) \to \mathcal{F}^m(p_1, \ldots, p_m), \quad \text{for } \lambda \to 0 \tag{3.9}$$

$$\mathcal{F}^{m+1}(p_1, \ldots, p_i, \ldots, p_{m+1}) \to \mathcal{F}^m(p_1, \ldots, (p_i + p_{m+1}), \ldots, p_m),$$
$$\text{for } p_i \to z(p_i + p_{m+1}),\ p_{m+1} \to (1-z)(p_i + p_{m+1}). \tag{3.10}$$

3.2 Infra-Red Singularities and the Subtraction Method

The key starting point in the computation of a NLO cross-section is (3.4). We recall that V and R stand for the virtual and real corrections, whilst C labels the collinear counter-term required for NLO cross-sections involving initial state

[1]Outside the integral signs, the terms $1/s_{ab}$ and $1/(\bar{n}_a \bar{n}_b)$ correspond to the flux factor and the spin-colour averaging factors respectively.

partons. The terms $\int_m d\sigma^V$, $\int_{m+1} d\sigma^R$ and $\int_m d\sigma^C$ are individually IR divergent. However, as discussed earlier, for IR-safe observables, the singularities cancel in the sum of these terms.

For the real contribution, it is required that the integral over the additional parton phase-space, $\int_1 d\sigma^R$, be performed in d-dimensions and the divergences present extracted as poles in ϵ. These can then be cancelled by the ϵ poles from the virtual contributions to yield finite (in ϵ) expressions. The limit $\epsilon \to 0$ can then be safely taken and the integral over the m-parton phase-space can be performed. However, the integral over the additional parton phase-space is often impossible to compute analytically and one is forced to resort to a numerical approach to extract meaningful quantities from 3.4. Despite this not being completely straightforward, as one has to deal with divergent quantities which sum up to give finite results, it is well known how to progress.

There are two conceptually different approaches to this problem, the *Subtraction* method and the *Slicing* method [38]. In this work we will focus on the former. The trick, known as the Subtraction method, is to add zero to 3.4; more precisely, a term (known as a *subtraction counter-term*)

$$\int_{m+1} d\sigma^{R,c.t.} \tag{3.11}$$

is added and subtracted. Should this term satisfy certain properties, namely, reproduce all the singular regions of $d\sigma^R$ exactly and if the integral $\left(\int_1 d\sigma^{R,c.t.}\right)_{d=4-2\epsilon}$ can be performed analytically, then 3.4 can be written as

$$\sigma_{ab}^{\mathrm{NLO}}(p_a,p_b;\mu_F^2) =$$

$$\int_m \left(d\sigma_{ab}^V(p_a,p_b) + d\sigma_{ab}^C(p_a,p_b;\mu_F^2) + \int_1 d\sigma^{R,c.t.}(p_a,p_b) \right)_{\epsilon=0} \tag{3.12a}$$

$$+ \int_{m+1} \left(d\sigma_{ab}^R(p_a,p_b) - d\sigma^{R,c.t.}(p_a,p_b) \right)_{\epsilon=0}. \tag{3.12b}$$

Since the counter-term mimics the real matrix element in all its divergent regions, the ϵ-poles of $\int_1 d\sigma^{R,c.t.}$ are identical to those of $\int_1 d\sigma^R$. This means that (3.12a)

is free of ϵ-poles and finite, so the integrals over the m-parton phase-space can be performed numerically in 4 dimensions. Similarly, (3.12b) is also finite and the integral over the $m+1$-parton phase-space can be done numerically.

The success of this method clearly hinges on the construction of the local counter-term $d\sigma^{R,c.t.}$ with desirable properties outlined above. Fortunately, this is made possible by the universal IR behaviour of QCD scattering amplitudes. The two mainstream approaches to constructing these local counter-terms are the *Dipole method* of Catani and Seymour [32] (along with its generalization to massive final state partons [39]) and the *FKS method* of Frixione, Kunszt and Signer [40] (and its generalization to the massive case [41]). These two methods will now be briefly described.

3.2.1 The Dipole Subtraction Method

As mentioned above, it is the universal IR behaviour of QCD amplitudes that is exploited to construct the local subtraction counter-terms. In the Dipole Method, a term is constructed that simultaneously captures the limits in which two partons become soft or collinear to each other. Restricting ourselves to the case where a final state k becomes soft or collinear to another final state, i, the method works as follows. Firstly, the various partons involved are defined as the *emittor* parton, (ik) (the one that splits), the *emitted* parton, k, and a *spectator* parton, labelled j here. The latter is the parton colour connected to the emittor in the soft limit. *Dipole* functions can then be written down which smoothly interpolate between the strict soft and collinear limits and regions away from these. For the case considered here, the dipole takes the form

$$\mathcal{D}_{ik,j} = \mathcal{M}^{ij}(\{\tilde{p}_l\})\,\mathbf{V}_{ik,j}, \tag{3.13}$$

where the factorization into a Born-level (colour-correlated) matrix element and a function describing the singular limits is evident. The dipoles are universal in the sense that the process dependence only enters in the Born-level matrix element, $\mathcal{M}^{ij}$, whilst the expressions $\mathbf{V}_{ik,j}$ are process independent (the only dependence they have are on the flavour of the partons i, j and k). The Born-level matrix element is evaluated with new momenta $\{\tilde{p}_l\}$, obtained from the original momenta

via a mapping

$$\{p_a,\, p_b;\, p_1, \ldots, p_n,\, p_{n+1}\} \rightarrow \{\tilde{p}_a,\, \tilde{p}_b;\, \tilde{p}_1, \ldots,\, \tilde{p}_n\}. \tag{3.14}$$

This mapping must be performed as the Born-level matrix element requires a reduced, n-final-state configuration.

In general, the emittor and the spectator can be either final state or initial state partons, yielding four different types of dipole function. The full expressions for these functions can be found in the original Dipole Formalism papers [32, 39]. The full counter-term for the real matrix element can then be written schematically as

$$\begin{aligned} d\sigma^{R,c.t.} &= \sum_{D} \mathcal{D}(\{p_i\}) \cdot \mathcal{F}(\{\tilde{p}_i\}) \\ &= \sum_{\text{dipoles}} d\sigma^B \otimes \left(dV_{\text{dipoles}} + dV'_{\text{dipoles}} \right). \end{aligned} \tag{3.15}$$

The term dV_{dipoles} matches the divergences of the real matrix element arising from regions where the additional parton becomes soft and/or collinear to a final state parton, whilst dV'_{dipoles} reproduces the singularities present when the additional parton becomes collinear to an initial state parton. Integration over the additional parton phase-space can be performed analytically to give

$$\int_1 d\sigma^B \otimes dV_{\text{dipoles}} = d\sigma^B \otimes \mathbf{I}(\epsilon) \tag{3.16}$$

and

$$\begin{aligned} \int_1 d\sigma^B \otimes dV'_{\text{dipoles}} = &\int_0^1 dx\, d\sigma^B(xp_a, p_b) \otimes \left(\mathbf{P}(xp_a, x, \mu_F^2) + \mathbf{K}(x) \right) \\ &+ \int_0^1 dy\, d\sigma^B(p_a, yp_b) \otimes \left(\mathbf{P}(yp_b, y, \mu_F^2) + \mathbf{K}(y) \right). \end{aligned} \tag{3.17}$$

$\mathbf{I}$, $\mathbf{K}$ and $\mathbf{P}$ are universal, so-called, *insertion* factors. $d\sigma^B \otimes \mathbf{I}(\epsilon)$ contains ϵ-poles which cancel those from the virtual matrix element; the pole structure of the $\mathbf{I}$

insertions will be indicated explicitly where appropriate.

Putting everything together, the NLO correction to the cross-section can be written as the sum of three separate finite terms,

$$\sigma^{\mathrm{NLO}}(p_a,p_b;\mu_F^2) = d\sigma^{\mathrm{NLO},\{m+1\}}(p_a,p_b) + d\sigma^{\mathrm{NLO},\{m\}}(p_a,p_b) + \int_0^1 dx \ \left[d\hat{\sigma}^{\mathrm{NLO},\{m\}}(xp_a,p_b;\mu_F^2) + d\hat{\sigma}^{\mathrm{NLO},\{m\}}(p_a,xp_b;\mu_F^2)\right] \tag{3.18}$$

with each term individually given by

$$d\sigma^{\mathrm{NLO},\{m+1\}}(p_a,p_b) = \int_{m+1} \left[d\sigma^R_{ab}(p_a,p_b) - \sum_{\mathrm{dipoles}} d\sigma^B \otimes \left(dV_{\mathrm{dipoles}} + dV'_{\mathrm{dipoles}}\right)\right], \tag{3.19}$$

$$d\sigma^{\mathrm{NLO},\{m\}}(p_a,p_b) = \int_m \left[d\sigma^V_{ab}(p_a,p_b) + d\sigma^B \otimes \mathbf{I}(\epsilon),\right] \tag{3.20}$$

$$\int_0^1 dx \ \left[d\hat{\sigma}^{\mathrm{NLO},\{m\}}(xp_a,p_b;\mu_F^2) + d\hat{\sigma}^{\mathrm{NLO},\{m\}}(p_a,xp_b;\mu_F^2)\right] = \int_m \left[d\sigma^C_{ab}(p_a,p_b;\mu_F^2) + \int_0^1 dx\, d\sigma^B(xp_a,p_b) \otimes (\mathbf{K}(x) + \mathbf{P}(x,\mu_F^2)) + \int_0^1 dx\, d\sigma^B(p_a,xp_b) \otimes (\mathbf{K}(x) + \mathbf{P}(x,\mu_F^2))\right]. \tag{3.21}$$

These are now in a form that can be readily integrated with a Monte Carlo integrator where arbitrary IR-safe cuts on the final state phase-space may be imposed.

3.2.2 The FKS Subtraction Method

In the FKS method the universal IR behaviour of QCD amplitudes is exploited in a rather different way to construct a local subtraction counter-term. To illustrate the key idea we first consider a function $f(\xi, y)$ which in the limits $\xi \to 0$ and

$y \to 1$ diverges as $1/\xi$ and $1/(1-y)$ respectively and thus the integral

$$I = \int_0^{\xi_{\max}} d\xi \int_{-1}^{1} dy \; f(\xi, y) \tag{3.22}$$

is singular. Due to the divergences appearing at the specified points in phase-space, it is possible to isolate and remove them through the use of +-distributions. Modifying the above integral to

$$I_{\text{subtr.}} = \int_0^{\xi_{\max}} d\xi \int_{-1}^{1} dy \; \left(\frac{1}{\xi}\right)_{\xi_{\text{cut}}} \left(\frac{1}{1-y}\right)_{\delta} \xi \, (1-y) \, f(\xi, y) \tag{3.23}$$

where the +-distributions are defined by

$$\int_0^{\xi_{\max}} d\xi \; \left(\frac{1}{\xi}\right)_{\xi_{\text{cut}}} g(\xi) = \int_0^{\xi_{\max}} d\xi \; \frac{g(\xi) - g(0)\Theta(\xi_{\text{cut}} - \xi)}{\xi}, \tag{3.24}$$

$$\int_{-1}^{1} dy \; \left(\frac{1}{1-y}\right)_{\delta} g(y) = \int_{-1}^{1} dy \; \frac{g(y) - g(1)\Theta(y - 1 + \delta)}{1-y}. \tag{3.25}$$

The Θ-functions are the Heaviside-step functions and the parameters $0 < \xi_{\text{cut}} < \xi_{\max}$ and $0 < \delta < 2$ are arbitrary parameters dictating how close to the divergent phase-space points ξ and y can get. The modified integral takes the form

$$\begin{aligned} I_{\text{subtr.}} = \int_0^{\xi_{\max}} d\xi \int_{-1}^{1} dy \; \{ & f(\xi, y) - f(0, y)\Theta(\xi_{\text{cut}} - \xi) - f(\xi, 1)\Theta(y - 1 + \delta) \\ & + f(0, 1)\Theta(\xi_{\text{cut}} - \xi)\Theta(y - 1 + \delta)\} \end{aligned} \tag{3.26}$$

and is finite under integration over $d\xi$ and dy. The prescription described by the above equations is precisely the one that allows for a realisation of the Subtraction

Method. To see this we now make the replacements

$$\xi \to \xi_k, \tag{3.27}$$

$$y \to y_{ik}, \tag{3.28}$$

$$f(\xi, y)\, d\xi\, dy \to \mathcal{M}^R(\xi_k, y_{ik})\, \xi_k\, d\xi_k\, dy_{ik}, \tag{3.29}$$

where ξ_k and y_{ik} parametrize the energy of the additional parton, k and the cosine of its angle relative to the parton i. $\mathcal{M}^R$ is the real matrix element, which depends on ξ_k and y_{ik} as well as other phase space variables. The limits $\xi_k \to 0$ and $y_{ik} \to 1$ are the soft and collinear limits, where by collinear we mean collinear to parton i. The additional factor of ξ_k in the replacements above comes from the measure of the emitted parton's phase space. It is clear that the situation for $\xi_k\, \mathcal{M}^R(\xi_k, y_{ik})$ is just as for the function $f(\xi, y)$ since as discussed the real matrix element diverges as $1/\xi_k^2$ and $1/(1 - y_{ik})$ in the soft and collinear limits.

As it stands, the above prescription is valid if there is only one coloured external parton at Born-level. In order to make full use of this machinery in practice a partitioning of the phase space must be performed, where in each partition the emitted parton can become collinear to at most one other external parton. This means that each partition contains no more than one soft and one collinear singularity and the method described above using the +-distributions can be applied. The splitting up of phase-space is achieved via the introduction of functions $\mathcal{S}_i$ constructed such that

$$\mathcal{M}^R = \sum_i \mathcal{S}_i\, \mathcal{M}^R \tag{3.30}$$

and $\mathcal{S}_i \to 0$ when k becomes collinear to a parton other than i.

The method so far provides the local subtraction counter-terms required for (3.12*b*). To be consistent, the terms subtracted must be added back. The terms added back will involve simpler integrals that can be straightforwardly evaluated analytically in d-dimensions, providing the ϵ-poles required to cancel those present in the virtual matrix element.

A feature of the method outlined here is that the dependence of the counter-

terms on the parameters $\xi_{\rm cut}$ and δ translates to a dependence on these parameters of (3.12a) and (3.12b) separately. However the physical quantity obtained when adding these two contributions is, as expected, independent of the choice of these parameters.

For many more details on the functions $\mathcal{S}_i$, the parametrization of phase-space and all analytical formulas required, we refer to the original FKS paper [40] as well as a more recent paper [41] describing the extension of the method to the case of massive partons and its automation in NLO calculations in general.

Chapter 4

The Unstable Top Quark

Unstable particles such as Z and W bosons or the top quark are not seen in detectors. Instead, their existence is inferred by an examination of their decay products. In this chapter we describe some of the main approaches to unstable particle production and decay and discuss the role of hard and soft gluons in higher order corrections to such processes.

4.1 Resummation of the Top Quark Propagator

Let us consider a process in which the final state $\{l_1, \ldots, l_M,\ f_1, \ldots,\ f_N\}$ is produced and where a heavy unstable particle, X, may contribute to this final state via $X \to f_1, \ldots,\ f_N$.

In general, the tree-level amplitude for this process may be written as

$$\mathcal{A}^{(0)} = \frac{\mathcal{K}(p_i)}{p_X^2 - M_X^2} + \mathcal{N}(p_i) \tag{4.1}$$

where p_i are the final state momenta, $p_X^2 = (p_{f_1} + \ldots p_{f_N})^2$ and M_X is mass of particle X. $\mathcal{K}$ includes the Feynman diagrams involving the decay subprocess $X \to f_1, \ldots,\ f_N$, the *resonant* diagrams, whilst $\mathcal{N}$ accounts for the *non-resonant* diagrams which do not involve a decay of X.

The kinematic limit $p_X^2 \to M_X^2$ sees this amplitude run into a non-integrable singularity. This is an indication that higher order terms in the pertubative ex-

pansion become of the same magnitude as the leading term and must be included to all orders. The known cure for this is a Dyson resummation of self-energy insertions, $\overline{\Sigma}_X$, to the X-propagator. In the case where X is a top quark, this amounts to performing the substitution

$$\frac{i(\not{p}_t + M_t)}{p_t^2 - M_t^2} \to \frac{i(\not{p}_t + M_t)}{p_t^2 - M_t^2} \sum_{n=0}^{\infty} \left[-i\overline{\Sigma}_t(\not{p}) \frac{i(\not{p}_t + M_t)}{p_t^2 - M_t^2} \right]^n \tag{4.2}$$

for the resonant top quark propagators in (4.1). The Dyson resummation shifts the pole of the heavy particle propagator away from the real axis as follows,

$$p_X^2 - M_X^2 \to p_X^2 - M_X^2 - i\overline{\Sigma}_X(p_X^2), \tag{4.3}$$

thus regulating the pole for real momenta.

Whilst in principle this is fine when just studying the propagator, making this replacement in the amplitude (4.1), is potentially dangerous. The self-energy will in general only be known up to some fixed order, and is a gauge-dependent quantity. Thus the naive replacement (4.3) will usually yield gauge-dependent amplitudes; a problem only cancelled by some (uncalculated) higher orders. Mixing up orders in perturbation theory, if not done with care, will lead to violation of gauge invariance - a property only guaranteed for fixed order amplitudes in perturbation theory. Various approaches to treating unstable particles whilst maintaining gauge-invariant amplitudes will now be outlined.

4.2 On-Shell Treatment

An assumption that can be made that simplifies the calculation of the amplitude of (4.1) is to make the kinematic constraint that $p_X^2 = (p_{f_1} + \dots p_{f_N})^2 = M_X^2$. We will see how this is an approximation that can be introduced in a systematic manner.

The resonant part of the tree-level amplitude, $\mathcal{K}(\{p_i\}, p_X^2)$, can always be written as

$$\mathcal{K}(\{p_i\}, p_X^2) = P^{\alpha}(i\, j \to l_1,\, \dots,\, l_M,\, X)\Pi_{\alpha\beta}(p_X)D^{\beta}(X \to f_1, \dots, f_N), \tag{4.4}$$

namely, factorized into production and decay parts, P and D linked together by the numerator of the unstable particle propagator, $\Pi(p_X)$. The spin indices of X are made explicit to emphasise that no approximations have yet been made and that all correlations are still included in the expression on the RHS of (4.4).

Squaring this resonant amplitude (assuming that a resummation of the propagator has been performed[1]) and integrating over the final state phase-space, we have

$$\int d\Phi_{ij\to l_1,\ldots,l_M,f_1,\ldots,f_N} \frac{\mathcal{K}(\{p_i\},p_X^2)\,\mathcal{K}^*(\{p_i\},p_X^2)}{(p_X^2-M_X^2)^2+M_X^2\Gamma_X^2}$$

$$=\int \frac{dp_X^2}{2\pi}\int d\Phi_{ij\to l_1,\ldots,l_M,X}\, d\Phi_{X\to f_1,\ldots,f_N}\frac{\mathcal{K}(\{p_i\},p_X^2)\,\mathcal{K}^*(\{p_i\},p_X^2)}{(p_X^2-M_X^2)^2+M_X^2\Gamma_X^2}. \tag{4.5}$$

Now we can utilise the following expansion of the denominator above

$$\frac{1}{(p_X^2-M_X^2)^2+M_X^2\Gamma_X^2}=\frac{\pi}{M_X\Gamma_X}\delta(p_X^2-M_X^2)+\mathcal{O}(\frac{\Gamma_X}{M_X}) \tag{4.6}$$

to simplify this expression. If we keep only the first term in the expansion it is straightforward to see that this yields the expression

$$\frac{1}{2M_X\Gamma_X}\int d\Phi_{ij\to l_1,\ldots,l_M,\bar{X}}\, d\Phi_{\bar{X}\to f_1,\ldots,f_N}\mathcal{K}(\{p_i\},M_X^2)\,\mathcal{K}^*(\{p_i\},M_X^2), \tag{4.7}$$

where the bar on $\bar{X}$ simply indicated that now the unstable particle X is treated as on-shell everywhere. Some simplifications follow from this.

Firstly, the condition $p_X^2=M_X^2$ means that $\Pi(p_X)$ can be written as a sum

[1]Strictly speaking the form of the propagator with a fixed width, Γ_X, is only valid when in the region of $p_X^2\sim M_X^2$ we have that $\mathrm{Im}[\,\overline{\Sigma}(p_X^2)]\ll M_X^2$ and the approximation $\mathrm{Im}[\,\overline{\Sigma}(p_X^2)]\simeq \mathrm{Im}[\,\overline{\Sigma}(M_X^2)]$ can be applied, yielding the standard Breit-Wigner propagator.

over a complete set of states

$$\Pi(p_X) = \not{p}_X + M_X = \sum_{\text{spins}} u(p_X)\bar{u}(p_X), \qquad \text{if X is a fermion,} \tag{4.8}$$

$$\Pi(p_X) = -g^{\mu\nu} + \frac{p_X^\mu p_X^\nu}{M_X^2} = \sum_{\text{pols}} \varepsilon^\mu(p_X)\varepsilon^{\nu\,*}(p_X), \qquad \text{if X is a vector boson .} \tag{4.9}$$

The full expression for the tree-level resonant piece reduces to

$$\mathcal{K}(\{p_i\}, M_X^2) = \sum_s \mathcal{A}^{(0)}_{\text{prod}}(i\,j \to l_1,\,\ldots,\,l_M,\,\bar{X}^s)\mathcal{A}^{(0)}_{\text{dec}}(\bar{X}^{-s} \to f_1, \ldots, f_N). \tag{4.10}$$

$\mathcal{A}^{(0)}_{\text{prod}}$ and $\mathcal{A}^{(0)}_{\text{dec}}$ are now the actual amplitudes for the production and decay processes $i\,j \to l_1,\,\ldots,\,l_M,\,\bar{X}$ and $\bar{X} \to f_1, \ldots, f_N$. The amplitudes are still linked by the sum over spins, thus correlations between production and decay subprocesses are still present (as in the case where no approximations are made (4.4)). However, any off-shell effects have been eradicated, hiding somewhere in the higher orders in the expansion in Γ_X/M_X; all effects of off-shell propagators have amounted to a constant phase factor.

What has been thus far described is known as the improved Narrow Width Approximation (iNWA). A further simplification can be achieved if one wishes to ignore spin correlations between production and decay subprocesses. In this case the resonant amplitude squared, integrated over phase space, reduces to

$$\frac{1}{2\,M_X\Gamma_X} \int d\Phi_{i\,j\to l_1,\,\ldots,\,l_M,\,\bar{X}} \left|\mathcal{A}^{(0)}_{\text{prod}}\right|^2 \int d\Phi_{\bar{X}\to f_1,\ldots,f_N} \left|\mathcal{A}^{(0)}_{\text{dec}}\right|^2, \tag{4.11}$$

known as the Narrow Width Approximation (NWA). It can be significantly simpler technically to calculate the required matrix elements for the NWA compared to calculating those required for the iNWA. In the case of the former, production and decay matrix elements can be treated completely independently, whilst in the latter case they must be spin correlated.

Going to higher orders in the perturbative expansion in the iNWA or NWA is fairly straightforward. At NLO the computation of one-loop and real-emission

corrections to $\mathcal{A}^{(0)}_{\text{prod}}$ or $\mathcal{A}^{(0)}_{\text{dec}}$ is required. Writing the differential cross-sections of the production and decay subprocesses as $d\sigma_P$ and $d\sigma_D$, at LO and NLO respectively the total differential cross-section is given by

$$\text{LO: } d\sigma^0 = d\sigma^0_P \otimes d\sigma^0_D \tag{4.12}$$

$$\text{NLO: } d\sigma^1 = \alpha\, d\sigma^1_P \otimes d\sigma^0_D + \alpha\, d\sigma^0_P \otimes d\sigma^1_D. \tag{4.13}$$

In principle, to be fully consistent in perturbation theory one should also expand the decay width, Γ_X, in the coupling α. The construction of an NLO correction to the differential cross-section that is *strictly* of $\mathcal{O}(\alpha)$ accuracy is then possible. The (i)NWA thus provides one with a consistent framework with which to make predictions correct to whatever fixed order in perturbation theory required (or possible). There is no danger of the width spoiling gauge cancellations between diagrams due to the fact that Dyson resummation of self-energies has been demoted to a constant phase-space factor.

The corrections to the production and decay processes are known as *factorizable* corrections. Due to the way the phase space has factorized, as a result of the on-shell condition, corrections connecting production and decay subprocesses (*non-factorizable corrections*) are forbidden by momentum conservation. Schematic diagrams indicating the corrections required in the on-shell case are shown in Figure 4.1.

We note that when the on-shell assumption is made no effects coming from non-resonant diagrams are included. The final matrix elements are strictly gauge-invariant thanks to the intermediate unstable particle being on-shell and the amplitudes themselves therefore correspond to physical amplitudes. In fact, this also means that the production and decay amplitudes are also independently gauge-invariant.

4.2.1 Decays of W-bosons

Throughout this work W-bosons are implicitly assumed to decay to leptons. These decays are included in the iNWA which amounts to replacing the W-

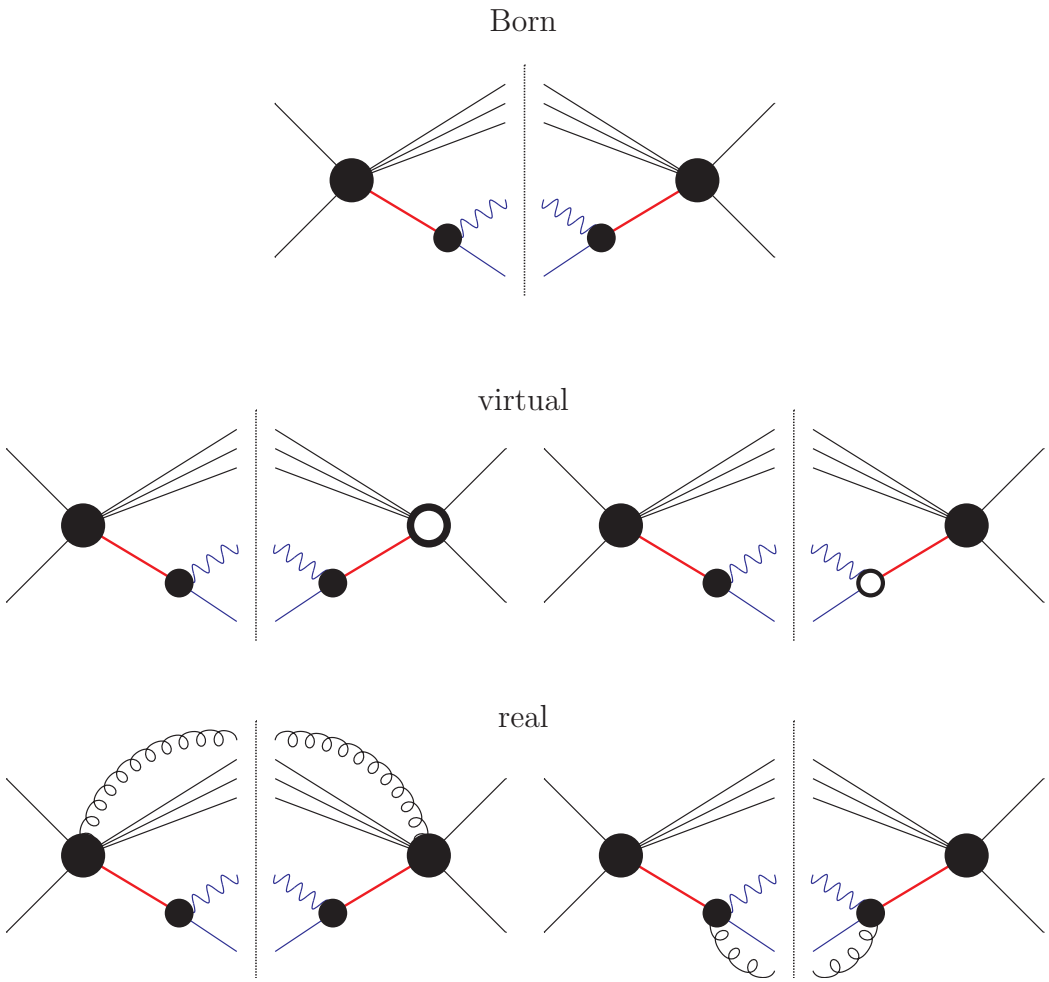

Figure 4.1: Schematic diagrams of corrections required in the production and subsequent decay of an unstable heavy particle, X, in the (i)NWA. No loops connecting production and decay are present and interferences between real emissions from production and decay are not permitted.

polarization tensors in the amplitudes with the expressions:

$$\varepsilon^{\mu}(p_{W^+} = p_{l^+} + p_{\nu_l}) \to \frac{i\, g_{\text{ew}}}{\sqrt{2}} \frac{1}{\sqrt{2M_W\Gamma_W}} \langle p_{\nu_l}| \gamma^{\mu} |p_{l^+}] \tag{4.14}$$

$$\varepsilon^{\mu}(p_{W^-} = p_{l^-} + p_{\bar{\nu}_l}) \to \frac{i\, g_{\text{ew}}}{\sqrt{2}} \frac{1}{\sqrt{2M_W\Gamma_W}} \langle p_{l^-}| \gamma^{\mu} |p_{\bar{\nu}_l}] \,. \tag{4.15}$$

At tree-level, hadronic decays, for example $W^+ \to u\,\bar{d}$, can be incorporated in much the same manner. These however, have not been included in the work presented in this thesis.

4.2.2 On-Shell Top-Pair Literature

Next-to-leading order corrections to top-pair production processes where top quarks are taken to be on-shell have been the object of studies spanning more than two decades. Corrections to stable top-pair production have been presented in [42, 43, 44, 45, 46]. As these calculations were made prior to the discovery of the top quark, the studies were focused mainly on b-quark production and light ($M_t < 170\,\text{GeV}$) top quark production at relatively low center of mass energies. Corrections of up to 50% were observed both for total cross-sections and in various distributions thus indicating the importance of NLO corrections in the description of the production of heavy quarks. However, this pioneering work does not allow for the construction of Monte Carlo's where the final states generated are the decay products of the top quarks. To achieve this the decay of the tops must be included.

QCD corrections to production and decay of a $t\bar{t}$-pair, including spin correlations, have been presented in [47, 48]. This description of top-pair production has also been implemented recently in the public Monte Carlo generator, MCFM [49]. This work allows for a realistic description of top-pair production at hadron colliders due to the final states being the b-quark jets and leptons arising from the decay of the tops. Including NLO corrections in the decay has significant effects in some distributions; this will be illustrated further on. Moreover, for observables sensitive to the spin of the heavy tops (e.g. the opening angle between the two leptons), including spin correlations between production and decay subprocesses has important effects, therefore for a good description of such observables the iNWA should be employed over the NWA.

For a large class of observables, the (i)NWA is sufficient for a good description of the partonic processes. In particular, the argument that corrections to the (i)NWA are suppressed by a factor of $\sim \Gamma_t/M_t$ enforces this idea. However, as will be explained in the next section, this argument only holds for observables

that are inclusive in the invariant mass of the top and this strong suppression is not expected to hold otherwise.

4.3 Off-Shell Treatment

Relaxing the assumption that X is on-shell results in complications. Not only must care be taken to ensure gauge invariance upon inserting the Dyson resummed propagator, but, in addition, the calculation becomes more involved as will now be discussed.

Firstly, contributions from background diagrams (the term $\mathcal{N}$ in (4.1)) can no longer be ignored. As the split into resonant/non-resonant diagrams is not a gauge-invariant one, these background diagrams must be included to guarantee gauge invariance. Going to higher orders, this means one-loop and real-emission corrections must be calculated for *all* background as well as resonant diagrams. Simply due to the proliferation of diagrams that must be computed, this leads to a significant increase in complexity of the calculation. Schematic diagrams required in the fully off-shell scenario are depicted in Figure 4.2.

A further difficulty comes via the shift $M_t^2 \to \mu_t^2$ in the unstable particle propagators due to Dyson resummation. All loop diagrams involving the unstable particle in the loop require the evaluation of integrals with complex masses. This presents additional challenges.

4.3.1 Non-Factorizable Corrections

A class of corrections that must be consistently included once the unstable particle is considered to be off-shell are the non-factorizable corrections. These corrections connecting production and decay subprocesses have traditionally been thought of as technically difficult to compute as, in particular, they involve the computation of multi-point and multi-scale integrals. Studies of the effects of non-factorizable corrections have shown that for inclusive observables, such as the total production cross-section of the unstable particle, the contributions are very small. The reason for this is a cancellation of large logarithms ($\sim \log(\Gamma_t/M_t)$) between such real and virtual corrections, leaving residual terms of $\mathcal{O}(\Gamma_t/M_t)$ [50, 51]. For top quark

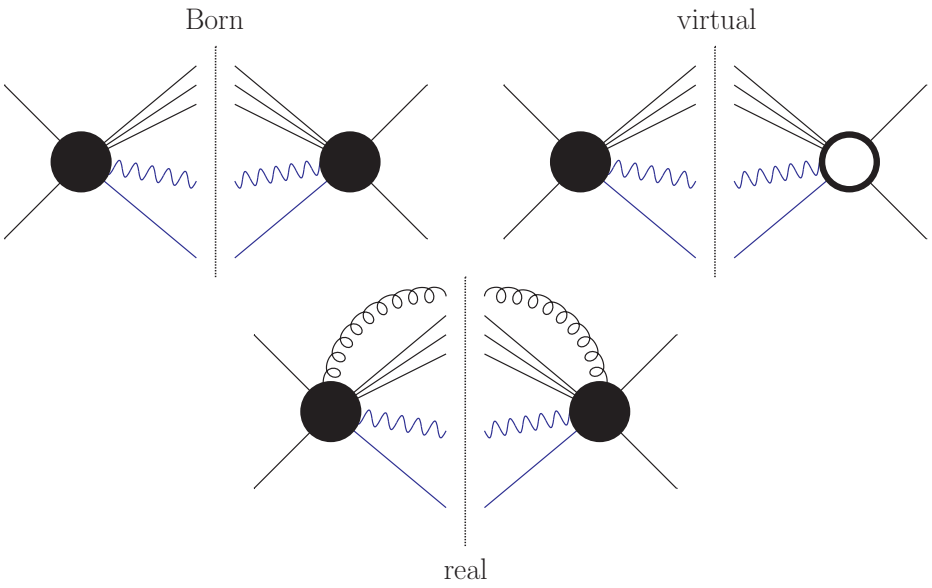

Figure 4.2: Schematic diagrams of corrections required when the unstable heavy particle, X, is fully off-shell.

production, this amounts to an effect of $\lesssim 1-2\%$ for the total cross-section. This is one of the justifications for the use of the iNWA in the calculation of unstable particle production and decay.

A priori, however, it is not clear whether the cancellation between real and virtual contributions, demonstrated in [50, 51], remains for less inclusive observables and distributions. For the case of top quarks, it would be highly desirable to have such effects under control, especially given the unique opportunity provided by the LHC and Tevatron for precision top studies. Moreover, it is essential to include this set of corrections if we are to determine the value of top mass to a precision better than $\sim \Gamma_t$.

4.3.2 The Complex Mass Scheme

As mentioned, the shift in the mass, $M_X^2 \to \mu_X^2$ required to overcome the non-integrable singularity around $p_X^2 = M_X^2$ requires care so as not to spoil the gauge-invariance of the matrix elements. One possible way around this at NLO is to

introduce the complex mass consistently at the level of the Lagrangian via a new renormalization scheme known as the Complex Mass Scheme (CMS) [52]. Here, the unstable particle's bare mass is split into a complex renormalized mass and a corresponding complex counter-term,

$$M_{X,0}^2 = \mu_X^2 + \delta\mu_X^2. \tag{4.16}$$

The unstable particle's bare field has the same form as previously[2],

$$X_0 = (1 + \frac{1}{2}\delta Z_X)X. \tag{4.17}$$

Introduction of these complex renormalized fields and masses for all unstable particles of the Lagrangian leads to Feynman rules for renormalized vertices and counter-terms that are complex. Standard perturbation theory can then be carried out with these new Feynman rules. Clearly, the CMS implies that evaluation of integrals with complex internal masses will be required for loop diagrams.

The counter-terms are fixed by the choice of conditions which in this case are a generalization of the on-shell scheme, leading to [52],

$$\delta\mu_X^2 = \Sigma_X(\mu_X^2) \quad \text{and} \quad \delta Z_X = -\Sigma'(\mu_X^2), \tag{4.18}$$

i.e. the same as the on-shell scheme except that the self-energy Σ_X is evaluated with the complex mass, μ_X^2.

The consistent insertion of complex masses in the Lagrangian using the CMS scheme ensures that Ward Identities are satisfied exactly at NLO, thus explicitly preserving gauge invariance. The authors of [52] are confident that the CMS scheme can be generalized to higher orders.

Though standard perturbation theory methods can be employed when using the CMS, its use in NLO calculations still requires the computation of all background diagrams and corrections to these - a book-keeping feat made even more challenging when all Feynman rules for vertices and counterterms are complex. Another, perhaps undesirable feature, is that as all unstable particle masses are rendered complex, all associated propagators contain the effects of an all-orders

[2] X here is assumed to be a fermion or a vector boson.

resummation of self-energies, irrespective of whether or not this is appropriate. For example, in t-channel propagators (such as in t-channel single-top production) this is not necessary.

4.3.3 The Pole Expansion

If we are interested in kinematic regions where the unstable particles are near their mass-shell, i.e. resonant, then a method developed in the early 1990's provides a consistent and gauge-invariant way of performing resummation of the unstable particle propagator. This method is the *pole expansion* [53, 54].

We again recall that a fixed-order amplitude runs into a non-integrable singularity in the resonant region, $p_X^2 \to M_X^2$. Simply resumming the fixed (l^{th}) order self-energy, $\overline{\Sigma}_X^l(p_X^2)$, to all orders, thus 'fixing' this problem via the shift $p_X^2 - M_X^2 \to p_X^2 - M_X^2 - \overline{\Sigma}_X^l(p_X^2)$, yields a gauge-dependent amplitude. This is due to the gauge dependence of $\overline{\Sigma}_X^l(p_X^2)$ and is only cancelled by higher order contributions in the perturbative expansion.

The problem here stems from trying to cure a fixed-order calculation in an *ad hoc* manner through the insertion of a shift in mass (albeit physically motivated). A better approach would be to start from an expression that is valid in the kinematic region we are interested in and extract the amplitudes we require up to the precision desired. The pole expansion provides the first step in this direction.

The starting point is the amplitude for a process, correct to *all orders* in the couplings,

$$\mathcal{A}(p_X^2) = \frac{\omega(p_X^2)}{p_X^2 - \bar{s}_X} + n(p_X^2). \tag{4.19}$$

Here $\bar{s}_X$ is the physical complex pole of the amplitude, defined through the solution(s) to $\bar{s}_X - M_X^2 - \overline{\Sigma}_X(\bar{s}_X) = 0$ (with $\overline{\Sigma}_X$ the all orders 1PI self-energy of X). $\omega(p_X^2)$ is the residue at this pole and $n(p_X^2)$ is the non-resonant piece. These three parts are all physical gauge-invariant quantities. The amplitude $\mathcal{A}$ is clearly gauge-invariant as there has been no expansion in coupling constants.

Expanding about the physical parameter $\bar{s}_X$ results in an order by order gauge-

invariant expansion, whose leading term is

$$\mathcal{A}(p_X^2) = \frac{\omega(\bar{s}_X)}{p_X^2 - \bar{s}_X} + \mathcal{O}((p^2 - \bar{s}_X)^0). \tag{4.20}$$

In principle, this can now be expanded in the coupling(s) α to any fixed order we wish. The expression obtained through this is guaranteed to be gauge-invariant as well as valid in the resonant region. The task now turns to computing the $\mathcal{O}(\alpha)$, say, corrections in the expansion above in practise, using results from what is calculable, that is, from perturbation theory.

At LO all that is required is the tree-level on-shell production and decay amplitude as well as the leading self-energy (which is $\mathcal{O}(\alpha)$). At NLO there are corrections from both virtual and real-emission diagrams and the contributions from each can be classed into factorizable and non-factorizable. At $\mathcal{O}(\alpha)$, the factorizable parts are essentially those corresponding to one-loop corrections or single-emission corrections to the on-shell production or decay subprocesses. The non-factorizable contributions are slightly more subtle. From the virtual diagrams not involving an explicit $1/(p_X^2 - M_X^2)$ propagator (these would go into the virtual-factorizable corrections), one must extract *only* the terms that diverge as $1/(p_X^2 - M_X^2)$. These could for example be found in diagrams involving propagators of the form $1/((p_X + k)^2 - M_X^2)$, where k is the loop momentum, in the region where $k \to 0$. For the real non-factorizable corrections, as with the virtuals, only the contributions that diverge as $1/(p_X^2 - M_X^2)$ must be extracted. The self-energy at two loops is also required to achieve $\mathcal{O}(\alpha)$ accuracy.

The process of extracting the correct pieces from standard perturbation theory to insert into (4.20) can be cumbersome. In particular, care must be taken to use the correct pieces for the non-factorizable terms. This is not trivial; for example, for loop diagrams this involves intricate manipulation of integrals to obtain only the terms required. However, as will be explained in detail in the forthcoming chapter, adopting ideas from ETs and making use of the method of regions simplifies the problem of extracting the correct terms from loop diagrams to one of book-keeping. In addition, we will see that an ET approach is almost a natural way to implement the pole expansion in practice.

Finally, if there are multiple unstable particles present, then the pole expan-

sion must be performed once for each unstable particle. This will be illustrated in detail for the case of top-pair production.

4.3.3.1 Potential Limitations

As can be seen from (4.20), the residue $\omega(p_X^2)$ is to be evaluated *on-shell* in the pole expansion, i.e. with $p_X^2 = \bar{s}_X$. In practice, a projection must be made from the off-shell phase space to the on-shell one that must be used for evaluation. This projection is arbitrary and the results obtained with different projections are expected to vary slightly. This variation however should be of $\mathcal{O}(\alpha\Gamma_X/M_X)$ [54] relative to the precision to which we work.

As mentioned above, the starting-point for the pole expansion method is an expression valid in the region where p_X^2 is near the physical pole $\bar{s}_X$. Here, the relevant expansion parameter is $p_X^2 - \bar{s}_X$. Near threshold regions this will in general pose problems. More specifically, unless p_X^2 actually corresponds to the partonic centre of mass energy, $\hat{s}$, the pole expansion is simply not equipped to describe these regions correctly. In threshold regions, the appropriate expansion parameter is $\beta = \sqrt{1 - \hat{s}/\bar{s}_X}$ and it is only an expansion in β that captures the behaviour correctly. A possible solution would be to switch to a Non-Relativistic Effective Theory to describe the process in this region, however this is beyond the scope of the work presented here. The assumption will be that the unstable particle, X (or the system of unstable particles, in the case where multiple unstable particles are produced), is always at least a few widths away from threshold. This can be enforced with a physical cut on the final states.

4.3.4 Off-Shell Top-Pair Literature

The NLO QCD corrections to the process involving a pair of fully off-shell top quarks, i.e. the $W^- b W^+ \bar{b}$ production process, was recently calculated by two groups [55, 56, 57][3] using the Complex Mass Scheme. These calculations are impressive even if only considering the complexity of the computations involved:

[3]The calculation of [57] also included effects of off-shell W-bosons. The differences between treating the Ws as off-shell and on-shell (iNWA) were observed not to exceed 0.5% for all differential observables dominated by resonant top-quarks examined therein.

over one thousand one-loop diagrams (involving over eighty pentagons and over twenty hexagons) were evaluated. The two papers demonstrated that the difference in the total cross-section between treating the top on- or off-shell is of the order of 1%, both at Tevatron and LHC energies, i.e. $\mathcal{O}(\Gamma_t/M_t)$, as expected by the cancellation theorems [50, 51].

A detailed comparison of the full finite-top-width and iNWA predictions was made in [58]. The latter study highlighted that for 'standard' Tevatron and LHC experimental cuts, the full and iNWA yield inclusive cross-sections for $W^+ b W^- \bar{b}$ production that differ by at most 1%. However, for differential observables, for example the p_T-distribution of the $b\bar{b}$-system, the effects can reach up to 20-30% in the tails of distributions. It is also clear that placing invariant-mass cuts of the form $M_{\rm inv}(W^+ + J_b) > 200$ GeV would greatly enhance the contributions of both single- and non-resonant subprocesses and therefore also the contrast with the iNWA predictions.

4.4 Scales in Processes involving Top Quarks

At this point we appeal to ideas from ETs to argue that scattering amplitudes for processes involving unstable top quarks are dominated only by certain contributions and many others do not play as significant a role.

Since the top quark decays in typical space-time scales of $1/\Gamma_t$, top quark production and subsequent decay subprocesses are also separated by such large(ish) scales. Thus, possible QCD connections between production and decay can only be significant when emitted gluons induce long-range interactions, i.e. only when the gluons are soft, $p_g \sim \Gamma_t$. Hard gluons on the contrary can only generate short-range interactions and so cannot affect subprocesses separated by an unstable top.

It would be optimal were it possible to exploit this physical observation to simplify calculations involving unstable top quarks. From an ET viewpoint, one would utilize the physical scales present and perform an expansion of the full amplitudes in ratios of these scales (provided these ratios were small enough). For the present scenario, the two physical scales are Γ_t and M_t and it would be desirable to expand full amplitudes in the ratio Γ_t/M_t.

It is possible to parametrize top quark virtualities through the kinematic variable, Δ_t,

$$\Delta_t := p_t^2 - \mu_t^2. \tag{4.21}$$

In the region where top quarks are resonant we have

$$\frac{\Delta_t}{M_t^2} \sim \frac{M_t \Gamma_t}{M_t^2} \sim \frac{\Gamma_t}{M_t} \ll 1. \tag{4.22}$$

It is then clear that an expansion in Γ_t/M_t also corresponds to an expansion in the top quark virtualities in such regions. Furthermore, scattering amplitudes are dominated by the leading terms in such an expansion, i.e. by subprocesses that involve resonant top quark propagators. Processes not involving unstable top quarks will be sub-leading in such an expansion, being accompanied by higher powers of Δ_t. Schematic diagrams that would yield leading contributions in an expansion are depicted in Figure 4.3.

The reason behind the Born-level schematic diagram not involving a top quark line is related to consistent ET counting. It may be that the leading parts of some non-resonant diagrams scale as the leading NLO corrections, and thus must be included for consistency.

Such an ET approach would allow one to systematically calculate the relevant contributions to the process desired. This would significantly simplify the inclusion of off-shell effects for unstable heavy particles compared to the standard fixed order NLO approach. Furthermore, extending calculations for the processes considered here beyond NLO looks to be an almost impossible task using standard approaches at present. Making full use of the physical information provided, as advocated here, provides an inroad to computing higher-order corrections (though even in an ET approach this would undoubtedly be a very challenging problem). The application of these concepts at NLO are formalized and their use in practice is discussed at length later on.

4.4.1 Resonant Single Top Production

The application of ET concepts to the study of higher-order corrections to the production of unstable particles was first examined in [59, 60]. The methods were further developed for W-pair production near threshold in e^+e^--collisions in [61] and first applied to a hadron collider process for single-top production [62, 63].

Computing the process $u\,b \to W^+bd$ at NLO in QCD, by brute force, requires roughly a factor of 8 more diagrams than that of the calculation of [62, 63]. The ET methods allowed the authors to identify the dominant corrections prior to the evaluation of any loop or real-emission diagrams thus resulting in a significant reduction of the computational complexity. The off-shell effects were studied in detail and, importantly, extensive comparison to the relevant on-shell calculations (both NWA and iNWA) were made. The effects on the total cross-section as well as many distributions were of the order of 1-2%, as expected for observables inclusive in the invariant mass of the top. However, for more exclusive observables and in particular near the edges of some distributions, differences of up to 10% from the on-shell predictions were observed.

In addition, through the use of ET methods, important steps were made in separating contributions that naturally live at the (widely-separated) hard and soft scales of the process. The presence of such scales leads to the presence of large logarithms (of the ratio of these scales) in perturbation theory. Complete separation of such contributions may allow for a resummation of these large logarithms and progress towards this is reported further on. Having control of the effects of these large logarithms is highly desirable and it should be noted that such a separation is non-trivial to achieve when using standard fixed-order perturbation theory.

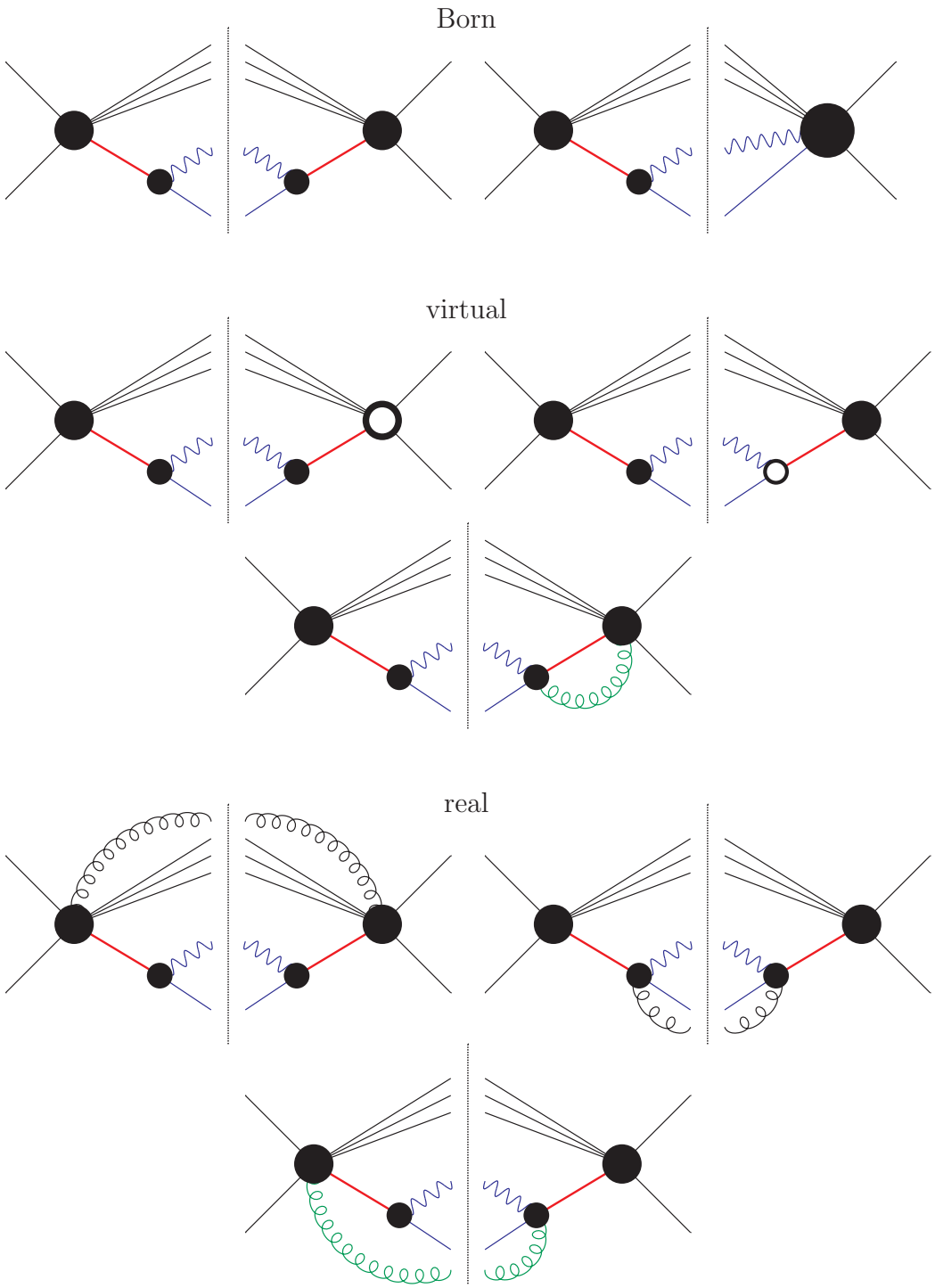

Figure 4.3: Schematic diagrams of corrections required when the unstable heavy particle, X, is resonant, i.e. $p_X^2 \neq M_X^2$, but $p_X^2 \sim M_X^2$. Loops connecting production and decay as well as interferences between real emissions production and decay must be included.

Chapter 5

Resonant $t\bar{t}$ Production at NLO

The method fusing the pole expansion with ideas from Effective Theories is presented in this chapter by means of the example of unstable, resonant top-pair production at hadron colliders. Many of the methods have been carried on and further developed from the work on single top production published in [62, 63] as well as thoroughly documented in the PhD Thesis of Paul Mellor. A new treatment of the real corrections is described which allows for the clean split of NLO corrections into factorizable and non-factorizable corrections.

The condition that the $t\bar{t}$ system is at least a few widths away from threshold will be assumed throughout this chapter, unless otherwise stated. This is to ensure the validity of the pole expansion. The reasons for the breakdown of the method near and below threshold will be discussed.

5.1 Processes

In the introduction it was noted that top-pair production comes about via both $q\bar{q}$ and gg initial states at hadron colliders. Here the focus will be on computing the dominant NLO QCD corrections to $q\bar{q} \to W^+bW^-\bar{b}$ production in the resonant region, i.e. where $(p_{W^+} + p_b)^2 \sim (p_{W^-} + p_{\bar{b}})^2 \sim M_t^2$. The double resonant subprocess at tree-level is depicted in Figure 5.1. The $q\bar{q}$-initiated process is the dominant one at the Tevatron proton anti-proton collider, however it also plays an important role at the LHC at CERN. To fully describe this process of course, one

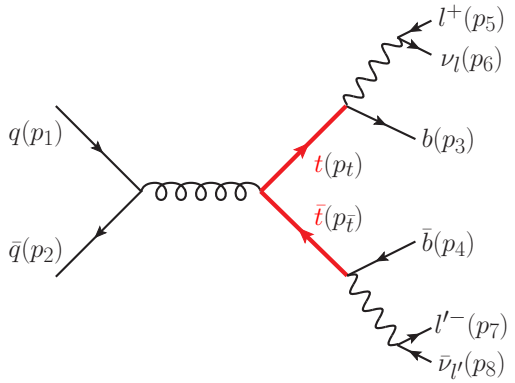

Figure 5.1: Double resonant diagram for $q\bar{q} \to b\, l^+\, \nu_l\, \bar{b}\, l'^-\, \bar{\nu}_{l'}$

must also include the gg-initiated processes (as well as the qg- and $\bar{q}g$-initiated processes, which enter at NLO).

5.2 Notation

First we set up the notation to be used in this chapter. The momenta are as labelled in Figure 5.1, with the top quark momenta given by

$$p_t = p_3 + p_5 + p_6 \qquad p_{\bar{t}} = p_4 + p_7 + p_8 \tag{5.1}$$

$$p_{t9} = p_3 + p_5 + p_6 + p_9 \qquad p_{\bar{t}9} = p_4 + p_7 + p_8 + p_9. \tag{5.2}$$

The momentum p_9 is that of the additional gluon radiation present in the real corrections at NLO. In what follows, the b-quarks are taken to be massless, i.e. $p_3^2 = p_4^2 = 0$. We also define terms denoting the denominators of top quark propagators (standard and resummed) by

$$D_t = p_t^2 - M_t^2 \qquad D_{\bar{t}} = p_{\bar{t}}^2 - M_t^2 \tag{5.3}$$

$$D_{t9} = p_{t9}^2 - M_t^2 \qquad D_{\bar{t}9} = p_{\bar{t}9}^2 - M_t^2 \tag{5.4}$$

$$\Delta_t = p_t^2 - \mu_t^2 \qquad \Delta_{\bar{t}} = p_{\bar{t}}^2 - \mu_t^2 \tag{5.5}$$

$$\Delta_{t9} = p_{t9}^2 - \mu_t^2 \qquad \Delta_{\bar{t}9} = p_{\bar{t}9}^2 - \mu_t^2. \tag{5.6}$$

5.3 The Pole Expansion and Effective Theory Power-Counting

As advocated in §4.3.3 a good starting-point for the computation of gauge-invariant quantities for unstable particles is the full (all orders) amplitude for the production of the associated decay products. In the case of $t\bar{t}$, where the final state is $W^+\, b\, W^-\, \bar{b}$, this full amplitude can be written as

$$\mathcal{A}_{\text{full}}(p_t^2, p_{\bar{t}}^2) = \frac{\mathcal{K}^D(p_t^2, p_{\bar{t}}^2, \{p_i\})}{(p_t^2 - \mu_t^2)(p_{\bar{t}}^2 - \mu_t^2)} + \frac{\mathcal{K}^{S,t}(p_t^2, \{p_i\})}{p_t^2 - \mu_t^2} + \frac{\mathcal{K}^{S,\bar{t}}(p_{\bar{t}}^2, \{p_i\})}{p_{\bar{t}}^2 - \mu_t^2} + \mathcal{J}(\{p_i\}). \tag{5.7}$$

Here μ_t^2 is the position of the pole of the full top quark propagator (we have called the corresponding quantity $\bar{s}_X$ in §4.3.3). $\mathcal{K}^{\mathcal{D}}$, $\mathcal{K}^{S,t(\bar{t})}$ are the residues at the double and single poles and contain the appropriate effects from double and single resonant diagrams. $\mathcal{J}$ is the non-resonant remainder.

The next step is to perform an expansion of the full amplitude about the complex poles [53, 54]. The presence of two unstable particles means we have to use a 'double pole expansion'[1], which reads:

$$\mathcal{A}^{(0)}_{\text{full}} = \frac{\mathcal{K}^D(p_t^2 = p_{\bar{t}}^2 = \mu_t^2)}{\Delta_t \Delta_{\bar{t}}} + \frac{1}{\Delta_t}\left[\mathcal{K}^{S,t}(p_t^2 = p_{\bar{t}}^2 = \mu_t^2) + \frac{\partial K^D}{\partial p_t^2}(p_t^2 = p_{\bar{t}}^2 = \mu_t^2)\right] + (t \leftrightarrow \bar{t}) + \dots \tag{5.8}$$

The term $\partial\mathcal{K}^D/\partial p_t^2$ arises from the expansion of $\mathcal{K}^D$ about $p_t^2 = \mu_t^2$ and describes single resonant contributions from double resonant diagrams. The ellipses denote an infinite series of terms suppressed by ever higher powers of Δ_t and $\Delta_{\bar{t}}$. The expression above can now be expanded in the perturbative couplings α_s and α_{ew}

[1] The double pole expansion was successfully employed to study NLO QED corrections to unstable W-pair production in e^+e^- collisions for inclusive quantities [64].

to whatever order we wish. At each order the expression is gauge-invariant and valid in the resonant region. The non-trivial task that remains is to extract from the standard perturbative expansion, the relevant pieces that should be included in the expansion of (5.8). One method of doing this is examining the Feynman diagrams and keeping only those with resonant top-quark propagators and inserting them into (5.8), evaluating the relevant amplitudes with $p_t^2 = p_{\bar{t}}^2 = \mu_t^2$. This is fairly straightforward at tree-level but becomes an increasingly delicate procedure when including higher orders (loop and real-emission diagrams).

Adopting ideas from how ETs approach the computation of scattering amplitudes it is possible to develop a framework that provides an easy and efficient way to pick out the correct pieces of standard perturbation theory for use in the pole expansion.

As a first step this involves the introduction of a power-counting scheme that will allow for the systematic expansion of Feynman diagrams in a single, generic small parameter, δ. As we will be interested in the process $q\,\bar{q} \to W^+\,b\,W^-\,\bar{b}$, the Feynman diagrams that will be examined are the relevant ones describing this process. The small parameter, δ, is identified with $\Delta_{t(\bar{t})}/M_t^2$ in the resonant region, as well as with each of the coupling constants raised to some power. In fact, the relative scalings are:

$$\frac{\Delta_t}{M_t^2} \sim \frac{\Delta_{\bar{t}}}{M_t^2} \sim \alpha_{\text{ew}} \sim \alpha_s^2 \sim \delta. \tag{5.9}$$

The first scaling $\Delta_{t(\bar{t})}/M_t^2 \sim \alpha_{\text{ew}}$ is a formal one as in the resonant region $\Delta_{t(\bar{t})} \sim \Gamma_t M_t$ and $\Gamma_t \sim \alpha_{\text{ew}} M_t$. On the other hand the second scaling $\alpha_{\text{ew}} \sim \alpha_s^2$ is a purely numerical one. Should the relative sizes of the couplings differ to the ones above, a different scaling can easily be accounted for. The power of a series in δ is that it realises a simultaneous pole expansion *and* expansion in the couplings. This combination ensures gauge invariance at each order of δ.

Powers of δ may now be associated with individual diagrams prior to their computation. The power of δ indicates how the leading part (in an expansion in $\Delta_{t(\bar{t})}$) of a diagram scales with δ. For example, by assigning powers of δ to the diagrams in Figure 5.2 following the scalings of (5.9), we can deduce that the

leading parts of each would scale as

$$\mathcal{A}^{\rm lp}_{\rm eg.(a)} \sim \alpha_s\alpha_{\rm ew}\frac{1}{\Delta_t\Delta_{\bar{t}}} \sim \frac{\delta^{\frac{1}{2}}.\delta}{\delta.\delta} \sim \delta^{-\frac{1}{2}} \tag{5.10}$$

$$\mathcal{A}^{\rm lp}_{\rm eg.(b)} \sim \alpha_s\alpha_{\rm ew}\frac{1}{\Delta_t} \sim \frac{\delta^{\frac{1}{2}}.\delta}{\delta} \sim \delta^{\frac{1}{2}} \tag{5.11}$$

$$\mathcal{A}^{\rm lp}_{\rm eg.(c)} \sim \alpha_s\alpha_{\rm ew} \sim \delta^{\frac{1}{2}}.\delta \sim \delta^{\frac{3}{2}} \tag{5.12}$$

The sum of tree-level diagrams following an expansion in δ can be written as

$$\begin{aligned}\mathcal{A}^{(0)}_{\rm tree} = \frac{1}{2}\left(\delta^{\bar{i}_3}_{i_1}\delta^{\bar{i}_2}_{i_4} - \frac{1}{N_c}\delta^{\bar{i}_2}_{i_1}\delta^{\bar{i}_3}_{i_4}\right)\alpha_s\alpha_{\rm ew}\left[A^{(1,1)}_{(-2)} + A^{(1,1)}_{(-1)} + A^{(1,1)}_{(0)} + \ldots\right] \\ + \left(\delta^{\bar{i}_2}_{i_1}\delta^{\bar{i}_3}_{i_4}\right)\alpha^2_{\rm ew}\left[A^{(0,2)}_{(-2)} + A^{(0,2)}_{(-1)} + A^{(0,2)}_{(0)} + \ldots\right]\end{aligned} \tag{5.13}$$

where $A^{(j,k)}_{-l}$ indicates the sum of contributions that have a total of l resonant top or anti-top quark propagators and are multiplied by j and k powers of α_s and $\alpha_{\rm ew}$. Thus $A^{(1,1)}_{(-2)}$ receives contributions from diagram (a) of Figure 5.2, $A^{(1,1)}_{(-1)}$ from diagrams including (b) and (a sub-leading part of) (a) of Figure 5.2 and so on. The second line in the equation above indicates the purely EW contributions to the full amplitude.

The terms in the two square brackets above (when we include the couplings), scale as $[\ \sim\delta^{-\frac{1}{2}} + \sim\delta^{\frac{1}{2}} + \sim\delta^{\frac{3}{2}} + \ldots\ ]$ and $[\sim\delta^0 + \sim\delta^1 + \sim\delta^2 + \ldots]$ once the power-counting rules are applied. The ellipses indicate terms which scale as higher powers of δ.

For the colour-averaged square amplitude, $\mathcal{M}^{\rm tree}_{\rm full}$ we have

$$\begin{aligned}\mathcal{M}^{\rm tree}_{\rm full} = \frac{C_F}{2N_c}\alpha_s^2\alpha_{\rm ew}^2\left[\left|A^{(1,1)}_{(-2)}\right|^2 + 2{\rm Re}\left\{A^{(1,1)}_{(-2)}A^{(1,1)\,*}_{(-1)}\right\} + \ldots\right] \\ + \alpha^2_{\rm ew}\left[\left|A^{(0,2)}_{(-2)}\right|^2 + \ldots\right].\end{aligned} \tag{5.14}$$

In the expression above we have kept terms that scale up to ~ 1 and the ellipses now indicate terms of order $\mathcal{O}(\delta)$ and higher. In principle there could be an

interference term of the form $2\text{Re}\left\{A^{(1,1)}_{(-2)}A^{(0,2)*}_{(-2)}\right\}$, which would scale as $\sim \delta^{-\frac{1}{2}}$. However, this vanishes as the colour interference is zero.

For a leading order (LO) calculation in δ we need only keep the first term in (5.13). This term scales as δ^{-1} and involves only the double resonant diagram, (a) of Figure 5.2. To consistently include corrections in δ we must deal with the higher order virtual and real diagrams in an appropriate manner. This will be discussed next.

The purpose of this work is to compute corrections of $\mathcal{O}(\delta^{\frac{1}{2}})$ to the leading order matrix element. That is, from the matrix element at all orders in α_s and α_{ew}, $\mathcal{M}^{\text{all-orders}}_{\text{full}}$, we must extract terms that scale as up to and including $\mathcal{O}(\delta^{-\frac{1}{2}})$. Parts suppressed by higher orders in δ can be safely ignored to this level of accuracy. Referring back to the relative scaling of small parameters in the resonant region, (5.9), it is clear that these corrections will be comprised primarily of the $\mathcal{O}(\alpha_s)$ or NLO QCD corrections. In principle, additional contributions scaling as $\delta^{-\frac{1}{2}}$ may be present in higher orders in QCD or indeed QED/EW and these should all be included for consistency. From now on we take 'NLO' to mean a correction of $\mathcal{O}(\delta^{\frac{1}{2}})$.

One-loop corrections must be interfered with the Born-level amplitude and therefore it it necessary to extract one-loop contributions that scale as ~ 1 such that the interference makes up a correction of $\mathcal{O}(\delta^{\frac{1}{2}})$ to the LO matrix element. Examples of such one-loop terms can be found in the QCD corrections to the double-resonant diagrams. The leading parts of such corrections have a power-counting of

$$\alpha_s^2\alpha_{\text{ew}}A^{(2,1)}_{(-2)} \;\sim\; \delta.\delta\frac{1}{\delta^2} \;\sim\; 1, \tag{5.15}$$

giving a contribution to the matrix element, after interfering with the tree-level amplitude of

$$\mathcal{M}^{\text{Virt}} \sim \alpha_s^3\alpha_{\text{ew}}^2 2\text{Re}\left\{A^{(2,1)}_{(-2)}A^{(1,1)\,*}_{(-2)}\right\} \;\sim\; \delta^{-\frac{1}{2}}. \tag{5.16}$$

As is necessary when using perturbation theory to make predictions that are fully differential, real-emission diagrams must be included for a correct treatment

of higher order corrections[2]. Once again, the power-counting dictates that corrections to the double-resonant Born diagrams are required. The leading parts of such diagrams will scale as

$$\alpha_s^{\frac{3}{2}} \alpha_{\text{ew}} A_{(-2)}^{(\frac{3}{2},1)} \sim \delta^{-\frac{1}{4}}, \tag{5.17}$$

and contribute to the matrix element as

$$\mathcal{M}^{\text{Real}} \sim \alpha_s^3 \alpha_{\text{ew}}^2 \left| A_{(-2)}^{(\frac{3}{2},1)} \right| \sim \delta^{-\frac{1}{2}}. \tag{5.18}$$

As will be detailed further on, the expansion of the real corrections requires some attention and is not as straightforward as the expansion of the virtual contributions.

We will now explain how the relevant pieces required for the computation of the matrix element up to $\mathcal{O}(\delta^{-\frac{1}{2}})$ are extracted from each order of the full perturbation expansion.

5.4 Born Amplitudes

As mentioned previously, it is possible to separate the diagrams for the process $q\bar{q} \to W^+ b\, W^- \bar{b}$ into three classes: double-, single- and non-resonant diagrams. Examples of such diagrams are depicted in Figure 5.2. Working to leading-order in δ only the leading piece of diagram (a) is required.

The expansion introduced in the previous section results in the following expression for the tree-level helicity amplitude (with incoming quark helicities fixed)

$$\mathcal{A}_{\text{full}}^{(0)} = \sum_{\rho=\pm} \sum_{\lambda=\pm} \frac{\mathcal{A}_{D,t}^{(0)}(t^\lambda \to W^+ b)\, \mathcal{A}_P^{(0)}(q\bar{q} \to t^{-\lambda}\, \bar{t}^\rho)\, \mathcal{A}_{D,\bar{t}}^{(0)}(\bar{t}^{-\rho} \to W^- \bar{b})}{\Delta_t \Delta_{\bar{t}}} + \mathcal{O}(\delta^{\frac{1}{2}}). \tag{5.19}$$

$A_{D,t(\bar{t})}^{(0)}$ is the tree-level amplitude describing the decay of an on-shell (anti-)top and $A_P^{(0)}$ is the tree-level amplitude for on-shell $t\bar{t}$ production. The helicity (spin)

[2]For completely inclusive quantities, the real corrections can be related to the imaginary part of the virtual correction via the Optical Theorem.

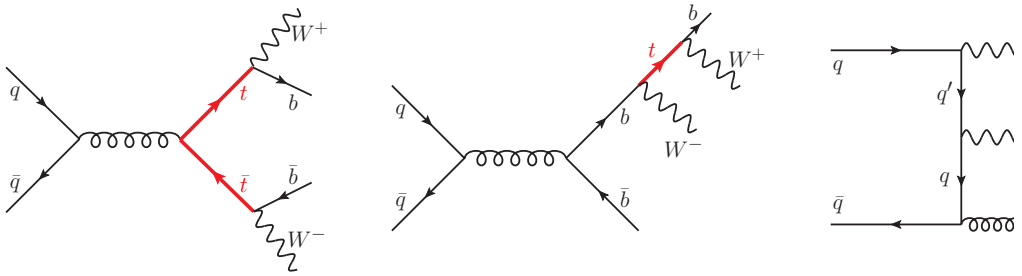

Figure 5.2: Example double-, single- and non-resonant tree-level diagrams of the process $q\bar{q} \to W^+ b W^- \bar{b}$

information of the top quarks is explicitly maintained between production and decay parts of the amplitude in the expression above. The form of the amplitudes above make them perfectly suited for calculation with the spinor helicity method and its massive extension.

More specifically, when the decay of $W^\pm$ to leptons (via the iNWA) is included, the amplitudes are given by (h_i indicates helicity)

$$\mathcal{A}^{(0)}_{D,t}(p_t^{h_t}, p_3, p_5, p_6) = g_{\text{ew}}^2 \, \delta^{\bar{i}_3}_{i_t} \, A^{(0)}_{D,t}(p_t^{h_t}, p_3, p_5, p_6) \tag{5.20}$$

$$\mathcal{A}^{(0)}_{D,\bar{t}}(p_{\bar{t}}^{h_{\bar{t}}}, p_4, p_7, p_8) = g_{\text{ew}}^2 \, \delta^{\bar{i}_{\bar{t}}}_{i_4} \, A^{(0)}_{D,\bar{t}}(p_{\bar{t}}^{h_{\bar{t}}}, p_4, p_7, p_8) \tag{5.21}$$

$$\mathcal{A}^{(0)}_{P}(p_1^{h_q}, p_2^{-h_q}, p_t^{h_t}, p_{\bar{t}}^{h_{\bar{t}}}) = g_s^2 \, \frac{1}{2} \left(\delta^{\bar{i}_t}_{i_1} \delta^{\bar{i}_2}_{i_{\bar{t}}} - \frac{1}{N_c} \delta^{\bar{i}_2}_{i_1} \delta^{\bar{i}_t}_{i_{\bar{t}}} \right) \, A^{(0)}_{P}(p_1^{h_q}, p_2^{-h_q}, p_t^{h_t}, p_{\bar{t}}^{h_{\bar{t}}}) \tag{5.22}$$

where

$$A^{(0)}_{D,t}(p_t^+, p_3, p_5, p_6) = \frac{\langle 3\,6\rangle \, \langle \eta_3 | \, p_t \, | 5]}{\langle 3^\flat \, \eta_3 \rangle} \frac{1}{\sqrt{2 M_W \Gamma_W}} \tag{5.23}$$

$$A^{(0)}_{D,\bar{t}}(p_{\bar{t}}^-, p_4, p_7, p_8) = -\frac{\langle 7 | \, p_{\bar{t}} \, | \eta_4] \, [4\,8]}{[\eta_4 \, 4^\flat]} \frac{1}{\sqrt{2 M_W \Gamma_W}} \tag{5.24}$$

$$A^{(0)}_{P}(p_1^-, p_2^+, p_t^-, p_{\bar{t}}^+) = -2 \, \frac{\langle 2 | \, p_t \, | \eta_3] \, \langle \eta_4 | \, p_{\bar{t}} \, | 1] + M_t^2 \, \langle 2 \, \eta_4 \rangle \, [1 \, \eta_3]}{s_{12} \, [3^\flat \, \eta_3] \, [4^\flat \, \eta_4]}. \tag{5.25}$$

The momentum labels are as depicted in Figure 5.1. The momenta $3^\flat$ ($4^\flat$) and

η_3 (η_4) correspond to the light-like momenta that the top momentum, p_t ($p_{\bar{t}}$) has been decomposed into (see §2.1.2.1).

All other helicity configurations can be deduced from the expressions above. However, choosing $\eta_3 = p_5$ and $\eta_4 = p_7$ the amplitudes $A^{(0)}_{D,t}(p_t^-, p_3, p_5, p_6)$ and $A^{(0)}_{D,\bar{t}}(p_{\bar{t}}^+, p_4, p_7, p_8)$ vanish. Thus the sum over all possible top and anti-top helicities in (5.19) reduces to a single term, with only the production amplitude with p_t^- and $p_{\bar{t}}^+$ required. Of course, for the matrix element, the helicity amplitude with the helicities of the incoming quarks swapped is also needed; this can be obtained from the amplitude above via charge conjugation and results in $A^{(0)}_P(p_1^+, p_2^-, p_t^-, p_{\bar{t}}^+)$ having the same expression as (5.25) with the swap $1 \leftrightarrow 2$.

It is noted that is has been possible to write the leading contribution to the pole expansion in this factorized form due to the fact that the pole expansion dictates that the residue of the pole must be evaluated *on-shell*. As a result, we are able to introduce a complete set of states for the numerator of the top quark propagators, thus achieving the form of (5.19), much akin to the iNWA structure of (4.10). Here it is appropriate to make the point that the on-shell condition $p_t^2 = \mu_t^2$ can also be re-expressed as a series in δ. Explicitly this is $p_t^2 = \mu_t^2 \simeq M_t^2 + \mathcal{O}(\alpha_{\text{ew}}) = M_t^2 + \mathcal{O}(\delta)$. To obtain the accuracy we aim for it is sufficient to drop the $\mathcal{O}(\delta)$ pieces of the on-shell condition and simply take $p_t^2 = M_t^2$.

5.5 One-Loop Amplitudes

A selection of one-loop corrections to the double-resonant tree-level diagram, Figure 5.1 is shown in Figure 5.3. For a NLO calculation of $q\bar{q} \to W^+ b\, W^- \bar{b}$ where $(p_W + p_b)^2 \neq M_t^2$, the full set of one-loop corrections to *all* tree-level (including single and non-resonant diagrams) would be required. In the resonant region however, we will argue that the corrections we need to include are the corrections to the double-resonant Born diagrams. It is important to re-iterate that we should only keep the parts of these diagrams that scale as ~ 1.

In order to pick out these relevant pieces it is necessary to be able to perform an expansion in δ. The tool used to do this is the method of regions (see §2.1.4), whereby the diagrams must be expanded in the *hard* ($k_0 \sim \vec{k} \sim M_t$) and *soft*

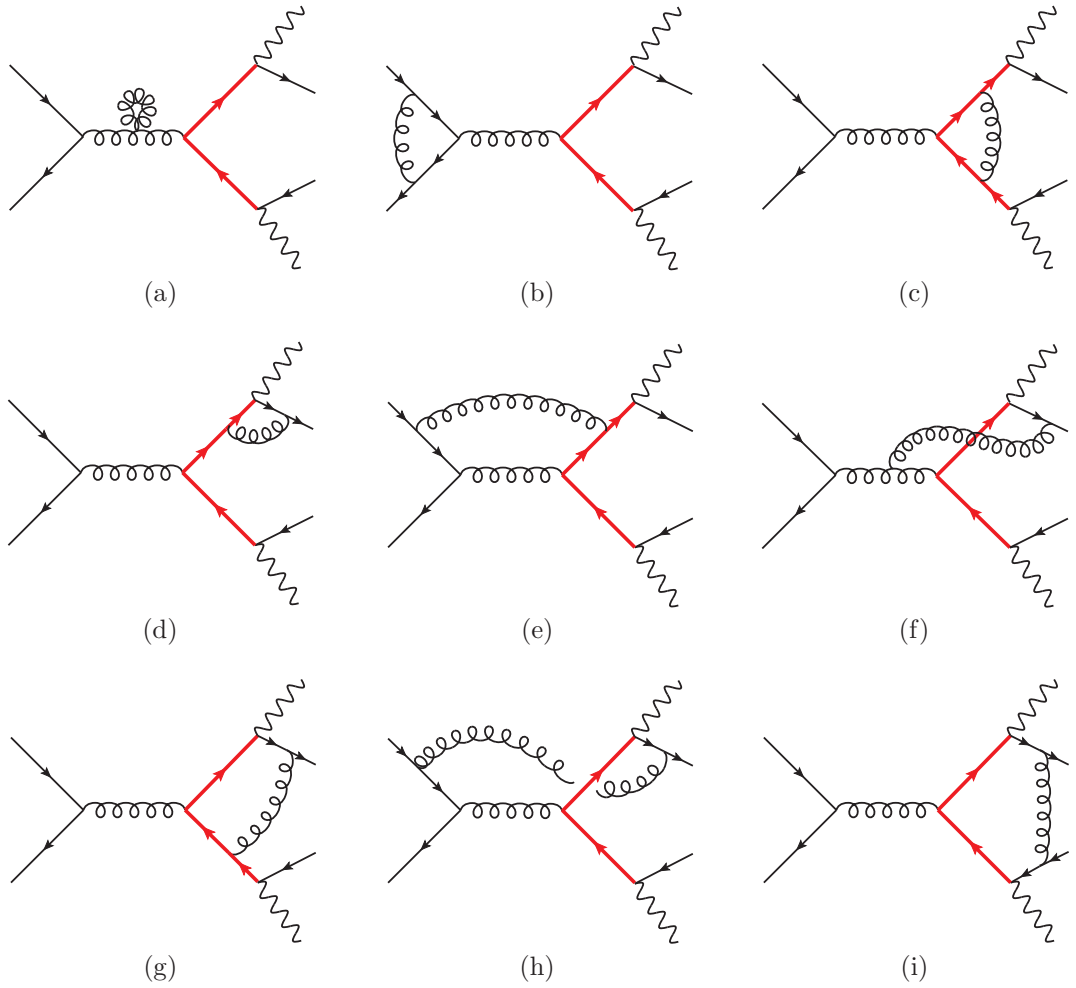

Figure 5.3: Selection of 1-loop corrections to the double resonant diagram of the process $q\bar{q} \rightarrow W^+ b\, W^- \bar{b}$

$(k_0 \sim \vec{k} \sim \delta\, M_t)$ regions. Factors of M_t are suppressed in the power-counting to ease arguments in the forthcoming discussion.

5.5.1 Power-Counting

Prior to computing hard and soft integrals resulting from an expansion in regions, we can apply the same power-counting rules introduced earlier to obtain the scalings of the leading terms in the expansions.

For clarity we will run through an example, examining how the application of the expansion by regions and power-counting works for diagram (c) of Figure 5.3. Using the Feynman rules, diagram (c) is given by the following expression

$$\mathcal{A}^{(1)}_{(c)} = \alpha_s^2\,\alpha_{\rm ew}\ldots\frac{1}{\Delta_t\,\Delta_{\bar{t}}}\int[dk]\,\frac{\gamma^\mu\,(\not{p}_t-\not{k}+M_t)\,\gamma_\rho\,(\not{p}_{\bar{t}}+\not{k}-M_t)\,\gamma_\mu}{k^2\;((p_t-k)^2-M_t^2)\,((p_{\bar{t}}+k)^2-M_t^2)}\;\ldots \tag{5.26}$$

In the hard region, the denominator of the top-quark propagator, upon expansion, simplifies to

$$(p_t-k)^2-M_t^2 = k^2-2k.p_t+D_t\;\rightarrow\;k^2-2k.p_t. \tag{5.27}$$

In this region the top propagators in the loop cannot be resonant and the resulting expression for the leading hard term of full diagram becomes

$$\mathcal{A}^{(1)}_{(c),\rm hard} = \alpha_s^2\,\alpha_{\rm ew}\ldots\frac{1}{\Delta_t\,\Delta_{\bar{t}}}\int[dk]\,\frac{\gamma^\mu\,(\not{p}_t-\not{k}+M_t)\,\gamma_\rho\,(\not{p}_{\bar{t}}+\not{k}-M_t)\,\gamma_\mu}{k^2\;(k^2-2k.p_t)\,(k^2+2k.p_{\bar{t}})}\;\ldots \tag{5.28}$$

Applying the same power-counting rules as before to the expression above we find the scaling

$$\mathcal{A}^{(1)}_{(c),\rm hard}\sim\delta\,.\,\delta\,.\frac{1}{\delta\,.\,\delta}.\,1\,.\frac{1}{1\,.\,1\,.\,1}\;\sim 1 \tag{5.29}$$

as in the hard region $[dk]\sim 1$, $k^2\sim 1$, $k.p_t\sim k.p_{\bar{t}}\sim 1$.

In the soft region, the top-quark propagators are expanded slightly differently, leading to the denominators taking the form

$$(p_t-k)^2-M_t^2 = k^2-2k.p_t+D_t\;\rightarrow\;-2k.p_t+\Delta_t. \tag{5.30}$$

In the soft region it is evident that the top propagators are still resonant (scale as $\sim\delta^{-1}$) and thus the shift $D_t\rightarrow\Delta_t$ must be performed in order that propagator resummation effects are consistently included. The leading soft term of diagram

Diagram	Hard	Soft
a	1	0 (tadpole)
b	1	0 (tadpole)
c	1	1
d	1	1
e	1	1
f	δ	δ
g	δ	1
h	δ	1
i	δ^2	1

Table 5.1: Power-counting for leading hard and soft contributions of double-resonant one-loop diagrams.

(c) is thus

$$\mathcal{A}^{(1)}_{(c),\text{soft}} = \alpha_s^2\,\alpha_{\text{ew}}\ldots\frac{1}{\Delta_t\,\Delta_{\bar{t}}}\int[dk]\,\frac{\gamma^\mu\,(\not{p}_t+M_t)\,\gamma_\rho\,(\not{p}_{\bar{t}}-M_t)\,\gamma_\mu}{k^2\;(-2k.p_t+\Delta_t)\,(2k.p_{\bar{t}}+\Delta_{\bar{t}})}\;\ldots \tag{5.31}$$

which then scales as

$$\mathcal{A}^{(1)}_{(c),\text{soft}} \sim \delta\,.\,\delta\,.\frac{1}{\delta\,.\,\delta}.\,\delta^4\,.\frac{1}{\delta^2\,.\,\delta\,.\,\delta}\;\sim 1. \tag{5.32}$$

This scaling is obtained from the fact that in the soft region $[dk]\sim\delta^4$, $k^2\sim\delta^2$ and $k.p_t\sim k.p_{\bar{t}}\sim\delta$. We also note that the k-terms in the numerator have disappeared as they yield expressions that are suppressed by higher powers of δ.

Repeating this procedure for all diagrams in Figure 5.3 results in the scalings of Table 5.1. The power-counting tells us that for diagrams (f)-(i) the hard parts are beyond the order to which we work. The soft part of diagram (f) can also be safely discarded. This leads to significant simplification of the one-loop contributions as, in particular, only the soft parts of the pentagon and hexagon diagrams must be included.

Due to the number of resonant top-quark propagators, it is clear that one-loop corrections to single-resonant (non-resonant) Born diagrams will be suppressed by a factor of δ (δ^2) relative to the corrections to double-resonant Born diagrams.

Multiplying the scalings in Table 5.1 by δ (δ^2) we see that the leading hard and soft contributions from the former set of corrections are well beyond our target accuracy.

Similarly, QED/EW corrections as well as higher order QCD loops will in general be suppressed by at least a factor of $\alpha_s \sim \delta^{\frac{1}{2}}$ relative to the terms in Table 5.1 and so can be safely disregarded. However, care must be taken to ensure this is really the case; we will see a little later that self-energy corrections to the top propagators will require special attention.

5.5.2 Factorizable Corrections

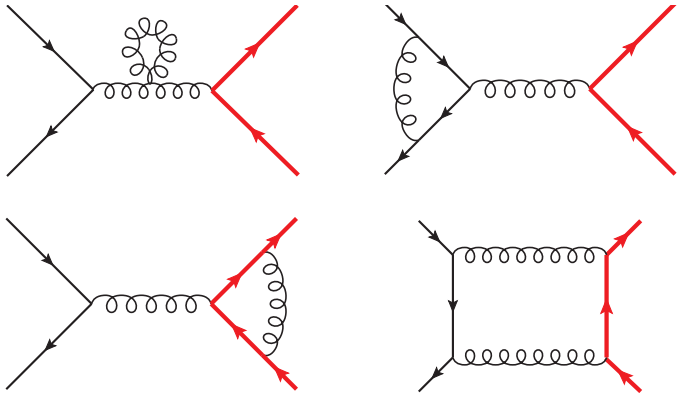

Figure 5.4: Selection of one-loop corrections to the on-shell production process: $q\bar{q} \to t\bar{t}$. These correspond to the factorizable corrections of $q\bar{q} \to W^+ b\, W^- \bar{b}$ arising from the $t\bar{t}$ production subprocess.

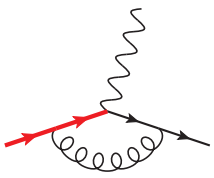

Figure 5.5: One-loop correction to the on-shell decay process: $t \to W^+ b$. This corresponds to the factorizable corrections of $q\bar{q} \to W^+ b\, W^- \bar{b}$ arising from the $t(\bar{t})$ decay subprocess.

A close inspection of the hard corrections that must be included reveals that

they correspond exactly to the one-loop corrections to the production process $q\bar{q} \to t\bar{t}$ or the decay process $t \to W^+ b$ (or $\bar{t} \to W^- \bar{b}$). Relevant Feynman diagrams for these factorizable corrections are shown in Figures 5.4 and 5.5 respectively. The production and decay subprocesses linked as in the iNWA (the difference being that the denominators of the top propagators are evaluated off-shell). This can be seen explicitly in (5.28). This is a general result and it is precisely these hard corrections to production and decay subprocesses that formally define the factorizable corrections. The pole expansion combined with the method of regions provides a gauge-invariant separation of these corrections [59] in contrast to a naive compilation of factorizable corrections selected on a diagram by diagram basis, which is on the whole not gauge-invariant.

Finally, we write down the structure of the factorizable corrections (or the leading hard corrections).

$$\begin{aligned}\mathcal{A}^{(\text{1-loop})}_{\text{hard}} = \sum_{\lambda=\pm}\sum_{\rho=\pm}\Bigg\{ & \frac{\mathcal{A}^{(1)}_{D,t}(t^\lambda \to W^+ b)\, \mathcal{A}^{(0)}_{P}(q\bar{q} \to t^{-\lambda}\, \bar{t}^{\rho})\, \mathcal{A}^{(0)}_{D,\bar{t}}(\bar{t}^{-\rho} \to W^- \bar{b})}{\Delta_t \Delta_{\bar{t}}} \\ & + \frac{\mathcal{A}^{(0)}_{D,t}(t^\lambda \to W^+ b)\, \mathcal{A}^{(1)}_{P}(q\bar{q} \to t^{-\lambda}\, \bar{t}^{\rho})\, \mathcal{A}^{(0)}_{D,\bar{t}}(\bar{t}^{-\rho} \to W^- \bar{b})}{\Delta_t \Delta_{\bar{t}}} \\ & + \frac{\mathcal{A}^{(0)}_{D,t}(t^\lambda \to W^+ b)\, \mathcal{A}^{(0)}_{P}(q\bar{q} \to t^{-\lambda}\, \bar{t}^{\rho})\, \mathcal{A}^{(1)}_{D,\bar{t}}(\bar{t}^{-\rho} \to W^- \bar{b})}{\Delta_t \Delta_{\bar{t}}} \Bigg\} \\ & + \mathcal{O}(\delta^{\frac{1}{2}}). \end{aligned} \tag{5.33}$$

The superscript (1) indicates that the amplitude for the on-shell subprocess (production or decay) should be computed at one-loop.

The one-loop production amplitudes $\mathcal{A}^{(1)}_P$ have the structure

$$\begin{aligned}\mathcal{A}^{(1)}_P(1_q, 2_{\bar{q}}, p_t, p_{\bar{t}}) = g_s^4 \Bigg\{ & \frac{N_c}{2}\, \delta^{\bar{i}_3}_{i_1} \delta^{\bar{i}_2}_{i_4}\, A^{(1)}_{P;1}(1_q, 2_{\bar{q}}, p_t, p_{\bar{t}}) \\ & + \frac{1}{2}\, \delta^{\bar{i}_2}_{i_1} \delta^{\bar{i}_3}_{i_4}\, A^{(1)}_{P;2}(1_q, 2_{\bar{q}}, p_t, p_{\bar{t}}) \Bigg\} \end{aligned} \tag{5.34}$$

where the subamplitudes can be further decomposed into so-called primitive amplitudes as [48, 15]

$$\begin{aligned} A^{(1)}_{P;1}(1_q, 2_{\bar{q}}, p_t, p_{\bar{t}}) = {} & A^{[lc]}_P(1_q, 2_{\bar{q}}, p_t, p_{\bar{t}}) \\ & - \frac{1}{N_c}\left(N_f\, A^{[f]}_P(1_q, 2_{\bar{q}}, p_t, p_{\bar{t}}) + N_h\, A^{[h]}_P(1_q, 2_{\bar{q}}, p_t, p_{\bar{t}})\right) \\ & - \frac{2}{N_c^2}\left(A^{[lc]}_P(1_q, 2_{\bar{q}}, p_t, p_{\bar{t}}) - A^{[lc]}_P(2_{\bar{q}}, 1_q, p_t, p_{\bar{t}})\right) \\ & - \frac{1}{N_c^2} A^{[slc]}_P(1_q, 2_{\bar{q}}, p_t, p_{\bar{t}}) \end{aligned} \tag{5.35}$$

where amplitudes are labelled by lc, slc, f and h for the leading colour, subleading colour light and heavy fermion contributions respectively. For further details and full expressions for all these primitive amplitudes we refer to the paper by Badger, Sattler and Yundin [15] in which compact expressions for the helicity amplitudes for on-shell $t\bar{t}$ production have been computed. We note that the expression for the sub-amplitude $A^{(1)}_{P;2}$ is not required; due to colour it does not interfere with the tree-level amplitude.

The one-loop helicity amplitude for the decays of the top and anti-top quarks,

$$\mathcal{A}^{(1)}_{D,t}(p_t, 3_b, 5_{l^+}, 6_{\nu_l}) = g_s^2\, g_{\text{ew}}^2\, C_F \frac{1}{\sqrt{2M_W\Gamma_W}}\, A^{(1)}_{D,t}(p_t, 3_b, 5_{l^+}, 6_{\nu_l}) \tag{5.36}$$

$$\mathcal{A}^{(1)}_{D,\bar{t}}(p_{\bar{t}}, 4_{\bar{b}}, 7_{l^-}, 8_{\bar{\nu}_l}) = g_s^2\, g_{\text{ew}}^2\, C_F \frac{1}{\sqrt{2M_W\Gamma_W}}\, A^{(1)}_{D,\bar{t}}(p_{\bar{t}}, 4_{\bar{b}}, 7_{l^-}, 8_{\bar{\nu}_l}) \tag{5.37}$$

can be extracted from the results of Campbell, Ellis and Tramontano in [65], in which on-shell single-top production and decay were studied.

5.5.2.1 Renormalization of Factorizable Corrections

The counter-terms required for renormalization of the NLO factorizable corrections are precisely those of the on-shell production and decay subprocesses. These are shown in Figures 5.6 and 5.7. Using the Feynman rules for the counter-terms (Figure 2.2), we find that only top-quark wavefunction and strong coupling renor-

malization are required. We note that the propagator counter-term will also be required once top quark self-energies are included - this is discussed in §5.5.3.

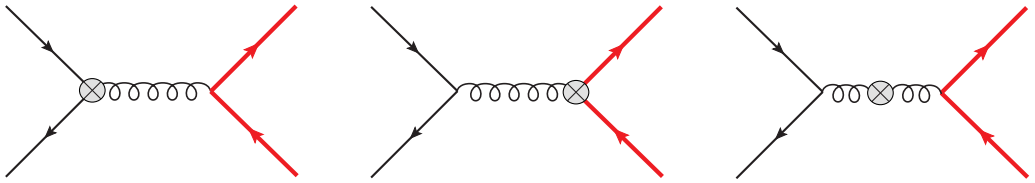

Figure 5.6: Counter-term diagrams required for renormalization of factorizable corrections to the production process: $q\bar{q} \to t\bar{t}$

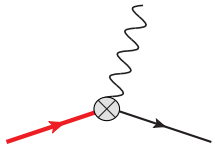

Figure 5.7: Counter-term diagrams required for renormalization of factorizable corrections to the decay process: $t \to W^+ b$

Explicitly, applying the Feynman rules[3] to the production diagrams we find

$$\begin{aligned}
\mathcal{A}_{\text{ct}}^{\text{1-loop, prod}} &= \mathcal{A}_{\text{ct, (a)}} + \mathcal{A}_{\text{ct, (b)}} + \mathcal{A}_{\text{ct, (c)}} \\
&= \left(\frac{1}{2}\delta Z_G + \frac{1}{2}\delta Z_{g_s^2}\right)\mathcal{A}^{(0)} + \left(\delta Z_t + \frac{1}{2}\delta Z_G + \frac{1}{2}\delta Z_{g_s^2}\right)\mathcal{A}^{(0)} \\
&+ \left(-\delta Z_G\right)\mathcal{A}^{(0)} \\
&= \left(\delta Z_t + \delta Z_{g_s^2}\right)\mathcal{A}^{(0)}. \qquad (5.38)
\end{aligned}$$

The decay process counter-term is

$$\mathcal{A}_{\text{ct}}^{\text{1-loop, dec}} = \frac{1}{2}\delta Z_t\,\mathcal{A}^{(0)}. \qquad (5.39)$$

[3]We recall that in the on-shell scheme, for massless quarks we have that $\delta Z_q = 0$.

In the on-shell and $\overline{MS}$ schemes respectively the wavefunction and strong coupling counter-terms are given by

$$\delta Z_t^{OS} = -g_s^2 \frac{C_F}{2} \left(\frac{3}{\epsilon} + 3 \log \left(\frac{\mu^2}{M_t^2} \right) + 4 + \eta_{sc} \right) \tag{5.40}$$

$$\delta Z_{g_s^2}^{\overline{MS}} = -g_s^2 \frac{1}{2} \left\{ \frac{1}{\epsilon} \left(\frac{11}{3} N_c - \frac{2}{3} N_f - \frac{2}{3} \left(\frac{\mu^2}{M_t^2} \right)^{\epsilon} N_h \right) - \frac{N_c}{3} \eta_{sc} \right\}. \tag{5.41}$$

Here N_c is the number of colours ($N_c = 3$) and N_f and N_h the number of light and heavy quarks ($N_f = 5$, $N_h = 1$).

5.5.2.2 Pole Structure of Virtual Factorizable Corrections

The virtual matrix elements describing the factorizable corrections to the production and decay subprocesses are given by

$$\mathcal{M}_P^{NLO,\,V} = C_F \, N_c^2 \, g_s^6 \, 2 \, \mathrm{Re} \left\{ \sum_{hels} \hat{A}_{P;1}^{(1)} \, A^{(0)*} \right\} \tag{5.42}$$

$$\mathcal{M}_{D,t}^{NLO,\,V} = C_F \, \frac{N_c^2 - 1}{4} \, g_s^6 \, 2 \, \mathrm{Re} \left\{ \sum_{hels} \hat{A}_{D,t}^{(1)} \, A^{(0)*} \right\} \tag{5.43}$$

$$\mathcal{M}_{D,\bar{t}}^{NLO,\,V} = C_F \, \frac{N_c^2 - 1}{4} \, g_s^6 \, 2 \, \mathrm{Re} \left\{ \sum_{hels} \hat{A}_{D,\bar{t}}^{(1)} \, A^{(0)*} \right\}. \tag{5.44}$$

The hatted amplitudes, $\hat{A}$, indicate that renormalization has been performed and top quark decay and production subprocesses have been sewn together. The explicit pole structure for the production subprocess is given by

$$\begin{aligned} \mathcal{M}_P^{NLO,\,V} = \frac{\alpha_s}{4\pi} \, 2 \Bigg\{ & -\frac{2C_F}{\epsilon^2} + \frac{1}{\epsilon} \Bigg[-5C_F + \left(\frac{2}{N_c} - N_c \right) \log \left(\frac{M_t^2 \mu^2}{s_{1t}^2} \right) \\ & - \frac{2}{N_c} \log \left(\frac{M_t^2 \mu^2}{s_{2t}^2} \right) + \frac{1}{N_c} \frac{s - 2M_t^2}{s\beta} \log \left(\frac{1-\beta}{1+\beta} \right) + \frac{1}{N_c} \log \left(\frac{\mu^2}{s} \right) \Bigg] \\ & + C_F \, \eta_{sc} \Bigg\} \, |A^{(0)}|^2 \end{aligned} \tag{5.45}$$

where $s_{ij} = (p_i + p_j)^2$, $\beta = (1 - 4M_t^2/s)^{1/2}$ and $s = s_{12}$. The pole structure for the decay subprocesses is

$$\mathcal{M}^{NLO,\,V}_{D,t\,(\bar{t})} = \frac{\alpha_s}{2\pi}\left\{-\frac{1}{\epsilon^2} - \frac{1}{\epsilon}\left(2\log\left(\frac{M_t^2 - M_W^2}{M_t^2}\right) - \frac{5}{2} - \log\left(\frac{\mu^2}{M_t^2}\right)\right)\right.$$
$$\left. + \frac{\eta_{sc}}{2}\right\}\,|A^{(0)}|^2. \tag{5.46}$$

5.5.3 Top Quark Self-Energies and Resummation

The discussion so far has not touched upon self-energy corrections to the top-quark propagators. Similarly nothing has yet been discussed regarding exactly what is 'resummed' in the propagators. The two are intricately linked and will be detailed next. At one-loop, the possible top quark propagator corrections consist of the QCD, QED and EW self-energy insertions depicted in Figure 5.8.

Performing the power-counting for diagram (a), we find that the leading hard and soft contributions of the self-energy insertion scale as

$$\mathcal{A}^{\text{self-energy}}_{(a),\text{hard}} \sim \delta^{-\frac{3}{2}} \tag{5.47}$$

$$\mathcal{A}^{\text{self-energy}}_{(a),\text{soft}} \sim 1. \tag{5.48}$$

The soft part poses no problems and can be treated in line with the rest of the soft contributions that we are required to include. These will be discussed further in the next section. However, the power-counting reveals a potential disaster for the hard contribution. This appears to be *super-leading*, that is, enhanced by a factor of $\delta^{-1/2}$ with respect to the leading-order terms. Unfortunately this appears to suggest a divergent expansion in δ, thus limiting the predictive power of such an approach. Luckily disaster can be averted by the use of a sensible mass-renormalization scheme.

To illustrate how this fits together, the top-quark self-energy will be examined in detail. In what follows, we will focus on the top propagator and forget about

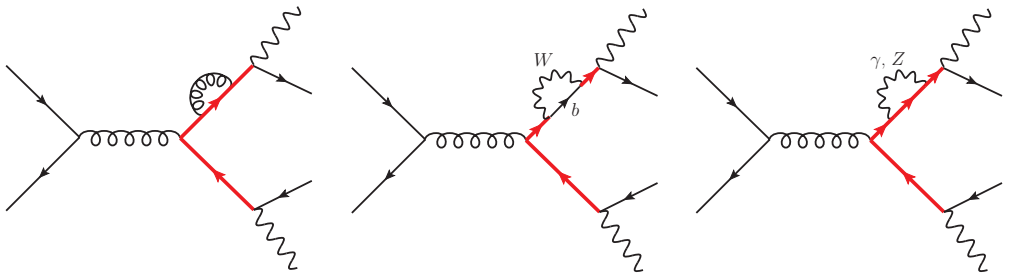

Figure 5.8: Top-Quark Self-Energy Diagrams

the rest of diagram (a). The correction to the propagator can be written as

$$\frac{i(\not{p}_t + M_t)}{D_t}\left[-4\pi\,\alpha_s\,C_F\int[dk]\frac{\gamma^\mu(\not{p}_t - \not{k} + M_t)\gamma_\mu}{k^2\,(k^2 - 2k.p_t + D_t)}\right]\frac{i(\not{p}_t + M_t)}{D_t}. \tag{5.49}$$

It is clear that just this part of the diagram scales as $\sim \delta^{-3/2}$ in the hard region. In the method of regions expansion we must keep not only the leading term, but also the first sub-leading term ($\sim \delta^{-1/2}$), as this also contributes to the set of corrections we aim to include. Performing the expansion and computing the integrals yields [62]:

$$\frac{\alpha_s C_F}{2\pi}\left(\frac{3}{2\epsilon} + 2 + \frac{\eta_{sc}}{2}\right)\left(\frac{M_t^2}{\mu^2}\right)^{-\epsilon}\left[\frac{2iM_t^2(\not{p}_t + M_t)}{D_t^2} + \frac{iM_t}{D_t} - \frac{i(\not{p}_t + M_t)}{D_t}\right] \tag{5.50}$$

where the super-leading behaviour is evident in the first term. To this the top-propagator counter-term must be added. The expression for this is given by

$$\frac{i(\not{p}_t + M_t)}{D_t} i\left((\not{p}_t - M_t)\delta Z_t - \delta M_t\right)\frac{i(\not{p}_t + M_t)}{D_t}, \tag{5.51}$$

which can then be split into terms proportional to δZ_t and δM_t. The former takes the form

$$-\frac{i(\not{p}_t + M_t)}{D_t}\delta Z_t \tag{5.52}$$

and yields a contribution to the full amplitude of $-\mathcal{A}^{(0)}\delta Z_t$. This cancels the

final term in the square brackets of (5.50), as expected, since internal lines do not require wavefunction renormalization. The term involving mass-renormalization has the form

$$\frac{\delta M_t}{M_t}\left(\frac{iM_t}{D_t}+\frac{2iM_t^2(\not{p}_t+M_t)}{D_t^2}\right). \tag{5.53}$$

We notice that the counter-term and the self-energy diagram have super-leading terms that are very similar in structure. This fact is the only potential saving grace when it comes to the super-leading terms in the expansion. Should the form of δM_t be such that there is a cancellation of the super-leading terms when (5.50) and (5.53) are added, then the super-leading terms disappear and we are left with terms which are sub-leading in δ. The latter therefore do not require resumming.

In the on-shell scheme, the mass counter-term has the form

$$\delta M_t^{OS} = -\frac{\alpha_s C_F}{2\pi} M_t \left[\frac{3}{2\epsilon}+2+\frac{\eta_{sc}}{2}\right]\left(\frac{M_t^2}{\mu^2}\right)^{-\epsilon}. \tag{5.54}$$

For this choice of mass scheme, the super-leading piece of the top-quark self-energy is cancelled exactly[4].

Expansion of diagrams (b) and (c) of Figure 5.8 results in terms scaling as

$$\mathcal{A}_{\text{hard}}^{\text{EW self-energy (W)}} \sim \delta^{-1}, \quad \mathcal{A}_{\text{hard}}^{\text{EW self-energy (Z)}} \sim \delta^{-1}, \quad \mathcal{A}_{\text{hard}}^{\text{QED self-energy}} \sim \delta^{-1} \tag{5.55}$$

$$\mathcal{A}_{\text{soft}}^{\text{EW self-energy (W)}} \to 0, \qquad \mathcal{A}_{\text{soft}}^{\text{EW self-energy (Z)}} \sim \delta^{2}, \quad \mathcal{A}_{\text{soft}}^{\text{QED self-energy}} \sim 1. \tag{5.56}$$

It is evident that the soft parts above are sub-leading and can be dropped. The hard parts of the EW-Z-boson and QED insertions are leading in δ so must be included. However, these have no imaginary part so their effect is absorbed into the definition of the top mass. Finally, the hard part of the EW-W-boson insertion is also leading. This does have an imaginary part that yields the LO definition of the top quark width and must be resummed in the top propagator.

[4]In fact, in the on-shell scheme, the QCD self-energy is cancelled completely by the propagator counter-term.

There are a couple of final comments to add here. The hard part of the two-loop QCD self-energy insertion is a leading contribution. But just as for the one-loop insertion, this is completely cancelled in the on-shell scheme. The hard part of the mixed QCD-EW two-loop insertion is sub-leading ($\sim \delta^{-\frac{1}{2}}$) and is not completely cancelled by renormalization. This must therefore be included perturbatively in a similar fashion to the factorizable corrections. In the results presented later on, the effect of this contribution is included by using the NLO top-quark width in the resummed propagator[5]. The soft parts of these two-loop insertions are beyond the accuracy we aim for. Higher loop self-energy insertions are suppressed by factors of δ due to the additional powers of the couplings involved and need not be included.

5.5.3.1 On Suitable Mass Renormalization Schemes

We have seen that the disappearance of the super-leading term in the one-loop QCD self-energy insertion is crucially dependent on the mass scheme employed. It is worth examining this closely considering that it appears that the methods presented so far would break down should a super-leading term remain.

The top mass counter-term in a generic renormalization scheme, R, can be written as

$$\delta M_t^R = \delta M_t^{OS} + \alpha_s \, \delta M_t^{R-OS}, \tag{5.57}$$

thus giving a potentially super-leading contribution of

$$\alpha_s \, \delta M_t^{R-OS} \, \frac{2iM_t^2(\not{p}_t + M_t)}{D_t^2} \; \sim \; \delta^{-\frac{3}{2}} \, \delta M_t^{R-OS}. \tag{5.58}$$

This indicates a breakdown of the expansion in δ, *unless* $\delta M_t^{R-OS} \sim \delta^{1/2}$, in which case the residual super-leading contribution is actually leading and can be resummed in the propagator. This is the case in the PS-mass scheme as discussed in detail below. In the $\overline{MS}$-scheme, however, $\delta M_t^{R-OS} \sim 1$ and so a super-leading term remains.

[5]This terms need not be resummed, however, the additional contributions included by resumming this are NNLO in δ

In principle, the use of any renormalization scheme ought to be allowed. In a generic renormalization scheme, the super-leading remainder requires the extraction of such terms from many (infinite) higher order diagrams in order that the accuracy we want is achieved. It appears that some schemes are far more practical for the *efficient* extraction of terms from the all orders perturbative expansion.

This peculiarity has its origin in the naive expectation we have had that order by order, the perturbative expansion in couplings closely resembles the structure of the full result (5.7). In particular we have implicitly assumed that the kinematic poles should be close to the physical poles, in order that the extraction of terms contributing to the full residue is feasible. Of course, this need not be the case when the perturbative expansion is arranged in a generic fashion, for example through the arbitrary choice of renormalization scheme. More precisely, the assumptions underlying the ET power-counting presented are that $p_t^2 - (M_t^R)^2 \sim \delta$ *and* $p_t^2 - \mu_t^2 \sim \delta$. As pointed out in [62], this is the case when $\mu_t^2 - (M_t^R)^2 \sim \delta$, which holds in the on-shell scheme (and also in the PS-scheme), but however in a generic scheme, for example in the $\overline{MS}$-scheme, where the renormalized mass is not related to the (region near the) pole of the full propagator, $\mu_t^2 - (M_t^{\overline{MS}})^2 \sim \delta^{\frac{1}{2}}$, thus violating these assumptions.

5.5.3.2 The PS-Mass Scheme

The PS-mass definition, introduced in Chapter 2, is an example of an alternative to the pole mass that can be used in the calculations employing the ET techniques described so far. It is given by [30]

$$M_t^{PS}(\mu_{ps}) = M_t - \alpha_s \, \Delta M(\mu_{ps}) \tag{5.59}$$

where

$$\Delta M(\mu_{ps}) = \frac{C_F \, \mu_{ps}}{\pi} \left[1 + \frac{\alpha_s}{4\pi} \left(a_1 - b_0 \left(\log \left(\frac{\mu_{ps}^2}{\mu^2} \right) - 2 \right) + \mathcal{O}(\alpha_s^2) \right) \right] \tag{5.60}$$

$$= \Delta M_1(\mu_{ps}) + \alpha_s \Delta M_2(\mu_{ps}) + \ldots \tag{5.61}$$

with M_t understood to be the pole mass of the top quark. The constants a_1 and b_1 are given by

$$a_1 = \frac{31}{3} - \frac{10N_f}{9} \qquad\qquad b_0 = 11 - \frac{2N_f}{3}. \tag{5.62}$$

Since we have that

$$M_{t,\,0} = M_t^{OS}\,\left(1 + \frac{\delta M_t^{OS}(M_t^{OS})}{M_t^{OS}} + \ldots\right) \tag{5.63}$$

$$= M_t^{PS}\,\left(1 + \frac{\delta M_t^{PS}(M_t^{PS})}{M_t^{PS}} + \ldots\right), \tag{5.64}$$

replacing M_t^{OS} with M_t^{PS} using (5.59), we find that the mass counter-term in the PS-scheme can be thus related to that in the pole-scheme via

$$\delta M_t^{PS}(\mu_{ps}) = \delta M_t^{OS}(M_t^{PS}) + \alpha_s\,\Delta M(\mu_{ps}). \tag{5.65}$$

The first term above leads to a cancellation of the first two terms of (5.50). However, in contrast to the pole-scheme where there is a complete cancellation between the top quark QCD self energy and the propagator counter-term, in the PS-scheme a residual term remains. This is given by

$$\alpha_s\,\frac{\Delta M(\mu_{ps})}{M_t^{PS}}\,\left[\frac{iM_t^{PS}}{D_t^{PS}} + \frac{2i\,(M_t^{PS})^2(\not{p}_t + M_t^{PS})}{(D_t^{PS})^2}\right]$$

$$= \alpha_s\,(\Delta M_1 + \alpha_s \Delta M_2)\,\left[\frac{i}{D_t^{PS}} + \frac{2i\,M_t^{PS}(\not{p}_t + M_t^{PS})}{(D_t^{PS})^2}\right], \tag{5.66}$$

sounding alarm bells with the presence of the term proportional to $(D_t)^2$ in the square brackets above. As mentioned in the previous subsection, should $\Delta M(\mu_{ps}) \sim \delta^{1/2}$ then the dangerous term is actually leading in δ. In detail, choosing $\mu_{ps} \sim \delta^{1/2}$ gives

$$\Delta M(\mu_{ps}) = \alpha_s\left(\sim \delta^{1/2} + \sim \alpha_s\delta^{1/2}\right), \tag{5.67}$$

and thus keeping terms scaling up to $\mathcal{O}(\delta^{-1/2})$ in (5.66), is

$$\alpha_s \, \frac{2iM_t^{PS}(\not{p}_t + M_t^{PS})}{(D_t^{PS})^2} \, (\Delta M_1 + \alpha_s \, \Delta M_2) \sim \delta^{-1} + \delta^{-1/2}. \tag{5.68}$$

The final outcome is that the first term must be resummed in the propagator whilst the second should be included perturbatively. The former leads to the following shift in the propagator:

$$p_t^2 - M_t^2 + iM_t\Gamma_t \;\rightarrow\; p_t^2 - (M_t^{PS})^2 - 2\alpha_s M_t^{PS}\Delta M_1 + iM_t^{PS}\Gamma_t := \Delta_t^{PS}, \tag{5.69}$$

whilst the latter yields the addition of the term

$$\frac{4\alpha_s^2 M_t^{PS}\Delta M_2 \left(p_t^2 - (M_t^{PS})^2 - 2\alpha_s M_t^{PS}\Delta M_1\right)}{\Delta_t^{PS}} \, \mathcal{M}^{(0)} \tag{5.70}$$

to the factorizable corrections. These must be taken into account for each resonant top quark propagator.

It is clear that the ET counting here allows for the easy identification of exactly what needs to be resummed and what must only be included perturbatively.

5.5.4 Non-Factorizable Corrections

So far only the leading *hard* part of the one-loop diagrams have been discussed in detail. As indicated by the scalings of Table 5.1, there are contributions from the expansion in soft region which must be included for consistency. The contributions that need to be kept from the set of diagrams in Figure 5.1 are given

individually by

$$\mathcal{A}^{\text{1-loop}}_{(c),\,\text{soft}} = -\frac{1}{4N_c}\left(\delta^{\bar{i}_3}_{i_1}\delta^{\bar{i}_2}_{i_4} - \delta^{\bar{i}_2}_{i_1}\delta^{\bar{i}_3}_{i_4}\right)\, I_{t\bar{t}}(p_t, p_{\bar{t}}, M_t; \epsilon, \mu)\, A^{(0)} \tag{5.71}$$

$$\mathcal{A}^{\text{1-loop}}_{(d),\,\text{soft}} = \frac{C_F}{2}\left(\delta^{\bar{i}_3}_{i_1}\delta^{\bar{i}_2}_{i_4} - \delta^{\bar{i}_2}_{i_1}\delta^{\bar{i}_3}_{i_4}\right)\, I_{tq}(p_t, p_3, M_t; \epsilon, \mu)\, A^{(0)} \tag{5.72}$$

$$\begin{aligned}\mathcal{A}^{\text{1-loop}}_{(e),\,\text{soft}} = \frac{1}{4N_c}&\left((N_c^2-2)\delta^{\bar{i}_3}_{i_1}\delta^{\bar{i}_2}_{i_4} + \frac{1}{N_c}\delta^{\bar{i}_2}_{i_1}\delta^{\bar{i}_3}_{i_4}\right)\\ &\times \left(I_{tq}(p_t, p_1, M_t; \epsilon, \mu) + I_{tq}(p_{\bar{t}}, p_2, M_t; \epsilon, \mu)\right)\, A^{(0)}\end{aligned} \tag{5.73}$$

$$\mathcal{A}^{\text{1-loop}}_{(g),\,\text{soft}} = -\frac{1}{4N_c}\left(\delta^{\bar{i}_3}_{i_1}\delta^{\bar{i}_2}_{i_4} - \delta^{\bar{i}_2}_{i_1}\delta^{\bar{i}_3}_{i_4}\right)\, I_{\bar{t}b}(p_{\bar{t}}, p_t, p_3, M_t; \epsilon, \mu)\, A^{(0)} \tag{5.74}$$

$$\mathcal{A}^{\text{1-loop}}_{(h),\,\text{soft}} = \frac{1}{4N_c}\left((N_c^2-2)\delta^{\bar{i}_3}_{i_1}\delta^{\bar{i}_2}_{i_4} + \frac{1}{N_c}\delta^{\bar{i}_2}_{i_1}\delta^{\bar{i}_3}_{i_4}\right) I_{qb}(p_t, p_1, p_3, M_t; \epsilon, \mu)\, A^{(0)} \tag{5.75}$$

$$\mathcal{A}^{\text{1-loop}}_{(i),\,\text{soft}} = -\frac{1}{4N_c}\left(\delta^{\bar{i}_3}_{i_1}\delta^{\bar{i}_2}_{i_4} - \delta^{\bar{i}_2}_{i_1}\delta^{\bar{i}_3}_{i_4}\right)\, I_{b\bar{b}}(p_t, p_{\bar{t}}, p_3, p_4, M_t; \epsilon, \mu)\, A^{(0)}. \tag{5.76}$$

It is clear that there is a common structure to the soft contributions, that of a soft scalar integral (I) accompanied by a colour factor multiplied by $A^{(0)}$, the leading double-resonant Born contribution. All necessary soft integrals are catalogued in Appendix B.

The sum of all soft corrections yields the following structure for the soft-virtual amplitude,

$$\mathcal{A}^{(1)}_{\text{soft}} = g_s^2\left(\delta^{\bar{i}_3}_{i_1}\delta^{\bar{i}_2}_{i_4}\, A^{(1)}_{\text{soft},1} + \delta^{\bar{i}_2}_{i_1}\delta^{\bar{i}_3}_{i_4}\, A^{(1)}_{\text{soft},2}\right) \tag{5.77}$$

where (suppressing the dependence of the soft integrals on M_t, ϵ and μ)

$$\begin{aligned}
A^{(1)}_{\text{soft},1} = A^{(0)} \Bigg\{ & \frac{C_F}{2} \left(I_{s.e.}(p_t) + I_{s.e.}(p_{\bar{t}}) + I_{tq}(p_t, p_3) + I_{tq}(p_{\bar{t}}, p_4) \right) \\
& + \frac{N_c^2 - 2}{4Nc} \left(I_{tq}(p_t, p_1) + I_{tq}(p_{\bar{t}}, p_2) + I_{qb}(p_t, p_1, p_3) + I_{qb}(p_{\bar{t}}, p_2, p_4) \right) \\
& + \frac{1}{4N_c} \Big(2 \left(I_{tq}(p_{\bar{t}}, p_1) + I_{tq}(p_t, p_2) + I_{qb}(p_{\bar{t}}, p_1, p_4) + I_{qb}(p_t, p_2, p_3) \right) \\
& \quad - \left(I_{t\bar{t}}(p_t, p_{\bar{t}}) + I_{t\bar{b}}(p_t, p_{\bar{t}}, p_4) + I_{t\bar{b}}(p_{\bar{t}}, p_t, p_3) + I_{b\bar{b}}(p_t, p_{\bar{t}}, p_3, p_4) \right) \Big) \Bigg\}.
\end{aligned} \tag{5.78}$$

The expression for $A^{(1)}_{\text{soft},2}$ has been omitted as due to colour this does not interfere with the tree-level amplitude.

5.5.4.1 Pole Structure of Virtual Non-Factorizable Corrections

Using (5.78) along with the expressions for the soft integrals in Appendix B, it is possible to derive the pole structure of the soft-virtual matrix element as

$$\begin{aligned}
\frac{\alpha_s}{4\pi} \frac{1}{\epsilon} 2C_F N_c \Bigg\{ & 2C_F + \frac{\eta \left(\log(-\xi_+) - \log(-\xi_-) \right)}{4N_c(\xi_+ - \xi_-)} \\
& - \frac{N_c^2 - 2}{2N_c} \left[\log\left(\frac{s_{1t} s_{3t}}{M_t^2 s_{13}} \right) + \log\left(\frac{s_{2\bar{t}} s_{4\bar{t}}}{M_t^2 s_{24}} \right) \right] \\
& - \frac{1}{2N_c} \left[\log\left(\frac{M_t^2 s_{34}}{s_{3\bar{t}} s_{4\bar{t}}} \right) + 2\log\left(\frac{s_{2t} s_{3t}}{M_t^2 s_{23}} \right) \right. \\
& \left. + 2\log\left(\frac{s_{1\bar{t}} s_{4\bar{t}}}{M_t^2 s_{14}} \right) - \log\left(-\frac{s_{3t}}{s_{3\bar{t}}} + i o_+ \right) \right] \Bigg\} |A^{(0)}|^2,
\end{aligned} \tag{5.79}$$

where $\xi_\pm = (\eta \pm \sqrt{\eta^2 - 4 + i o_+})/2$ and $\eta = (s - 2M_t^2)/M_t^2$.

5.6 Real Amplitudes

In a standard NLO calculation, though perhaps a little messy, the real corrections are by now routine to include; the Dipole and FKS subtraction methods allowing straightforward handling of the divergent regions. However, due to the expansion of the amplitudes used so far, the virtual matrix element is no longer the standard full one, but rather a modified one. In order to have singularity-matching the treatment of real corrections has to be changed a little.

In the study of resonant single top production [62, 63] there was a slight modification of the real subtraction term, where the usual NLO subtraction method

$$d\sigma^{NLO} = \left(d\sigma^{V} + \int_1 d\sigma^{R,c.t.} \right) + \int_1 (d\sigma^{R} - d\sigma^{R,c.t.}) \tag{5.80}$$

was replaced by

$$d\sigma^{NLO} \simeq \left(d\sigma^{V}_{\text{exp}} + \int_1 d\sigma^{R,c.t.}_{\text{exp}} \right) + \int_1 (d\sigma^{R} - d\sigma^{R,c.t.}) \tag{5.81}$$

to account for the fact that the virtual matrix element is now expanded to a certain order in δ. So long as the added back counter-term in the first term above is expanded to the same order in δ then the pole cancellation is exact. We note here that $d\sigma^V$ above involves the sum of the relevant hard and soft virtual corrections. There are two slightly undesirable features here. The first is that the term added back is slightly different to what is initially subtracted from the real matrix element. The difference in the terms is however of higher order in δ and thus is not of practical concern. The second feature is that the pole cancellation is achieved for the *sum* of factorizable and non-factorizable contributions. This is due to the fact that the real matrix element has not been split into factorizable and non factorizable parts. In what follows, a new treatment of the real matrix element is presented where this split is achieved. In doing so, a complete separation of factorizable and non-factorizable corrections to the process of interest is manifest.

5.6.1 Split of Real Matrix Element

It has been indicated in Section 5.3 that contributions scaling as $\delta^{-1/4}$ from the real corrections are required to compute the cross-section to the order to which we are working. Naively, this requires the real corrections to the double-resonant $t\bar{t}$ Born-level process, shown in Figure 5.9.

However, a strict expansion in δ for the case where an additional gluon is present in the final state is difficult compared to the expansion of amplitudes where only the Born-level configuration is involved. The reason for this is that it is no longer straightforward to identify precisely what the expansion parameter is. A resonant top quark momentum can now either be $(p_3 + p_5 + p_6)^2 \sim M_t^2$ or $(p_3 + p_5 + p_6 + p_9)^2 \sim M_t^2$, or indeed both of these (and similarly for the anti-top). The critical requirement of pole cancellation between real and virtual contributions, together with the structure of the virtual amplitudes unveiled by the method of regions, provide clear guidance as to how the real amplitudes must be split up. It is then possible to write the real matrix element as a sum of terms resembling the expanded virtual matrix element.

The idea is to split up the full real amplitude $\mathcal{A}^{\text{real}}_{\text{full}}$, into four parts; three proportional to $1/(D_t\, D_{\bar{t}})$, $1/(D_{t9}\, D_{\bar{t}})$ and $1/(D_t\, D_{\bar{t}9})$ respectively with the fourth one suppressed by higher powers of δ. Following the pole expansion, the numerators of these terms must be evaluated on-shell and the denominators will be replaced by $1/(\Delta_t\ \Delta_{\bar{t}})$, $1/(\Delta_{t9}\ \Delta_{\bar{t}})$ and $1/(\Delta_t\ \Delta_{\bar{t}9})$ to include effects of resummation of higher-order terms in the top quark propagators. The real amplitude can then

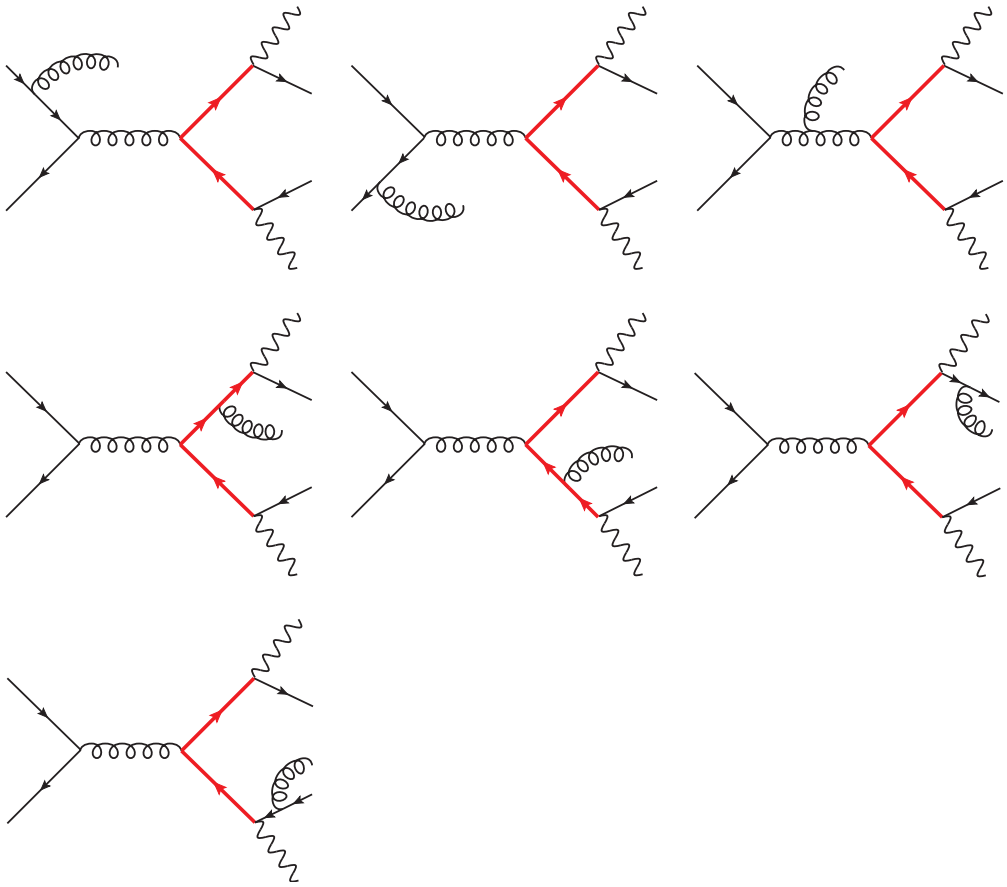

Figure 5.9: Real corrections to double resonant diagrams

be written as

$$\mathcal{A}^{\text{real}}_{\text{full}} = \sum_{\lambda=\pm}\sum_{\rho=\pm}\left\{\frac{\mathcal{A}^{R}_{D,t}(t^{\lambda}\to W^{+}\,b\,g)\;\mathcal{A}^{(0)}_{P}(q\bar{q}\to t^{-\lambda}\,\bar{t}^{\rho})\;\mathcal{A}^{(0)}_{D,\bar{t}}(\bar{t}^{-\rho}\to W^{-}\,\bar{b})}{\Delta_{t9}\Delta_{\bar{t}}}\right.$$

$$+\frac{\mathcal{A}^{(0)}_{D,t}(t^{\lambda}\to W^{+}\,b)\;\mathcal{A}^{R}_{P}(q\bar{q}\to t^{-\lambda}\,\bar{t}^{\rho}\,g)\;\mathcal{A}^{(0)}_{D,\bar{t}}(\bar{t}^{-\rho}\to W^{-}\,\bar{b})}{\Delta_{t}\Delta_{\bar{t}}}$$

$$\left.+\frac{\mathcal{A}^{(0)}_{D,t}(t^{\lambda}\to W^{+}\,b)\;\mathcal{A}^{(0)}_{P}(q\bar{q}\to t^{-\lambda}\,\bar{t}^{\rho})\;\mathcal{A}^{R}_{D,\bar{t}}(\bar{t}^{-\rho}\to W^{-}\,\bar{b}\,g)}{\Delta_{t}\Delta_{\bar{t}9}}\right\}$$

$$+\,\mathcal{A}^{R}_{\text{sub-leading}}\,, \tag{5.82}$$

where we will abbreviate the first three terms as $\mathcal{A}^R_P$, $\mathcal{A}^R_{D,t}$ and $\mathcal{A}^R_{D,\bar{t}}$ to aid the discussion that follows. $\mathcal{A}^R_P$, $\mathcal{A}^R_{D,t}$ and $\mathcal{A}^R_{D,\bar{t}}$ are the real corrections to the Born-level $t\bar{t}$-production, t-decay and $\bar{t}$-decay processes. These real corrections scale as $\delta^{-1/4}$, as required. Effects of real corrections to single- and non-resonant diagrams are captured by the term $\mathcal{A}^R_{\text{sub-leading}}$.

The expression (5.82) has been obtained by simply re-writing the full real amplitude in a way that makes the resonant structures explicit, followed by the evaluation of the latter with appropriate on-shell configurations (as required for consistency with the pole expansion used for the virtual contributions). For diagrams with a gluon emission off a (potentially resonant) top-quark line it may appear difficult to decide whether the gluon is emitted from the production or decay subprocesses. Such diagrams can be split up using the following identity

$$\begin{aligned}\frac{(\not{p}_t + M_t)\,\epsilon(\not{k})\,(\not{p}_t + \not{k} + M_t)}{(p_t^2 - M_t^2)\,((p_t+k)^2 - M_t^2)} &= \frac{(\not{p}_t + M_t)\,\epsilon(\not{k})\,(\not{p}_t + \not{k} + M_t)}{(p_t^2 - M_t^2)\,(2p_t.k)} \\ &\quad - \frac{(\not{p}_t + M_t)\,\epsilon(\not{k})\,(\not{p}_t + \not{k} + M_t)}{(2p_t.k)\,((p_t+k)^2 - M_t^2)} \end{aligned} \tag{5.83}$$

to explicitly identify the parts with the different pole structures. It is now easy to see that the first term on the RHS above would contribute to a pole-expanded real amplitude where $p_t^2 \sim M_t^2$, whilst the second term would contribute to one where $p_{t9}^2 \sim M_t^2$. This confirms that the split in (5.82) is the appropriate one picking out the correct terms from the perturbative expansion (at NLO) for use in the pole-expanded amplitudes. It is also clear that the first and second terms above will originate from amplitudes describing real corrections to production and decay sub-processes respectively.

Squaring the full amplitude then results in

$$|\mathcal{A}^{\text{real}}_{\text{full}}|^2 = |\mathcal{A}^R_P|^2 + |\mathcal{A}^R_{D,t}|^2 + |\mathcal{A}^R_{D,\bar{t}}|^2 \tag{5.84a}$$

$$+ 2\text{Re}\left(\mathcal{A}^R_P\,\mathcal{A}^{R\,*}_{D,t} + \mathcal{A}^R_P\,\mathcal{A}^{R\,*}_{D,\bar{t}} + \mathcal{A}^R_{D,t}\,\mathcal{A}^{R\,*}_{D,\bar{t}}\right) + \ldots \tag{5.84b}$$

Now the squared amplitudes of (5.84a) are nothing but the factorizable real corrections to the on-shell production and decay subprocesses. These corrections

are depicted in Figures 5.10 and 5.11. The interference terms of (5.84b) must be kept at the order in δ to which we work, whilst the ellipses indicate terms that are further suppressed and may be safely dropped. It is emphasised that the individual terms above are each gauge-invariant.

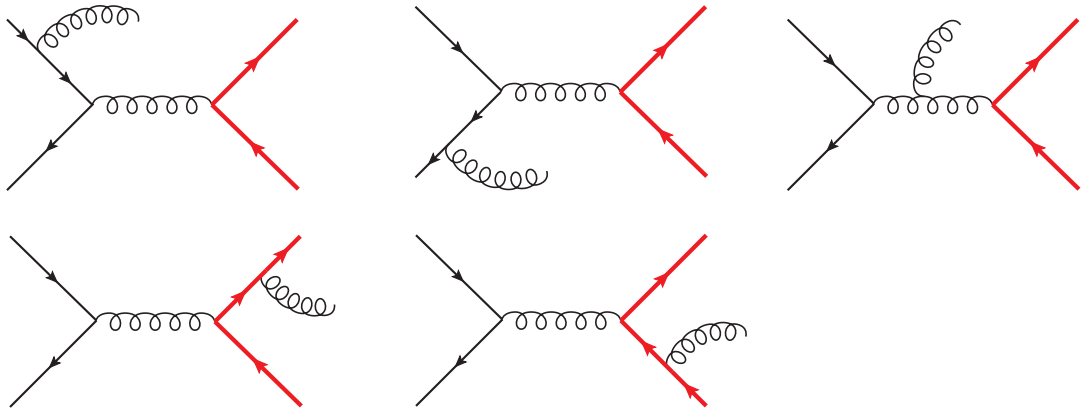

Figure 5.10: Real corrections to the on-shell production process $q\bar{q} \to t\,\bar{t}$

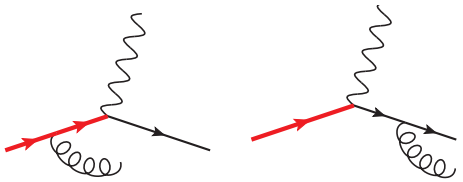

Figure 5.11: Real corrections to the on-shell decay process $t \to W^+\,b$

Given that the terms of (5.84a) are factorizable corrections, yielding ϵ-poles cancelling the corresponding poles found in the factorizable virtual corrections, the interference terms of (5.84b) correspond to the non-factorizable real corrections. Furthermore, as the ellipses indicate higher order terms in δ, the interference terms must reproduce the (soft) poles of the non-factorizable virtual matrix element. For the process being examined here the latter will be demonstrated explicitly below.

Following this split of the amplitudes, the real contributions to the NLO cross-

section is given by

$$d\sigma^{R,\,NLO} = d\sigma^R_P + d\sigma^R_{D,t} + d\sigma^R_{D,\bar{t}} + d\sigma^R_{NF} + \ldots, \tag{5.85}$$

with the first three terms in the sum indicating the factorizable contributions and $d\sigma^R_{NF}$ the non-factorizable contribution.

In accordance with the pole expansion and the approach taken thus far, all amplitudes must be computed with on-shell momentum configurations where the top quarks are on-shell. For the amplitudes above, this means $\mathcal{A}^R_P$ must be evaluated with a momentum configuration $\{p_i\}^9_1$ with $(p_3+p_5+p_6)^2 = M_t^2 = (p_4+p_7+p_8)^2$, $\mathcal{A}^R_{D,t}$ with $\{p_i\}^9_1$ where $(p_3+p_5+p_6+p_9)^2 = M_t^2 = (p_4+p_7+p_8)^2$ and $\mathcal{A}^R_{D,t}$ where $\{p_i\}^9_1$ with $(p_3+p_5+p_6)^2 = M_t^2 = (p_4+p_7+p_8+p_9)^2$. As for the terms evaluated with a Born-level momentum configuration, these on-shell momentum configurations are obtained from the corresponding off-shell ones via an expansion of the momenta in δ.

5.6.2 Structure of Real Factorizable Corrections

The terms $d\sigma^R_P$, $d\sigma^R_{D,t}$ and $d\sigma^R_{D,\bar{t}}$ can be computed straightforwardly à la standard real subtraction methods. The pole structure of these can be extracted from the insertion factors of [32, 39] and [65]. For the production subprocess the insertion factor is explicitly

$$\begin{aligned}\mathbf{I}_P(\epsilon)|A^{(0)}|^2 = \frac{\alpha_s}{2\pi}\Bigg\{ &\frac{2C_F}{\epsilon^2} + \frac{1}{\epsilon}\Bigg[5C_F - \left(\frac{2}{N_c} - N_c\right)\log\left(\frac{M_t^2\mu^2}{s_{1t}^2}\right) \\ &+\frac{2}{N_c}\log\left(\frac{M_t^2\mu^2}{s_{2t}^2}\right) - \frac{1}{N_c}\frac{s-2M_t^2}{s\beta}\log\left(\frac{1-\beta}{1+\beta}\right) + \frac{1}{N_c}\log\left(\frac{\mu^2}{s}\right)\Bigg] \\ &+C_F\,\eta_{sc}\Bigg\}\;|A^{(0)}|^2\end{aligned} \tag{5.86}$$

and for the decay subprocesses we have

$$\mathbf{I}_{D,t\,(\bar{t})}(\epsilon)|A^{(0)}|^2 = \left\{ \frac{1}{\epsilon^2} + \frac{1}{\epsilon}\left(2\log\left(\frac{M_t^2 - M_W^2}{M_t^2}\right) - \frac{5}{2} - \log\left(\frac{\mu^2}{M_t^2}\right)\right) - \frac{\eta_{sc}}{2}\right\} |A^{(0)}|^2. \tag{5.87}$$

As expected, comparing with (5.45) and (5.46), we have analytical cancellation of ϵ-poles between factorizable real and virtual contributions. Note also, that in all three sets of factorizable contributions the dependence on the regularization scheme disappears in the sum of virtual and real, as it should.

We note in passing that in contrast to the full real amplitude, where there is no soft singularity when a gluon is emitted from an intermediate top quark (as the top is off-shell), the 'expanded' real amplitude does exhibit soft singularities in such diagrams. This is understood physically as the modified real amplitudes are evaluated with on-shell momentum configurations. Thus essentially the top-quark (as far as IR-behaviour is concerned) is a final state, on-shell particle. The presence of additional singularities is to be fully expected from a method that treats real corrections in line with the method of regions used for the virtual corrections where, as mentioned previously, the expansion in regions introduces additional singularities to the individual (hard and soft) expansions.

5.6.3 Structure of Real Non-Factorizable Corrections

The non-factorizable real corrections only contain soft singularities. There are no collinear singularities due to the fact that $\mathcal{A}_P^R$, $\mathcal{A}_{D,t}^R$ and $\mathcal{A}_{D,\bar{t}}^R$ have different collinear divergent regions. Thus the interference terms, although appearing to contain collinear divergences, are actually integrable in these regions. On the other hand, all amplitudes have soft singularities $\sim 1/p_{9,0}$ and thus the interference term contains a non-integrable $1/p_{9,0}^2$ singularity, manifesting itself as a $1/\epsilon$ pole.

The requirement that the three amplitudes $\mathcal{A}_P^R$, $\mathcal{A}_{D,t}^R$ and $\mathcal{A}_{D,\bar{t}}^R$ be evaluated with different on-shell momentum configurations leads to difficulties in constructing a real counter-term for the non-factorizable matrix real matrix element. In the

Dipole method, the subtraction counter-term smoothly interpolates between the strict soft (and collinear) limits and regions away from these, and are functions of a single momentum configuration. The fact that soft and collinear regions are treated simultaneously in this way makes it difficult to use the Dipole method without significant modification to construct a local counter-term. However, as the FKS method treats soft and collinear regions separately, together with the fact the counter-term is a function of the real momentum configuration in the strict limits (where the three different momentum configurations we must use are the same), it is more straightforward to construct a local counter-term.

From the FKS soft counter-term we can extract the pole structure of the non-factorizable matrix element:

$$\begin{aligned}
&\frac{\alpha_s}{2\pi}\,\frac{C_F N_c}{2}\,\frac{1}{\epsilon}\,\{-4C_F \\
&+\left(\frac{1}{N_c}-\frac{N_c}{2}\right)\left[\log\left(\frac{M_t^2}{s_{1t}}\right)+\log\left(\frac{M_t^2}{s_{2\bar{t}}}\right)+\log\left(\frac{\mu^2}{s_{1t}}\right)+\log\left(\frac{\mu^2}{s_{2\bar{t}}}\right)\right] \\
&-\frac{1}{N_c}\left[\log\left(\frac{M_t^2}{s_{1\bar{t}}}\right)+\log\left(\frac{M_t^2}{s_{2t}}\right)+\log\left(\frac{\mu^2}{s_{1\bar{t}}}\right)+\log\left(\frac{\mu^2}{s_{2t}}\right)\right] \\
&-2C_F\left[\log\left(\frac{M_t^2}{s_{3t}}\right)+\log\left(\frac{M_t^2}{s_{4\bar{t}}}\right)+\log\left(\frac{\mu^2}{M_t^2}\right)\right] \\
&+\frac{2}{N_c}\left[\log\left(\frac{\mu^2}{s_{14}}\right)+\log\left(\frac{\mu^2}{s_{23}}\right)-\log\left(\frac{\mu^2}{s_{13}}\right)-\log\left(\frac{\mu^2}{s_{24}}\right)-\frac{1}{2}\log\left(\frac{\mu^2}{s_{34}}\right)\right] \\
&+N_c\left[\log\left(\frac{\mu^2}{s_{13}}\right)+\log\left(\frac{\mu^2}{s_{24}}\right)\right]-\frac{1}{2N_c}\frac{1}{V_{t\bar{t}}}\log\left(\frac{1+V_{t\bar{t}}}{1-V_{t\bar{t}}}\right)\Bigg\}\left|A^{(0)}\right|^2. \qquad (5.88)
\end{aligned}$$

Here $V_{t\bar{t}}=\left(1-(2M_t^2/s_{t\bar{t}})^2\right)^{1/2}$ and $s_{ij}=2p_i.p_j$.

After a little manipulation of the non-factorizable virtual pole structure, (5.79) and making the replacement $\eta=2\left(1-V_{t\bar{t}}^2\right)^{-1/2}$, it is relatively straightforward to see that the above non-factorizable real poles do indeed cancel those of the soft-virtual matrix element. This however does take place via a delicate cancellation of terms from different logarithms.

This completes the discussion regarding the methods to consistently extract factorizable and non-factorizable corrections from both loop and single-emission

contributions in perturbation theory. We emphasise that this means that, at the order in δ to which we work, the fully differential NLO cross-section can now be written as

$$d\sigma^{NLO} = d\sigma^{P} + d\sigma^{D,\,t} + d\sigma^{D,\,\bar{t}} + d\sigma^{\mathrm{NF}}, \tag{5.89}$$

where 'P', 'D, $t(\bar{t}\,)$' label the production and (anti-) top-decay factorizable corrections and 'NF' labels the non-factorizable corrections.

Finally, it is pointed out that the matrix elements making up each part of the differential cross-section must be evaluated using projected momenta. Resonant top propagators must however be kept off-shell. Schematically, for each NLO contribution $J(m) = V,\ C,\ R$ (with m final state particles) to $d\sigma^{I}$ ($I = P,\ (D,t),\ (D,\bar{t}),$ NF) of (5.89) , we must ensure that

$$d\sigma^{J(m),\,I} \sim \int d\Phi(\{p_i^{\mathrm{off}}\}_1^m)\, \frac{\mathcal{M}^{J(m),\,I}(\{\hat{p}_i^{\,\mathrm{on}}\}_1^m)}{\Delta_t^{\mathrm{off}}\,\Delta_{\bar{t}}^{\mathrm{off}}}\, \mathcal{F}^m(\{p_i^{\mathrm{off}}\}_1^m). \tag{5.90}$$

The denominators of the resonant propagators have been pulled out to highlight that they are to be evaluated with the off-shell configurations. Details of the projections used are given in Appendix A.

5.7 Remarks on Effective Theory Structure

It is clear that the use of the method of regions in conjunction with the pole expansion for the virtual contributions, together with the consistent method developed to subsequently treat the real corrections, points towards a definite structure to the matrix elements in the resonant regions. Taking the arguments of §4.4 into account, this structure is to be fully expected.

The physical scales present imply that there is a kind of factorization of top quark production, propagation and decay subprocesses where the only connections between these can be provided by soft gluons. The ET picture of the scenario for top-pair production is shown in Figure 5.12.

In a formal ET approach, the high virtuality modes would be integrated out of the full theory leaving a theory comprised of operators describing the production,

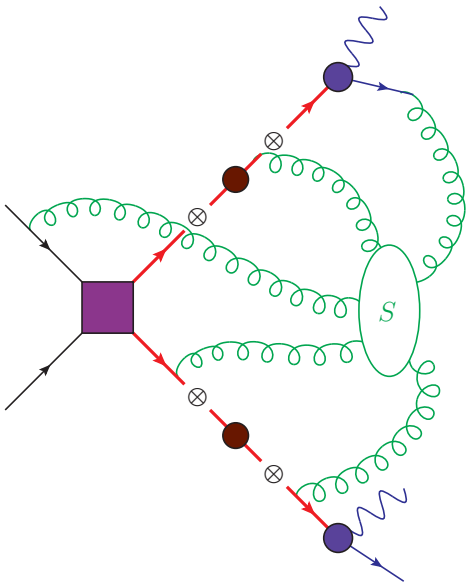

Figure 5.12: Effective Theory picture of Resonant $t\bar{t}$ production. Operators describing the production, propagation and decay of heavy quarks are only connected via soft gluons.

propagation and decay of heavy top quarks, indicated schematically by the violet box and brown and purple discs respectively in Figure 5.12. These would all be accompanied by Wilson (or matching) coefficients which describe the effects of the high virtualities (hard gluons for the case at hand) and are strictly gauge-invariant. The factorizable contributions arising from the expansion in δ capture precisely these parts of an ET approach, hence they are expected to be gauge-invariant. Furthermore, matching coefficients are always evaluated *on-shell*, a property reflected in the factorizable corrections, which as previously discussed are essentially corrections to on-shell top-quark production and decay.

Once the high virtuality modes have been integrated out, there are some dynamical modes (of low energy or virtuality) still left in the theory. In general there will be multiple dynamical modes remaining. However, for the processes at hand, the only dynamical modes are those describing soft gluons. These are the only fields in the ET that can possibly connect the production and decay operators. In Figure 5.12 the dynamical modes are depicted by the green circle and associated connections of this to the ET operators via the green gluon lines.

The effects of hard gluons connecting production and decay would be contained in higher dimensional operators (e.g. operators describing production of an on-shell top in association with a W^--boson and a b-quark), but these are suppressed by powers of the high matching scale. This provides an ET explanation to why the hard contributions of the 'non-factorizable' diagrams are sub-leading in δ.

In ETs, there is an honest factorization of hard and soft modes. The methods outlined in the previous sections allow for the extraction of the dominant contributions (i.e. those that lead to the picture in Figure 5.12) from the standard perturbative expansion and, moreover, for their complete separation into the hard and soft modes of an ET. In other words, it is now possible to treat these different sets of corrections as separate entities living as one might expect, at different scales; soft, $\mu_s \sim \Gamma_t$ and hard $\mu_h \sim M_t$.

Of course, simply evaluating the soft and hard corrections at different scales is not consistent. Importantly, this may well lead to a spoiling of what the method of regions so elegantly provides us with: the important part of the full result given via a sum of simpler terms. A naive evaluation with different scales would almost certainly ruin the pole structure, let alone the finite terms of the sum of these simpler integrals. The appropriate way to do this would be to run the hard corrections from μ_h to μ_s using the renormalization group equations, and evaluate the amplitudes at the common scale there, thus maintaining the correct pole structure of the full result. Furthermore, this procedure would have the added benefit of providing a resummation of large logarithms of the form $\sim \log(\mu_h/\mu_s)$. It should be pointed out that despite an important step being made towards this in the work presented here, the framework for the resummation of the large logs mentioned is not yet in place. One of the difficulties is that we are dealing with exclusive quantities with arbitrary cuts on final states which somewhat complicates the running between the hard and soft scales.

Finally, it has been pointed out that the methods described above are only strictly valid above threshold. The reason for this is that a new scale enters the problem and thus a new region must be taken into account in the method of regions[6]. Near threshold, the ET thus changes to one that realises a consistent

[6]More precisely, in this region the top momentum can be parametrized as $p_t^\mu = M_t\, v^\mu + q^\mu$ with $v = (1, \vec{0})$ and $q_0 \sim \delta$, $\vec{q} \sim \delta^{1/2}$. This new region, known as the Potential or Coulomb

expansion in this new region.

5.8 Remarks on Potential Limitations

Despite the power of the methods presented here in simplifying the calculation of processes involving unstable particles as well as picking out important structures in the full expansion of perturbation theory, there are a few limitations. The latter are mainly manifest in the kinematic cuts that must be applied to the final states. The predictions made using the methods developed here would by no means be valid in all kinematic regimes of a $W^+ b W^- \bar{b}$ final state.

As underlined, the ET expansion is only really valid in the regions where the top quarks are resonant and where the top anti-top system is above threshold. From an experimental point of view, perhaps the former condition is not as important if the objects of interest are the top quarks. These must be tagged in some way, which often involves imposing invariant mass cuts on the top quark decay products in a very similar vein to the assumptions the calculations in this chapter have been built upon. The threshold condition is only expected to have a small numerical effect to inclusive quantities at LHC energies. Some distribution bins may change a little, in particular those sensitive to the invariant mass of the $t\bar{t}$ system near threshold.

It is clear that threshold effects would be very important at an e^+e^- Linear Collider for a threshold scan about the top mass. In this case, it might be possible to match the calculations presented here with one that captures the important physics near threshold, using for example, NRQCD, or another appropriate ET. A significant challenge is the extraction of the appropriate real corrections consistent with the new expansion of the amplitudes - a necessary requirement for the study of exclusive observables.

region must systematically be taken into account.

Chapter 6

Results

In this chapter we explore in detail the numerical results of the implementation of the method detailed in Chapter 5. The focus will be mainly on results relevant for the Tevatron, because it is for the latter that the $q\bar{q}$ initiated process dominates top-pair production. We will endeavour to carefully compare the differences between on-shell and off-shell approaches as well as highlighting observables that are sensitive to off-shell effects. The particularly topical 'Forward-Backward asymmetry' as well as the effects of using a different mass-scheme suitable for use with the ET method will also be discussed.

6.1 Setup of Differential Computations

The matrix elements described in detail in the previous section have been assembled into an ensemble of Fortran code to produce fully differential results for a variety of observables. The phase-space generation in this work has made use of the 'Vegas' adaptive Monte Carlo algorithm from the 'Cuba' library for multi-dimensional numerical integration [66].

In order that contact is made with measurements in real experiments the final state partons, the b-quarks (and gluon at NLO), are clustered into jets. The algorithm employed is the sequential recombination k_t-algorithm [67, 68], although in principle any IR-safe jet algorithm can be used. The PDF set used is the (LO and NLO) MSTW2008 set [36], which also provides the numerical values

for $\alpha_s(\mu)$.

6.1.1 Observable Definition

In order to experimentally identify $t\bar{t}$ events certain conditions are usually imposed on the final states observed. The basic requirements we have are that a b-jet, J_b, and $\bar{b}$-jet, $J_{\bar{b}}$, are found by the jet-algorithm, in addition to a W^+ and a W^- being perfectly reconstructed (i.e. the four-momenta of the W's are $p(W^+) = p(l^+) + p(\nu_l)$ and $p(W^-) = p(l^-) + p(\bar{\nu}_l)$). Whilst the latter is not possible at experiments, where only the total missing momentum of the two neutrinos can be measured, it will allow us to cleanly identify features likely to be present in an experimentally more rigorous analysis. We define the 'top' momentum as $p(t) = p(J_b) + p(W^+)$ and the 'anti-top' momentum as $p(\bar{t}) = p(J_{\bar{b}}) + p(W^-)$, where the quotation marks '' highlight the fact that in a realistic setup it is not possible to unambiguously determine the top or anti-top momenta, even if these are correctly identified. This is of course due to (numerous sources of) additional radiation in experimental events that can leak into or out of the construction of jets, hence affecting momentum measurements. On the theory side, this arises naturally at NLO through the presence of the additional emitted parton from the real corrections.

The methods used to compute the scattering amplitudes for off-shell top quarks have relied on the condition that the tops are near resonance. In addition, we have advocated that we must stay above the $t\bar{t}$ threshold for our results to be trusted. These two important conditions are reflected in the following invariant-mass constraints on the final states that will always be made,

$$\begin{aligned} 140 \text{ GeV} < M_{\text{inv}}(t) &= \sqrt{\left(p(J_b) + p(W^+)\right)^2} < 200 \text{ GeV} \\ 140 \text{ GeV} < M_{\text{inv}}(\bar{t}\,) &= \sqrt{\left(p(J_{\bar{b}}) + p(W^-)\right)^2} < 200 \text{ GeV} \\ M_{\text{inv}}(t\bar{t}\,) &= \sqrt{\left(p(t) + p(\bar{t}\,)\right)^2} > 350 \text{ GeV}. \end{aligned} \tag{6.1}$$

In addition to these cuts that should always be made in the off-shell case, the

Collider: Tevatron, $\sqrt{s} = 1.96$ TeV		
$p_T(J_b) > 15$ GeV	$p_T(l^+) > 15$ GeV	$\not{E}_T > 20$ GeV
$p_T(J_{\bar{b}}) > 15$ GeV	$p_T(l^-) > 15$ GeV	$R_{\rm jet} = 0.7$
$M_t = 172.9$ GeV	$\Gamma_t^{\rm NLO} = 1.3662$ GeV	$M_Z = 91.2$ GeV
$M_W = 80.4$ GeV	$\Gamma_W = 2.14$ GeV	$\alpha_{\rm ew} = 0.03394$

Table 6.1: Example process definition at the Tevatron Collider, $\sqrt{s} = 1.96$ TeV and parameter setup.

setup of Table 6.1 is considered[1] as an example application of the code. Values of the parameters used are also indicated there.

The process these cuts define is

$$p\,\bar{p} \;\to\; J_b\,J_{\bar{b}}\,\not{E}_T\,l^+\,l^- + X, \tag{6.2}$$

typical of an experimental setup for studying top-pair production. Of course, in addition to the $q\bar{q}$-initiated process, the gg-initiated (and at NLO the qg and $\bar{q}g$-initiated) process must be included. However, as the $q\bar{q}$-initiated process is by far the dominant one at the Tevatron, we focus on this here.

6.2 Checks and Validation

The code written that provides the sample results presented here has been put through numerous validation checks. Some of these will be outlined here as will a comparison to the literature in the case where we consider on-shell top-pair production.

The computation of the NLO piece from the real corrections was implemented using two independent codes with two different subtraction methods, the Dipole method and the FKS method. For all observables tested, both methods give the same numerical results (within Monte Carlo integration uncertainties), thus

[1] It is precisely the set of experimental cuts combined with the jet definition that form the measurement function introduced earlier.

	$\sigma^{\text{incl.}}_{LO}$ $[fb]$			$\sigma^{\text{incl.}}_{NLO}$ $[fb]$		
	MCFM	TOPIXS	US	MCFM	TOPIXS	US
$p\bar{p}$ 1.96 TeV	66.46(2)	66.449(1)	66.449(4)	79.62(8)	79.71(1)	79.71(2)
pp 7 TeV	335.11(8)	335.037(1)	335.04(3)	383.4(4)	383.94(5)	383.89(5)
pp 14 TeV	1039.6(2)	1039.43(1)	1039.4(1)	1167.5(5)	1168.0(1)	1167.9(3)

Table 6.2: Comparisons of $\sigma^{\text{inclusive}}$ for on-shell $t\bar{t}$-production (in the di-lepton channel) with the publicly available codes TOPIXS [69] and MCFM [49]. Decays of the top quarks are included here at LO. Scales have been set to $\mu_F = \mu_R = M_t$.

providing a strong check on these contributions to the differential cross-sections.

Comparisons of the total inclusive cross-section (i.e. not implementing the cuts in Table 6.1) for on-shell $t\bar{t}$-production, at different centre of mass energies and scales, have been made with the publicly available programs TOPIXS [69] and MCFM [49], where full agreement has been found. More precisely, these comparisons include the corrections to the production subprocess but not to the top or anti-top decay subprocesses. A selection of these comparisons is shown in Table 6.2.

In addition to this, corrections to the production at the differential level have been cross-checked against a number of distributions produced by MCFM. For the observables checked, very good agreement was found and for illustration, a couple of distributions are shown in Figure 6.1. These not only provided an additional check on the factorizable corrections to the production subprocess, but also checked our implementation of spin correlations.

Due to the modular nature of the scattering amplitudes, it has been straightforward to check each set of corrections individually. The factorizable corrections to the top and anti-top decay vertices have been compared with the earlier work involving resonant single-top production [62, 63], where complete agreement was found. For the non-factorizable corrections, there were no 'easy' checks to be made with any literature, however, exact pole cancellation between real and virtual terms provides us with confidence that these have been correctly computed. Furthermore, the analytic expressions for the soft integrals have been compared to numerical integrations with very good agreement. The non-factorizable real

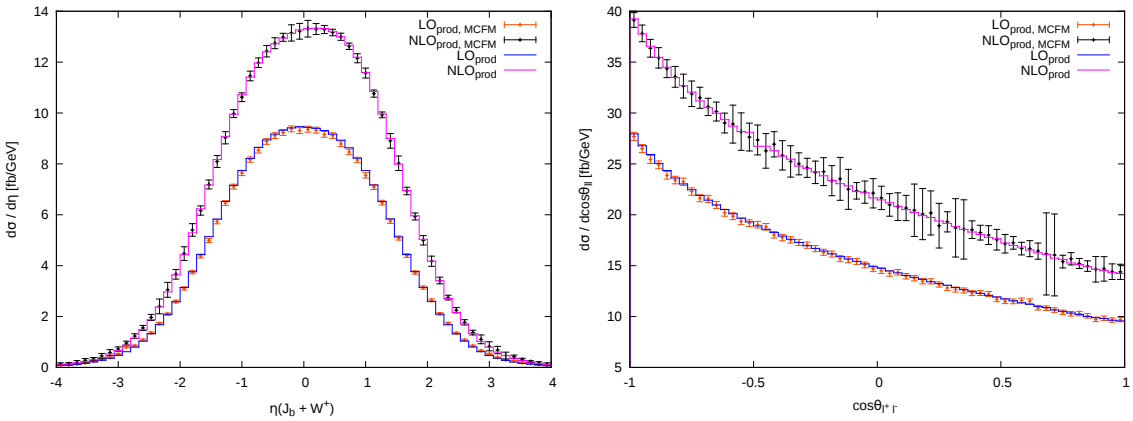

Figure 6.1: Sample distribution comparisons with MCFM, $\eta(J_b + W^+)$ (left) and $\cos(\theta_{l^+l^-})$ (right). LO and NLO results are compared for $\mu_F = \mu_R = 2M_t$.

corrections, computed using the FKS method, display the required independence on the $\xi_{\rm cut}$ parameter, providing an additional strong check.

6.3 1.96 TeV Tevatron Observables

In this section we present a detailed analysis of the numerical results for the setup of Table 6.1. In particular, the importance (or not) of off-shell effects is discussed at length. The following definitions are introduced to aid the illustration of the various effects:

$$d\sigma^{\text{NLO-correction}} = d\sigma^{\text{NLO, off-shell}} - d\sigma^{\text{LO, off-shell}} \tag{6.3}$$

$$d\sigma^{\text{off-shell effects}} = d\sigma^{\text{NLO, off-shell}} - d\sigma^{\text{NLO, on-shell}}. \tag{6.4}$$

In addition to these two types of correction to the cross-section, we have also implemented and examined the effects of the leading order *single*-resonant contributions which are suppressed by factor of δ relative to the LO double-resonant contributions (i.e. 'NN'LO in the power-counting, see (5.13) and (5.14)).

6.3.1 Cross-Sections

We first examine the inclusive cross-section for the setup described. The scale dependence of the LO and NLO, on-shell (dashed) and off-shell (solid) cross-sections under varying $\mu = \mu_F = \mu_R$ is shown in Figure 6.2. As expected, within a reasonable range of scales, the NLO cross-sections display a reduced scale-dependence compared with the LO cross-sections. We also note that the shape of the inclusive LO cross-section under scale variation remains the same when LO PDFs are used (indicated by the solid grey line in Figure 6.2), the difference appearing only as a slight shift of the curve.

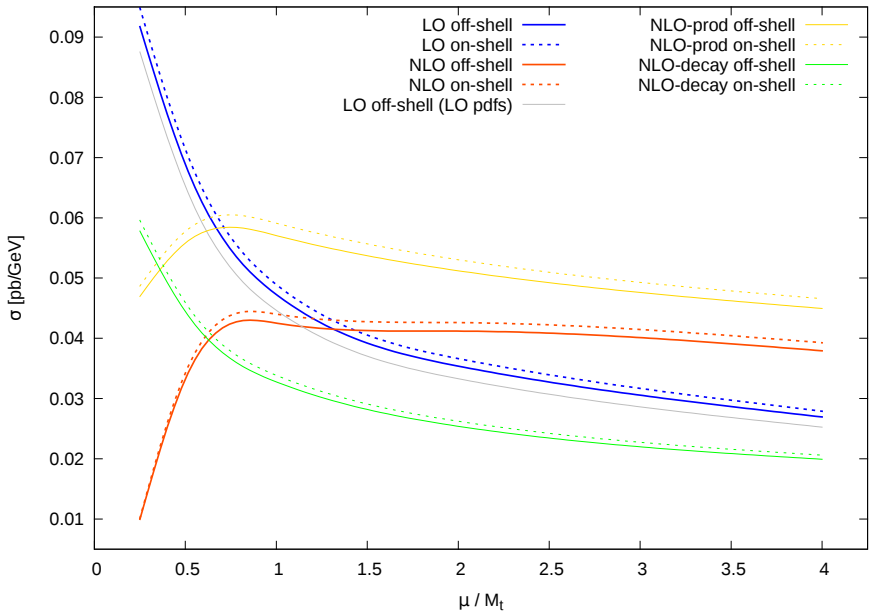

Figure 6.2: Scale variation of the LO and NLO cross-sections for $p\,\bar{p} \to J_b\,J_{\bar{b}}\,\not{E}_T\,l^+\,l^- + X$. The solid lines correspond to the off-shell results, whilst the dashed lines correspond to the on-shell case.

A more direct comparison of on-shell versus off-shell inclusive numbers can be found in Table 6.3 in which each correction making up the total NLO result is also contrasted. The differences between on-shell and off-shell numbers are around 2-4%, which is a little larger than what is to be expected by the cancellation theorems of [50, 51] ($\Gamma_t/M_t \sim 1\%$). This is likely to be related to a slight spoiling

of the cancellation of large logarithms brought about by the cuts imposed on our final state. The pure non-factorizable corrections make up a very small 0.5% correction to the NLO off-shell cross-section. The reason for this tiny number is illustrated later through the explicit visualisation of the large cancellations that occur there.

	on-shell	off-shell	% difference
σ^{LO} [fb]	49.368(4)	47.680(5)	-3.4 %
σ^{NLO} [fb]	43.137(5)	42.00(2)	-2.6 %
$\sigma^{\text{NLO-prod-correction}}$ [fb]	9.118(3)	8.782(3)	-3.7%
$\sigma^{\text{NLO-}t\text{dec-correction}}$ [fb]	-7.673(1)	-7.373(1)	-3.9%
$\sigma^{\text{NLO-}\bar{t}\text{dec-correction}}$ [fb]	-7.675(1)	-7.373(1)	-3.9%
$\sigma^{\text{NLO-NF-correction}}$ [fb]	N/A	0.29(2)	N/A
σ^{SR} [fb]	N/A	0.6984(3)	N/A

Table 6.3: Breakdown of the NLO on-shell and off-shell cross-sections for $\mu_F = \mu_R = M_t$. The contributions of factorizable and non-factorizable corrections are detailed. The last column indicates the % change in going from on-shell to off-shell. Numbers in brackets are Monte Carlo uncertainties.

It is interesting to observe that the corrections to the production subprocess are positive whilst the decay corrections are negative and thus leaving out either set leads to significantly different numbers for the full NLO cross-section. This is also indicated in Figure 6.2, where the gold and green lines trace the NLO cross-sections where corrections to only production and only decay are respectively included.

Table 6.3 also indicates the size of the single-resonant contributions, σ^{SR}, that are suppressed by a factor of δ relative to the LO numbers. More precisely, the single-resonant piece contains both $2\text{Re}[A_{-2}^{(1,1)}A_{-1}^{(1,1)*}]$ and $|A_{-1}^{(1,1)}|^2$ of (5.14), although the latter term is formally even further suppressed[2]. These terms constitute a correction of 1.5% to the LO cross-section, agreeing well with the estimate

[2]To be strict in the power-counting we should also include the double-resonant EW term $\sim |A_{-2}^{(0,2)}|$ along with the single-resonant pieces.

of their size from a power-counting point of view (corrections of $\delta^{1/2}$ and δ roughly correspond to 10% and 1% corrections).

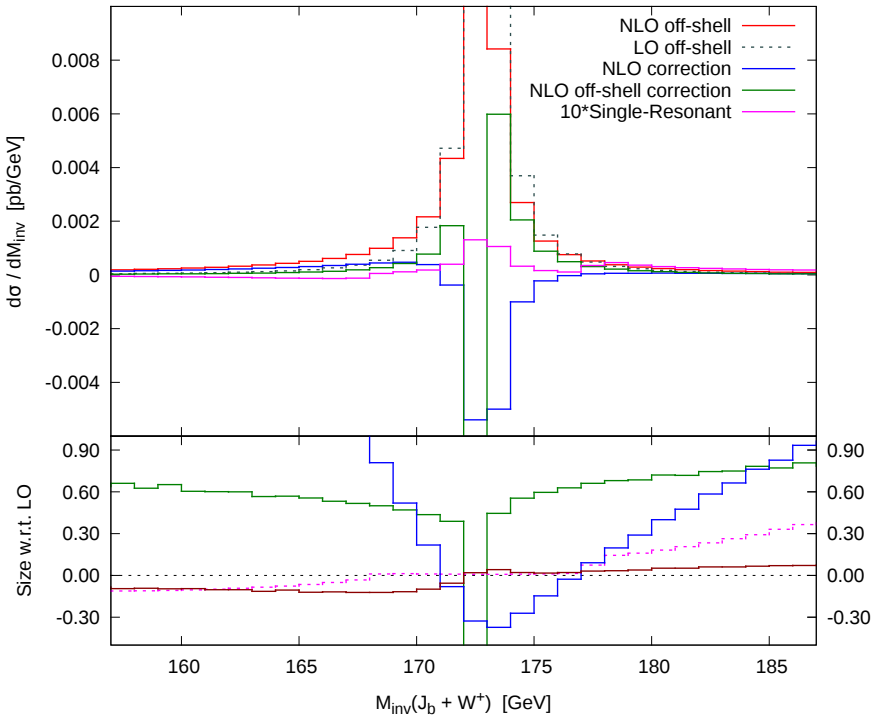

Figure 6.3: The various contributions to the invariant-mass of the top quark are shown in the upper panel. The lower panel shows the size of the NLO corrections (blue), off-shell effects (dark green), non-factorizable corrections (dark red) and single-resonant contributions (dashed purple) with respect to LO.

The effects on the inclusive cross-sections of including the off-shellness of top quarks are, as expected, rather small. However, the modest size of these corrections appears to be strange if one examines a differential observable such as the invariant mass of the top. Figure 6.3 depicts the LO and NLO distributions as well as the NLO off-shell corrections and the single-resonant contributions. The lower panel indicates the size of the latter three, relative to the LO predictions. What is perhaps surprising is that the off-shell corrections, as defined by (6.4) are large over the whole range of $M_{\text{inv}(t)}$ shown. The key reason behind the small impact the top off-shellness has on the inclusive cross-section is the fact that the

off-shell effects change sign from positive to negative around $M_{\rm inv}(t) \simeq M_t$, that is at the peak of this distribution. This cancels out the large positive effects arising from the tails of the distribution when integrating over the range of $M_{\rm inv(}t{\rm)}$. This will be a common feature in other distributions sensitive to the off-shellness of the top quarks.

Figure 6.3 also highlights that in the region of $M_{\rm inv}(t) \simeq M_t$, the NLO corrections and off-shell effects dominate, indicating that the ET method is working well here. We notice that the single-resonant pieces do begin to gain some significance moving towards the tails of the distributions. However, these are still smaller than the full NLO corrections and off-shell effects. Note that the increasing influence of the single-resonant pieces as we move further out of the resonant region is a tell-tale sign that the ET method employed here is one based on an expansion in a small 'kinematic' parameter. The cuts on $M_{\rm inv}(t)$ allow this kinematic parameter, Δ_t/M_t^2 to lie in the range [0.005, 0.35]. Towards the upper extreme of this range it is clear that the scaling is no longer $\Delta_t/M_t^2 \sim \alpha_s^2 \sim \delta$, but rather $\Delta_t/M_t^2 \sim \delta^{1/2}$, indicating that the counting slowly misjudges the size of the various contributions (for example, the single resonant contributions grow to scale as the NLO corrections, no more contributing as 'NN'LO). However, as the cross-section is very small in this region, the increasing importance of the sub-leading terms is not of great concern.

6.3.2 'Standard' Distributions

In this subsection we look at some common distributions displayed in Figures 6.4 and 6.5. The green and red bands are the LO and NLO off-shell predictions obtained by varying $\mu_F = \mu_R = \mu$ in the range $[M_t/2,\, 2\,M_t]$. The solid green and red lines indicate the LO and NLO off-shell distributions at the central scale $\mu = M_t$, whilst the NLO on-shell and sub-leading contributions (multiplied by a factor of 10 to make them visible) at the same scale are given by the blue and purple lines respectively. The ratio of off-shell effects versus the NLO off-shell results (red) and sub-leading terms over the LO weights (blue) are plotted in the lower panels. The first ratio allows for a clear identification of the regions in which off-shell effects are important whilst the second gives us a measure of how

well the ET power-counting estimates the suppressed terms.

It is important to stress that wherever we study an observable of the top or anti-top, it is implicitly assumed that we are referring to the *reconstructed* top or anti-top, i.e. defined via the b-jets and W-bosons, and never that the actual top or anti-top are somehow artificially isolated.

Figure 6.4 includes kinematic distributions for (left to right, top to bottom) the rapidity of the top, $\eta(t)$, the invariant mass of the top-anti-top system, $M_{\rm inv}(t,\bar{t})$, the rapidity of the positively charged lepton, $\eta(l^+)$, the cosine of the opening angle between the two charged leptons (in the lab frame), $\cos\theta_{l^+l^-}$, the transverse momentum of the top-anti-top system, $p_T(t\bar{t})$ and the hadronic transverse momentum, $H_T(J_b,\ J_{\bar{b}})$. These are defined via:

$$\begin{aligned}
\eta(t) &= \frac{1}{2}\,\log\left(\frac{|\vec{p}(t)|+p_z(t)}{|\vec{p}(t)|-p_z(t)}\right)\\
M_{\rm inv}(t,\bar{t}) &= \left[\left(p(J_b)+p(l^+)+p(J_{\bar{b}})+p(l^-)+p_{\rm miss}\right)^2\right]^{1/2}\\
\eta(l^+)\equiv y(l^+) &= \frac{1}{2}\,\log\left(\frac{p_0(l^+)+p_z(l^+)}{p_0(l^+)-p_z(l^+)}\right)\\
\cos\theta_{l^+l^-} &= \frac{\vec{p}(l^-)\cdot\vec{p}(l^+)}{p_0(l^+)p_0(l^-)}\\
p_T(t\bar{t}) &= p_T(t)+p_T(\bar{t}\,)\\
H_T(J_b,\ J_{\bar{b}}) &= p_T(J_b)+p_T(J_{\bar{b}})
\end{aligned}\tag{6.5}$$

It is immediately apparent that, in line with the differences in the inclusive cross-sections, the NLO corrections to the distributions are in general moderate and negative. The NLO corrections tend to modify the LO distributions in a way that respects the LO shapes in Figure 6.4 on the whole. The curves for $\eta(t)$ and $\eta(l^+)$ are made slightly asymmetric by the NLO corrections; this is well known and will be discussed further in the context of the Forward-Backward asymmetry a little later. We also notice a decreased dependence on the factorization and renormalization scales for the NLO compared with the LO distributions.

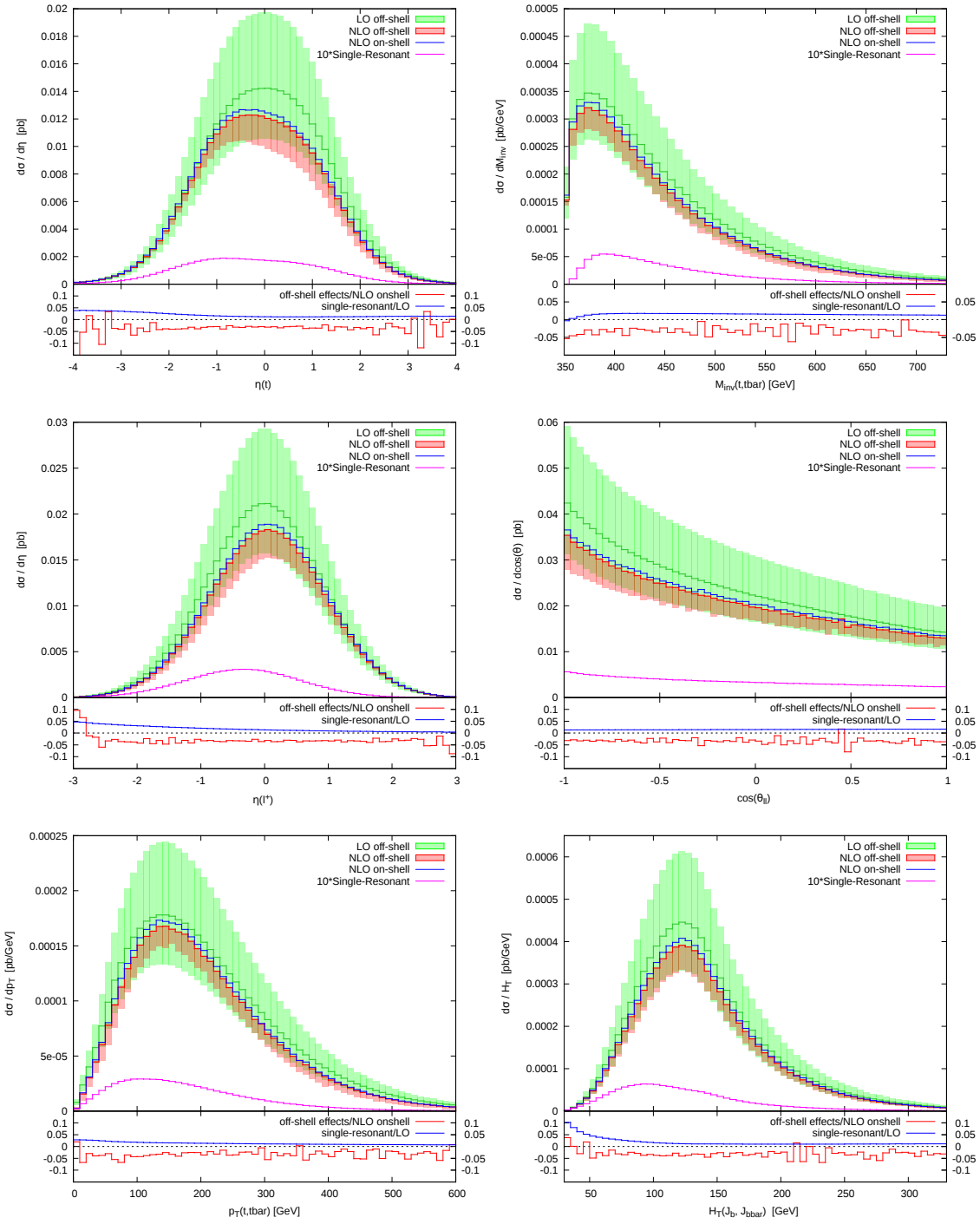

Figure 6.4: A selection of 'standard' kinematical distributions.

The on-shell curves lie slightly above the corresponding off-shell ones with very similar shapes. To quantify this difference, we examine the lower panels to find that for these observables the off-shell effects do not tend to exceed a few per cent of the NLO off-shell results right across the range of bins. The fact that the ratio of off-shell effects versus NLO on-shell is relatively constant more or less over the full ranges means that the shapes predicted by the on-shell calculations for these observables can be trusted. The difference in relaxing the on-shell assumption here only results in a small lowering of the curves. In addition, we point out that for these 'standard' distributions the off-shell effects amount to changes that are smaller in magnitude than the scale uncertainties[3].

It is also clear that the size of the sub-leading terms rarely increases above 1%, except near the lower end of the ranges for the rapidity and $H_T(J_b,\ J_{\bar{b}})$ curves. This is a strong indication that the power-counting is functioning well on a differential level. The shapes of the curves for the sub-leading contributions also in general follows those of the LO distributions.

Figure 6.5 reveals the kinematical distributions for (left to right, top to bottom) the transverse anti-top momentum, $p_T(\bar{t}\,)$, the transverse momentum of the b-jet, $p_T(J_b)$, the rapidity of the negatively charged lepton, $\eta(l^-)$ and the pseudo-rapidity of the top, $y(t)$. The definitions of the latter two are given by

$$\eta(l^-) \equiv y(l^-) = \frac{1}{2}\,\log\left(\frac{p_0(l^-)+p_z(l^-)}{p_0(l^-)-p_z(l^-)}\right)$$

$$y(t) = \frac{1}{2}\,\log\left(\frac{p_0(t)+p_z(t)}{p_0(t)-p_z(t)}\right). \tag{6.6}$$

The upper panels indicate the off-shell LO and NLO results at $\mu = M_t$. For comparison, the separate corrections to the production, top decay and anti-top decay subprocesses as well as the single-resonant contributions (multiplied by a factor of 5) are displayed. The lower panels give the size of the separate NLO factorizable corrections with respect to the LO weights.

As with the previous observables, the overall NLO corrections are negative, though the production and decay corrections are positive and negative respec-

[3]We similarly note that for these observables the off-shell effects are, in general, smaller than the typical uncertainties in the PDFs.

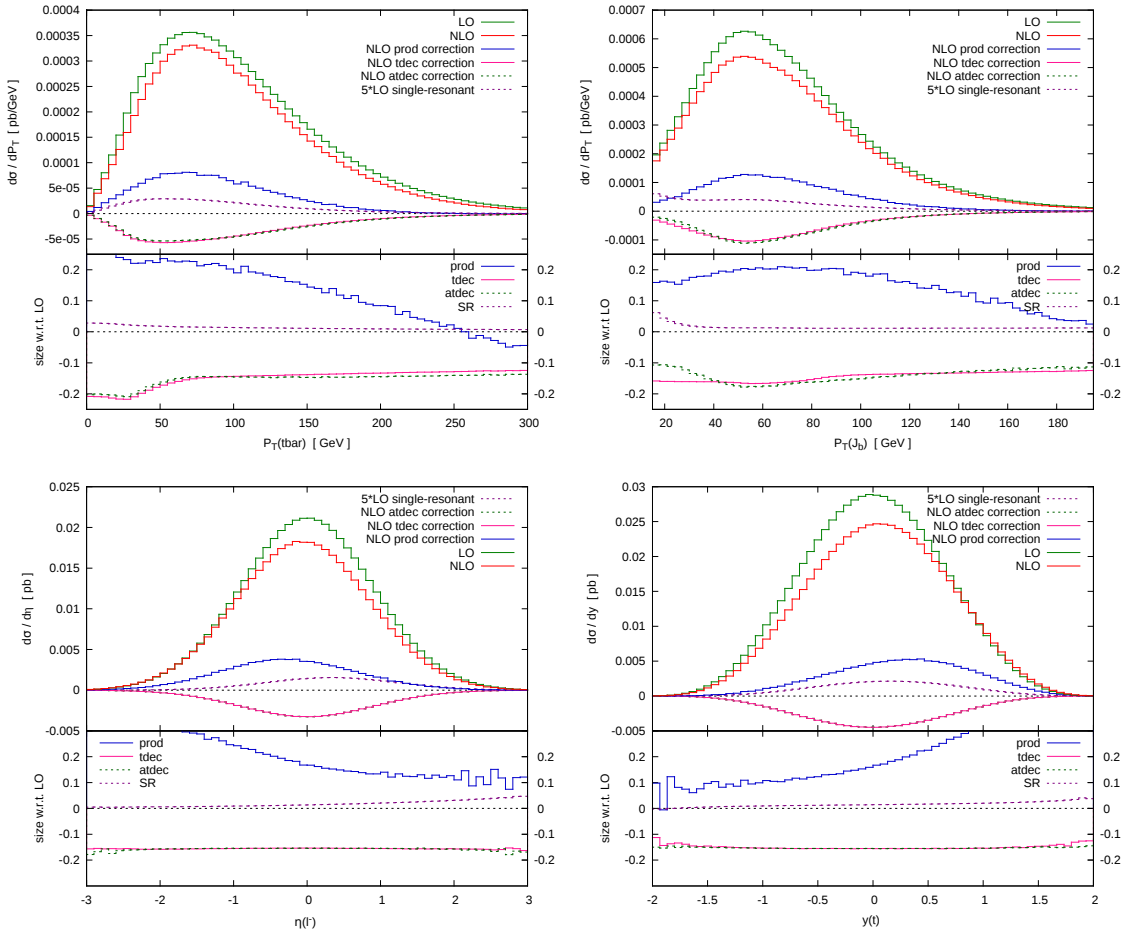

Figure 6.5: A selection of 'standard' kinematical distributions with a breakdown of the various NLO corrections. Plotted in the upper panel are: LO off-shell (green), NLO off-shell (red), NLO production correction (blue), NLO top-decay correction (pink), NLO anti-top decay correction (dashed green) and single-resonant contributions (dashed purple). The lower panels indicate the size of NLO production (blue), top decay (pink), anti-top decay (dashed green) and single-resonant (dashed purple) correction with respect to the LO off-shell predictions.

tively, with the former constituting corrections ranging from 10% to upwards of 30%, whilst the former yield corrections consistently between -10% and -20%. The lower panels also clearly point out that the effects of the single-resonant diagrams are by far eclipsed by the NLO corrections, giving correction with respect

to LO of the order of 1% for the greatest part of the kinematical ranges considered here.

The breakdown of contributions, as presented in Figure 6.5, allows for the identification of some interesting behaviour of the NLO corrections. For the rapidity distributions it is clear that the asymmetrical shapes at NLO come about due to the asymmetry present in the corrections to the production subprocess. In contrast, the corrections to top and anti-top decay are flat in rapidity and simply result to a lowering of the LO curves. It is also interesting to observe that there is a small asymmetry arising from the single-resonant contributions, though this is clearly outweighed by that of the production corrections.

Moving on to examine the p_T distributions, we find that the production corrections tend to decrease for increasing p_T, while the top and anti-top decay are much flatter, however they do become smaller slowly for increasing p_T. The single-resonant contributions are once more drowned out by the NLO factorizable corrections.

6.3.3 Mass-variable Distributions

We now turn to examine distributions that are sensitive to the off-shellness of the top quarks and thus of greater interest in this work. The first of these is the invariant mass of the top, displayed in Figure 6.6. Such distributions are not only important for the study of off-shell effects, but also experimentally are the basis for the modelling of 'templates' used for fitting data curves in the extraction of the top mass. Thus precisely how higher-order corrections affect the shapes of such curves is of vital importance to control.

In the upper panel, the green and red curves once again indicate the LO and NLO off-shell predictions whilst the blue line traces the NLO on-shell curve. The LO on-shell distribution would be a delta-function centered on M_t, which is not drawn in the figure. The LO off-shell curves show the standard Breit-Wigner distributions, whilst it is clear that the NLO corrections significantly modify the curves by smoothing out the sharp LO result. An important feature to pick out is that the NLO on-shell distribution displays a significantly different shape to the corresponding off-shell one. The higher-order corrections in the on-shell case

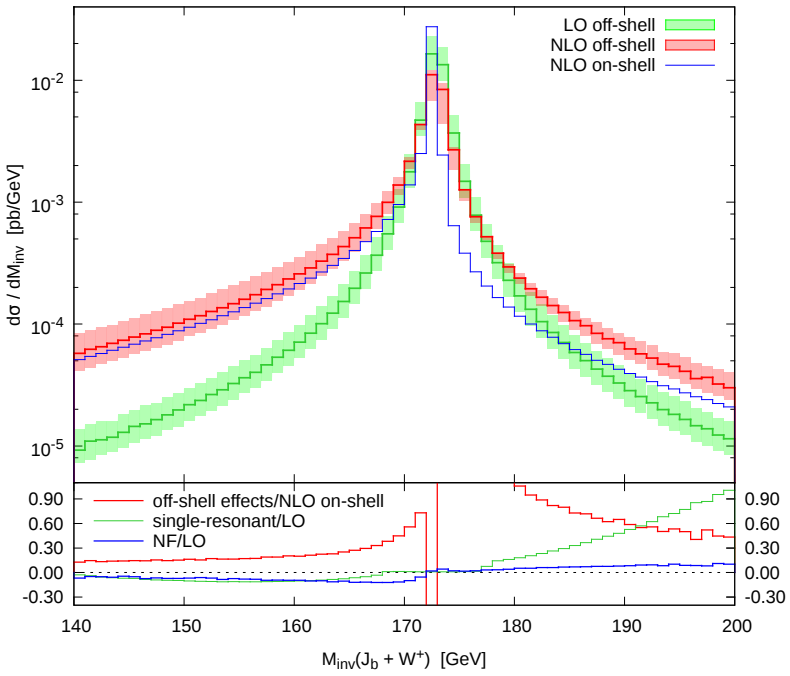

Figure 6.6: The $M_{\rm inv}(t) = M_{\rm inv}(J_b + W^+)$ distribution. The upper panel displays the LO (green) and NLO (red) off-shell results under scale variation, along with the NLO on-shell curve (blue) and the single-resonant contributions multiplied by a factor of 10 (purple). The lower panel indicates the size of off-shell effects (red) with respect to NLO on-shell and of non-factorizable corrections (blue) and single-resonant contributions (green) with respect to the LO off-shell prediction.

cannot cure the delta-function spike at M_t present at LO, the contrast with the off-shell NLO being particularly stark for $M_{\rm inv}(t)$ or $M_{\rm inv}(\bar{t}\,) > M_t$.

The lower panel of Figure 6.6 indicates the size of the off-shell effects (red) and single-resonant contributions (blue) with respect to the NLO off-shell results. The former highlight the fact that the off-shell corrections are large, especially in the region around M_t where, in places, they exceed 80-90%. The regions above M_t also display larger off-shell corrections. It should also be pointed out that the single-resonant contributions start becoming competitive with the NLO corrections when moving to greater values of $M_{\rm inv}(t)$ or $M_{\rm inv}(\bar{t})$ away from M_t.

In the remainder of this subsection we study three 'transverse' masses - ob-

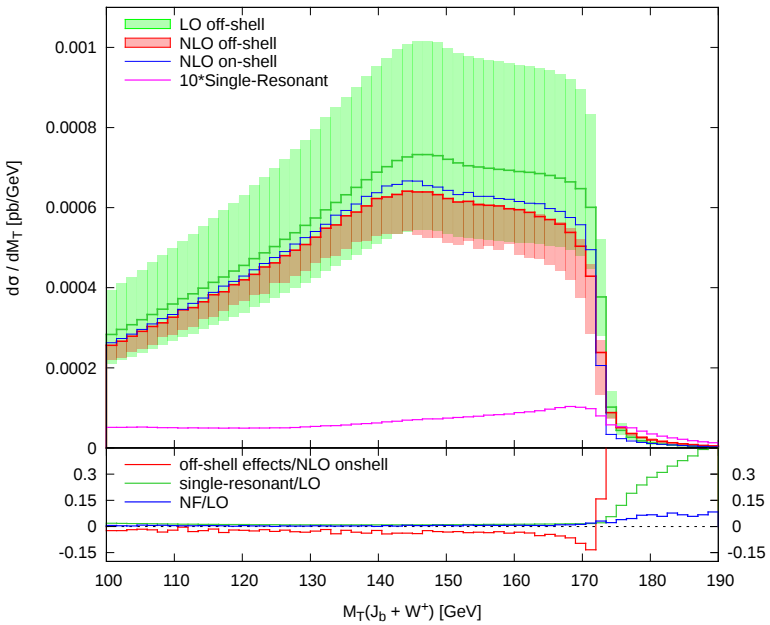

Figure 6.7: The $M_T(t)$ distribution. The upper panel displays the LO (green) and NLO (red) off-shell results under scale variation, along with the NLO on-shell curve (blue) and the single-resonant contributions multiplied by a factor of 10 (purple). The lower panel indicates the size of off-shell effects (red) and single-resonant contributions (blue) with respect to the NLO on-shell prediction.

servables that are sensitive to off-shell effects. These are defined here by

$$M_T(t) = \left((|\vec{p}_T(J_b)| + |\vec{p}_T(l^+)| + |E_T(\nu_l)|)^2 - (\vec{p}_T(J_b) + \vec{p}_T(l^+) + \vec{p}_T(\nu_l))^2\right)^{1/2}$$

$$M_{Tr}(t) = \left((p(J_b) + p(l^+))^2 + 2(E_T(b,\, l^+)E_T(\nu_l) - (\vec{p}_T(J_b) + \vec{p}_T(l^+)) \cdot \vec{p}_T(\nu_l))\right)^{1/2}$$

$$M_{Tr2}(t) = \left((p(J_b) + p(l^+) + p(\nu_l))^2 + (\vec{p}_T(J_b) + \vec{p}_T(l^+) + \vec{p}_T(\nu))^2\right)^{1/2} \tag{6.7}$$

where $\vec{p}_T(k)$ is the transverse momentum of the final state k and $E_T(b,\, l^+) = [(p(J_b) + p(l^+))^2 + (\vec{p}_T(J_b) + \vec{p}_T(l^+))^2]^{1/2}$. The same variables for the anti-top are obtained by swapping $\{J_b \leftrightarrow J_{\bar{b}},\ l^+ \leftrightarrow l^-,\ \nu_l \leftrightarrow \bar{\nu}_l\}$. A common property shared by the distributions of all three of these variables is that, when the tops are assumed to be on-shell, they display sharp edges at M_t. Relaxing the on-shell assumption therefore is expected to result in significant effects near these edges. Once again, it is highly desirable to understand how the shapes of these curves

change when the off-shellness of the tops is accounted for.

Figures 6.7, 6.8 and 6.9 depict distributions for $M_T(t)$, $M_{Tr}(\bar{t})$ and $M_{Tr2}(\bar{t})$ respectively, where the feature of an edge is clearly visible in all three. The lower panel indicates the significance of the off-shell effects and single-resonant contributions. The three plots show that off-shell effects are small over most of the allowed ranges. However, near the edges, the off-shell effects become important. Their absolute effect can reach values exceeding 20% locally, but more importantly, the sign of these (large) effects changes in crossing the M_t boundary. This crucially changes the shape of each distribution by smearing the region around M_t, leading to much less pronounced edges.

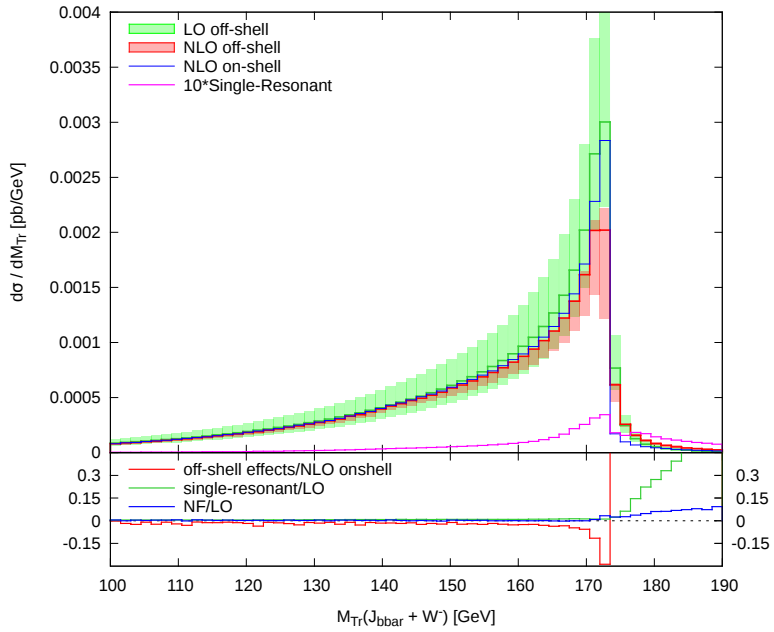

Figure 6.8: The $M_{Tr}(\bar{t})$ distribution. The upper panel displays the LO (green) and NLO (red) off-shell results under scale variation, along with the NLO on-shell curve (blue) and the single-resonant contributions multiplied by a factor of 10 (purple). The lower panel indicates the size of off-shell effects (red) with respect to NLO on-shell and non-factorizable (blue) and single-resonant contributions (green) with respect to the LO off-shell prediction.

It was pointed out in [62, 63] that the pattern of off-shell effects increasing in significance near edges or kinematic boundaries in distributions occurs due to an averaging effect becoming less effective. In general, the weight of a particular

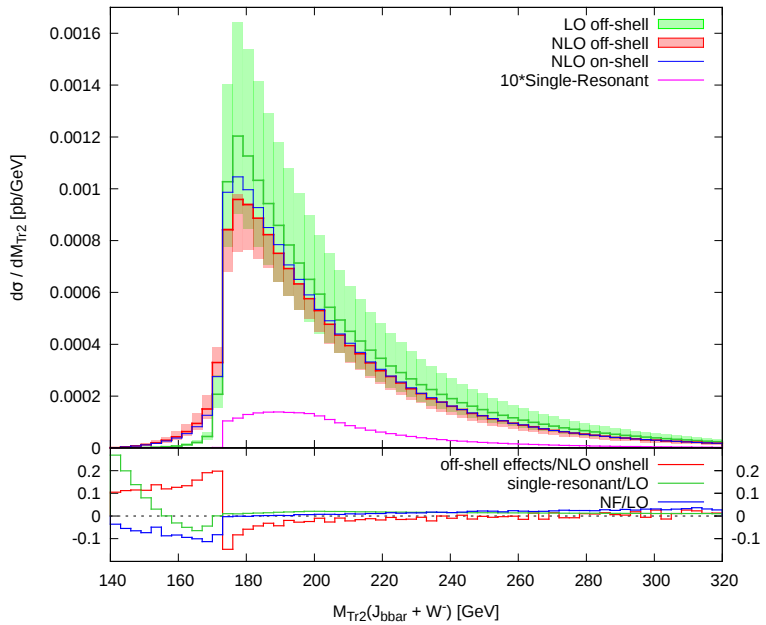

Figure 6.9: The $M_{Tr2}(\bar{t}\,)$ distribution. The upper panel displays the LO (green) and NLO (red) off-shell results under scale variation, along with the NLO on-shell curve (blue) and the single-resonant contributions multiplied by a factor of 10 (purple). The lower panel indicates the size of off-shell effects (red) with respect to NLO on-shell and non-factorizable (blue) and single-resonant contributions (green) with respect to the LO off-shell prediction.

observable in a particular bin will receive contributions from events with $M_{\rm inv}(t)$ and $M_{\rm inv}(\bar{t}\,)$ anywhere in the range [140, 200] GeV (as required by the cuts imposed). Due to the fact that the off-shell effects change sign near $M_{\rm inv}(t) \simeq M_t$ and $M_{\rm inv}(\bar{t}\,) \simeq M_t$ this leads to an averaging of the impact the off-shellness has in that bin[4]. However, for bins which can receive contributions from events with, say, only $M_{\rm inv}(t) > M_t$, then this averaging effect is spoiled to some degree, leading to the off-shell contributions having a more noticeable effect.

Once again, the size of the single-resonant diagrams with respect to the LO contributions is generally very small. However, near the tails of the distributions and more specifically in regions of high top and anti-top invariant masses, effects from these sub-leading parts can become important. In such regions of

[4]This is actually the reason why off-shell effects are modest for the 'standard' observables studied. Most (or all) bins of such distributions will receive contributions from events spanning the full range of $M_{\rm inv}(t)$ and $M_{\rm inv}(\bar{t}\,)$, thus leading to large cancellations and small effects.

phase-space however, the cross-section is so small that at least for the observables studied here, it is not clear if these effects will be of practical importance.

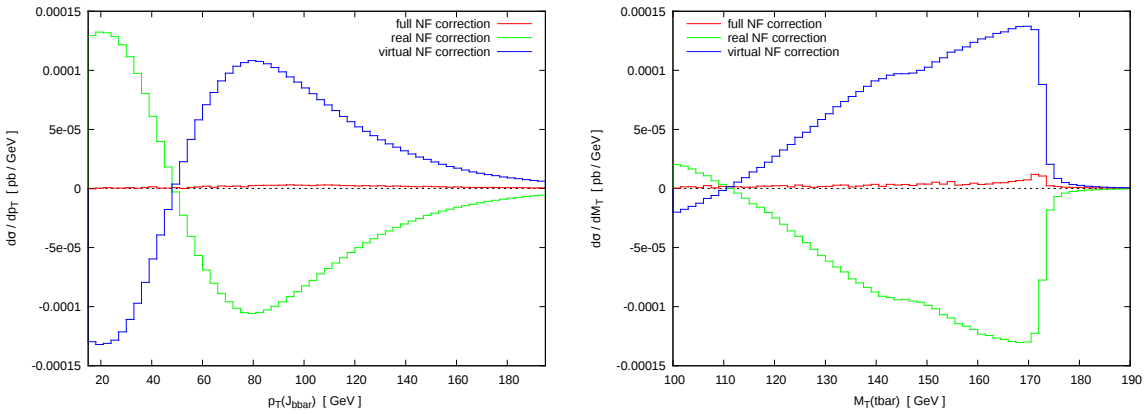

Figure 6.10: Plots indicating the large cancellation occurring within the non-factorizable corrections. The full non-factorizable correction is shown in red, whilst the real and virtual contributions to this are in green and blue respectively.

Finally, it is interesting to examine the non-factorizable pieces separately. Figure 6.10 shows the real and virtual parts of these small pieces separately. Of course, these are themselves not physical quantities, however the plots indicate the large and delicate cancellations amongst the components of the non-factorizable corrections that conspire to make the latter so modest in size. For observables, such as $p_T(J_{\bar{b}})$ on the left, the cancellations are almost perfect, leading to tiny corrections. In the case of observables that are less inclusive in the top and anti-top invariant masses (at least in some regions of phase-space), the cancellations are not as good leading to slightly larger effects. The figure can be viewed as a visualization of the cancellation theorems of [50, 51] promoted to the fully differential level.

6.3.4 The Forward-Backward Asymmetry

The top forward-backward (FB) asymmetry (and the related leptonic asymmetry) has been measured by the CDF and DO Tevatron experiments to be larger than that given by SM predictions (at present) [70, 71]. This has sparked much activity and excitement in the theory community with numerous new physics models

devised to explain the apparent discrepancy.

One of the standard inclusive top asymmetries studied is

$$A_{\mathrm{FB}} = \frac{\sigma(\Delta y > 0) - \sigma(\Delta y < 0)}{\sigma(\Delta y > 0) + \sigma(\Delta y < 0)} \tag{6.8}$$

where $\Delta y = y(t) - y(\bar{t}\,)$ and the related leptonic asymmetry

$$A^{l}_{\mathrm{FB}} = \frac{\sigma(\eta(l^+) > 0) - \sigma(\eta(l^-) < 0))}{\sigma(\eta(l^+) > 0) + \sigma(\eta(l^-) < 0))}. \tag{6.9}$$

In the SM, the FB asymmetry is zero at LO (when considering solely the QCD contributions to top-pair production diagrams) and becomes non-zero at NLO. This comes about due to the asymmetry present in the one-loop box corrections to $q\bar{q} \to t\bar{t}$ as well as that in the interference of initial-final state radiation in the real corrections under $t \leftrightarrow \bar{t}$ exchange[5] [72]. At NLO in QCD, the SM predicts a relatively small (inclusive) FB asymmetry due to a partial cancellation of the asymmetric contributions between real and virtual.

Here we study the relevant differential observables

$$\begin{aligned} \text{top asymmetry:} \quad & \frac{d\sigma}{dy(t)} - \frac{d\sigma}{dy(\bar{t}\,)} \\ \text{lepton asymmetry:} \quad & \frac{d\sigma}{d\eta(l^+)} - \frac{d\sigma}{d\eta(l^-)} \end{aligned} \tag{6.10}$$

paying particular attention to the effects introduced by relaxing the assumption that the top quarks are on-shell. It is to be expected from our previous experience with rapidity observables (see Figure 6.4), where off-shell effects were found to be consistently small, that these effects will not affect the asymmetries much at all.

Examining Figure 6.11, where the upper panels display the NLO on-shell and off-shell curves along with the sub-leading terms, we see that this is indeed the case. The lower panels measure the importance of the off-shell effects and single-

[5]The gluon-gluon initiated channel is symmetric under charge conjugation thus gives zero contribution to the FB asymmetry. This means that at the LHC, where top-pair production is dominated by the gg-channel, this asymmetry is very challenging to study.

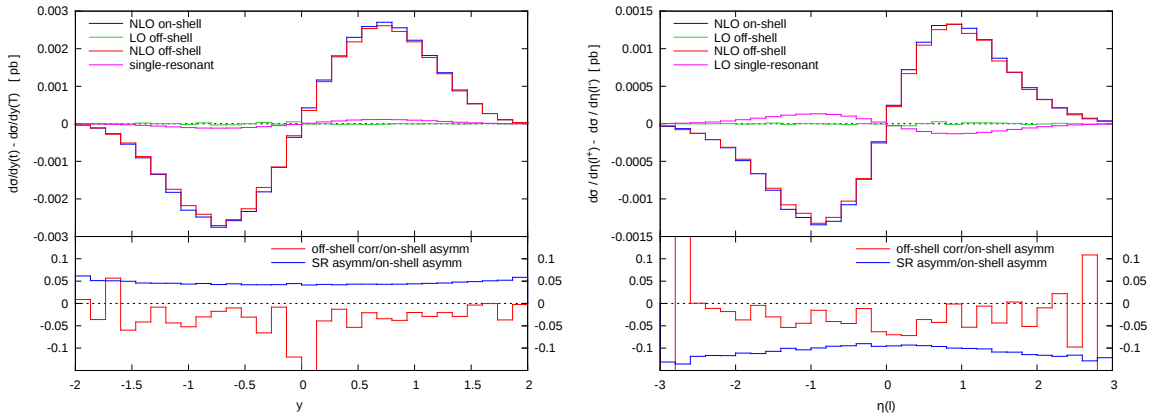

Figure 6.11: Top (left) and lepton (right) differential asymmetries as defined in (6.10). The upper panels show the LO (green) and NLO (red) off-shell, NLO on-shell (blue) and single-resonant (purple) curves. The lower panel shown the ratio of off-shell effects (red) and single-resonant contributions (blue) versus the NLO on-shell result.

resonant contributions with respect to the NLO on-shell predictions. From this we can gauge that going from on-shell to off-shell on the whole tends to reduce the asymmetry by 2-3%. What is perhaps more interesting in the plots is that the effects introduced by the sub-leading terms are comparable with the off-shell effects. For the case of the top asymmetry the sub-leading terms enhance the on-shell results by about 5%, whilst for the leptonic observable, they make up corrections of -10%. The single-resonant contributions give rise to an asymmetry due to the fact that they contain diagrams with W-boson emissions off initial state b-quarks. We note that this is not the full set of sub-leading contributions to the FB asymmetry as there is a non-zero LO EW correction which we have not included.

6.3.5 Effects of using the PS-mass scheme

In this subsection we explore the effects of using a PS-mass of 172.9 GeV instead of a pole mass of the same numerical value. As an example, we have chosen to fix the PS-scale to $\mu_{ps} = 20$ GeV. This corresponds to a pole mass of $M_t^{OS} \simeq$ 174.3 GeV (see (5.59)) with the difference between the two masses being roughly

the same as the current experimental uncertainty on the top mass [73]. The aim here is to investigate whether it is at all feasible to distinguish between the two schemes, albeit without the rigour of a full experimental analysis.

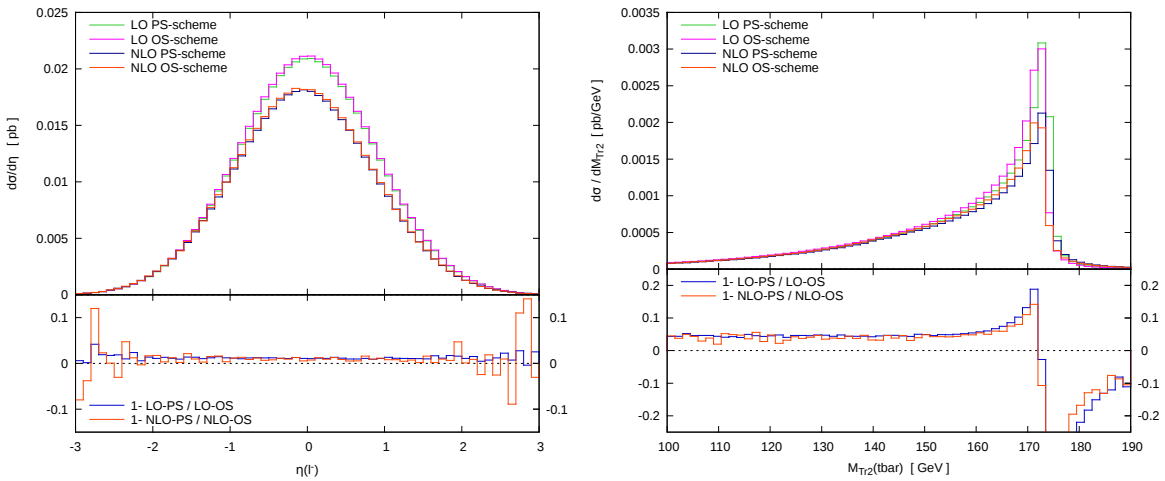

Figure 6.12: Kinematical distributions for $\eta(l^-)$ (left) and $M_{Tr}(\bar{t})$ (right). The upper panels display LO and NLO curves in the OS-scheme and PS-scheme with $\mu_{ps} = 20$ GeV. The lower panels plot the ratio of the difference in the predictions using the OS-scheme and PS-scheme relative to the OS-scheme, at LO and NLO.

Figure 6.12 displays two distributions with contrasting effects. For the first of these, the rapidity of the negatively charged lepton, $\eta(l^-)$, using the PS-mass has a very small effect of roughly 1% over the full range of η. The two curves at LO and NLO have the same shapes and can hardly be distinguished from one another. However, the changes are slightly more visible in the second distribution plotted. Given that the pole mass is greater than 172.9 GeV for the value of the PS-mass chosen, a shift of the edge of the distribution in the PS-scheme to slightly higher values of M_{Tr2} is noticed relative to the OS-scheme curves. The shift due to the different pole mass is evident in the constant 4% difference in the curves over the lower range of M_{Tr2} and the stark differences near the edge.

Making use of the distributions sensitive to the top mass definition it would be interesting to see whether or not the two different masses can be distinguished. The result for M_{Tr} indicate that there is a fairly sizeable difference between the two, however, a realistic analysis would need to be performed to evaluate if this is feasible.

Chapter 7

Conclusions and Outlook

A summary of the main ideas and results presented in this thesis is given in this final chapter along with an outlook for future research and developments that could follow on from this work.

7.1 Conclusions

The top quark has played a key part for much phenomenology at the Fermilab Tevatron and will continue to do so for many years at the LHC at CERN. Understanding its properties in detail will not only allow for a better grasp of the SM but will also aid physicists along the quest for new physics.

The main goal of the work presented in this thesis has been a description of top quark production processes at hadron colliders respecting the important properties of top quarks, namely that they are massive and, because of their large width, they decay before forming bound states. The assumption that the top quark is on-shell, known as the Narrow-Width Approximation, simplifies the calculations significantly, however, it evidently disregards any effects the non-zero virtuality may introduce.

As the bulk of the cross-section for processes involving the production of unstable tops lies in the resonant regions (where $p_t^2 \sim M_t^2$) the description we have aimed at is one that is valid here, without resorting to the on-shell assumption. ETs systematically pick out the dominant physics in different regions of momentum space via expansions of scattering amplitudes in small parameters. In the

material presented here ET ideas have been employed to aid the extraction of the dominant physics in regions of phase space where the top quarks are resonant.

The realisation of a simultaneous double expansion of the full process amplitudes about the complex poles of resonant propagators as well as in the perturbative couplings α_s and $\alpha_{\rm ew}$ is precisely what is required to describe the resonant regions efficiently. This is made possible by the introduction of an ET power-counting scheme, along with the use of the method of regions, providing a systematic framework for picking out relevant contributions to such a double expansion from tree-level and loop diagrams in perturbation theory. The expansion in regions separates virtual contributions into hard and soft. The first set corresponds to factorizable corrections to production and decay subprocesses whilst the latter, the non-factorizable corrections, link up these two, which are moderately separated in phase-space.

In the description of differential observables, the real corrections have to be explicitly dealt with, unlike in the case of inclusive quantities where they can be dealt with in line with the virtual corrections by use of the Optical Theorem. However, the treatment of the real corrections must be consistent with the method of regions used for the loop corrections if the desirable feature of the complete separation into factorizable and non-factorizable pieces is to hold. This would not only allow for the examination of the properties of these sets of corrections individually, but also for a better way of evaluating these, namely at their natural hard and soft scales. We have presented a method of treating the real corrections for general differential observables that enables this desired full split.

These ET inspired methods have been applied to the case of top-pair production. In particular, the focus has been on the $q\bar{q}$-initiated channel that dominates at the Tevatron. A number of distributions have been studied for a basic experimental setup and a detailed comparison made with the predictions made in the iNWA. For observables inclusive in the invariant top and anti-top masses the differences between treating the tops as on-shell and off-shell are modest, the off-shell effects usually making up negative corrections of 2-4% to the NLO on-shell results. However, differential observables that are less inclusive in $M_{\rm inv}(t)$ can and do display more significant enhancements of the off-shell corrections. In particular, for distributions possessing sharp edges at kinematic boundaries, the transi-

tion from on-shell to off-shell is often stark, with corrections even exceeding 15% and moreover, resulting in a modification of the distribution shape. In addition to these studies, differential observables related to the Forward-Backward asymmetry have been presented, where, as for other quantities inclusive in $M_{\text{inv}}(t)$, including the off-shellness of top quarks results in minor modifications. We have also shown that it is possible to use a scheme other than the pole mass-scheme in our ET method. For the observables studied, the differences between the pole and PS schemes are small, though larger effects can be seen near sharp edges due to differences in the pole mass in the two schemes.

We emphasise that the framework presented for the treatment of unstable heavy tops is applicable with only minor modifications to processes involving other unstable particles and thus it may well be of importance in the coming years where any new particles discovered by the LHC are likely to be both heavy and unstable. The method is a systematically improvable one and moreover, the ET structures found at 'N'LO can guide one in the computation of higher order terms. The computation of corrections to the matching coefficients as well as the introduction of higher suppressed operators in a strict ET approach, points us to include such effects in the counterparts to these, where unstable particle production is concerned.

7.2 Outlook

Finally, we give an outlook as to how the work discussed in this thesis can be improved on and extended. Once the gluon-gluon and gluon-quark initiated processes have been included a realistic description of resonant top-pair production and decay for the LHC will be possible. Including these additional subprocesses can be included using the framework presented in Chapter 5 without modifications. Going beyond this involves further developing the ET approach in a number of different directions in order that the accuracy of the predictions made is increased.

The first of these directions is related to one of the limitations to the method, namely that the invariant mass of the pair of unstable tops must be kept above

threshold in order that the ET power-counting remains valid. As discussed, the ET would have to be slightly modified in order to account correctly for the new, 'potential' region encountered near threshold. Although the numerical effects of describing such a region properly in a hadron collider context is likely to only result in small corrections, it would be both desirable and essential to do so in the case of pair-production at a linear collider, where the expected precision with which properties such as the top mass could be measured is significantly higher. This improvement would require the smooth interpolation between the method of this work and one based upon NRQCD. Once more, a big hurdle here would be the treatment of the real contributions in a fashion similar to the virtual corrections, allowing for the study of fully differential observables.

Improvements to the method presented here could be achieved through making the description of the processes involving unstable particles better. A clear way this can be done is to include higher order corrections. Here we have included corrections of $\mathcal{O}(\delta^{1/2})$ to the LO predictions, which have, for the most part, included one-loop and single real-emission QCD corrections. The computation of $\mathcal{O}(\delta)$ corrections would require us to include two-loop QCD and one-loop EW corrections to the double-resonant diagrams along with their real correction counterparts, as well as all appropriate tree-level single-resonant contributions. This would certainly be a tough challenge, but it would definitely be simpler than computing, say, the full two-loop corrections to $W^+\,b\,W^-\,\bar{b}$ production.

To finish, we stress that the ET inspired methods have allowed for the clean split of hard and soft corrections. Here we have evaluated both sets using a common hard scale. However, to minimize the effects of large logarithms appearing in both sets, each ought to be evaluated at its appropriate scale. More precisely, the hard scale $\mu_h = M_t$ should be used for the factorizable corrections and the soft scale $\mu_s = \Gamma_t$ for the non-factorizable. To do this consistently, the hard corrections should be run down from μ_h to μ_s using renormalization group equations and predictions be made at the common scale μ_s. This would achieve a resummation of logarithms of the form μ_s/μ_h and in this way would avoid the presence of unwanted large logarithms in both sets. Furthermore, this may actually lead to an enhancement of the soft corrections since the value of $\alpha_s(\mu)$ grows at smaller μ. Extending the framework discussed throughout this thesis to allow for such a

resummation would be of phenomenological interest for the process at hand, as well as perhaps giving some indication as to how to include other resummation effects for arbitrary exclusive observables.

Appendix A: Momentum Projections

Due to the fact that in the work presented in this thesis we study the effects of treating top quarks as off-shell, we generate phase-space such that at Born-level the momentum configurations satisfy

$$\{p_i\}_1^8 : \qquad p_t^2 = (p_3 + p_5 + p_6)^2 \neq M_t^2 \text{ and } \; p_{\bar{t}}^2 = (p_4 + p_7 + p_8)^2 \neq M_t^2 \tag{1}$$

and for the real corrections momenta are produced such that

$$\begin{aligned} \{p_i\}_1^9 : \qquad & p_t^2 = (p_3 + p_5 + p_6)^2 \neq M_t^2 \text{ and } \; p_{\bar{t}}^2 = (p_4 + p_7 + p_8)^2 \neq M_t^2 \\ & p_{t9}^2 = (p_3 + p_5 + p_6 + p_9)^2 \neq M_t^2 \text{ and } \; p_{\bar{t}9}^2 = (p_4 + p_7 + p_8 + p_9)^2 \neq M_t^2. \end{aligned} \tag{2}$$

These are the momentum configurations that must be used for binning, as indicated in (5.90). However, the ET power-counting along with the pole expansion dictate that the residues of the top quark propagators must be evaluated with on-shell top momenta. This means that the weight from the matrix element, except for the denominators of the top propagators themselves, must be one obtained using a configuration where the top quarks are on-shell. Clearly it is necessary to project the fully off-shell configurations to on-shell ones.

Projection for Born and virtual terms

For the Born and virtual matrix elements the situation is fairly straightforward. We must construct a projection that maps $\{p_i\}_1^8$ to $\{\tilde{p}_i\}_1^8$, where $(\tilde{p}_3+\tilde{p}_5+\tilde{p}_6)^2 = M_t^2$ and $(\tilde{p}_4+\tilde{p}_7+\tilde{p}_8)^2 = M_t^2$, allowing for the residues of the double-resonant matrix elements to be evaluated on-shell. For the results presented in Chapter 6, we have used the following mappings:

$$\begin{aligned} \tilde{p}_{3,5,6} &= \frac{p_{3,5,6}}{x} \\ \tilde{p}_{4,7,8} &= \frac{p_{4,7,8}}{y} \end{aligned} \tag{3}$$

with

$$\begin{aligned} x &= \frac{p_t^2}{M_t^2} \\ y &= \frac{p_{\bar{t}}^2}{M_t^2}. \end{aligned} \tag{4}$$

The sum of the initial momenta is mapped as follows

$$p_1 + p_2 \to \tilde{q} = \tilde{q}_1 + \tilde{q}_2 \tag{5}$$

where

$$\tilde{q} = p_1 + p_2 - p_t(1 - \frac{1}{x}) - p_{\bar{t}}(1 - \frac{1}{y}). \tag{6}$$

$\tilde{q}_1$ and $\tilde{q}_2$ are arbitrary but still light-like. The decomposition of $\tilde{q}$ into $\tilde{q}_1 + \tilde{q}_2$ is similar to (2.9), where the massive top momentum is written as a linear combination of two light-like momenta.

Projections for real terms

Projections for the real corrections must come in three variants since in the presence of an additional gluon, the factorizable corrections are split into real emission corrections to one of the production, top decay or anti-top decay vertices. This results in three possible situations: either $p_t^2 = p_{\bar{t}}^2 = M_t^2$ (production), $p_{t9}^2 = p_{\bar{t}}^2 = M_t^2$ (top decay) or $p_t^2 = p_{\bar{t}9}^2 = M_t^2$ (anti-top decay), for each of which an appropriate mapping of momenta must be made. The projections used are similar to the one used above for the Born and virtual terms.

For the factorizable corrections to the production subprocess, we have exactly the same projection as above, with the gluon momentum unchanged, i.e. $\tilde{p_9} = p_9$. In the case of emissions off the top decay vertex, we use

$$\begin{aligned} \tilde{p}_{3,5,6,9} &= \frac{p_{3,5,6,9}}{x} \\ \tilde{p}_{4,7,8} &= \frac{p_{4,7,8}}{y} \end{aligned} \tag{7}$$

with x and y now given by

$$\begin{aligned} x &= \frac{p_{t9}^2}{M_t^2} \\ y &= \frac{p_{\bar{t}}^2}{M_t^2}. \end{aligned} \tag{8}$$

The projection for the anti-top decay scenario is given by the top decay projection with the swaps $p_{3,5,6} \leftrightarrow p_{4,7,8}$, $p_{t9} \to p_t$, $p_{\bar{t}} \to p_{\bar{t}9}$ and $x \leftrightarrow y$.

The caveats to using this set of projections is that the new incoming momenta $\tilde{q}_{1,2}$ are no longer head on. In addition, the modified leptonic momenta satisfy

$$(p_5 + p_6)^2 = \frac{M_W^2}{x^2} \qquad\qquad (p_7 + p_8)^2 = \frac{M_W^2}{y^2}, \tag{9}$$

i.e. do not reconstruct the physical W-bosons. This is not a problem since the projected momenta $\{\tilde{p}_i\}$ are not the physical momenta, but only the momenta

that are used for evaluating (part of) the matrix element weights.

We note that this projection is by no means unique. In fact it may be of concern that this is the case since different projections would in general lead to different results. Due to the fact that the projection mapping off-shell to on-shell is a kind of expansion of the momenta, then we would expect that using alternative projections gives results that are different, but close enough such that the differences are smaller than our target accuracy. We have checked our results with three projections and the results satisfy the expectations.

Appendix B: Soft Scalar Integrals

Here we catalogue the Scalar integrals relevant for the soft-virtual contributions. The integrals $I_{s.e.}$, I_{tq}, I_{qb} can be found in [62], whereas $I_{t\bar{t}}$, $I_{t\bar{b}}$ and $I_{b\bar{b}}$ were calculated anew. In what follows we will always assume $s_{ij} = 2\, p_i \cdot p_j$.

$$I_{s.e.}(p_t, M_t; \epsilon, \mu) = -16\pi\, i\, \alpha_s \tilde{\mu}^{2\epsilon} \frac{M_t^2}{\Delta_t} \int \frac{d^d k}{(2\pi)^d}\, \frac{1}{k^2}\, \frac{1}{\Delta_t - 2k.p_t} \tag{10}$$

$$= \frac{\alpha_s}{2\pi} \left(\frac{1}{\epsilon} + 2\right) \left(-\frac{\Delta_t}{\mu M_t}\right)^{-2\epsilon} \tag{11}$$

$$I_{tq}(p_t, p_q, M_t; \epsilon, \mu) = -16\pi\, i\, \alpha_s \tilde{\mu}^{2\epsilon} (p_t.p_q) \int \frac{d^d k}{(2\pi)^d}\, \frac{1}{k^2}\, \frac{1}{-2k.p_q}\, \frac{1}{\Delta_t - 2k.p_t} \tag{12}$$

$$= \frac{\alpha_s}{2\pi} \left(\frac{1}{2\epsilon^2} + \frac{5}{24}\pi^2\right) \left(-\frac{\Delta_t}{\mu M_t}\right)^{-2\epsilon} \tag{13}$$

$$I_{t\bar{t}}(p_t, p_{\bar{t}}, M_t; \epsilon, \mu) = 16\pi\, i\, \alpha_s \tilde{\mu}^{2\epsilon} (p_t.p_{\bar{t}}) \int \frac{d^d k}{(2\pi)^d}\, \frac{1}{k^2}\, \frac{1}{\Delta_t - 2k.p_t}\, \frac{1}{\Delta_{\bar{t}} + 2k.p_{\bar{t}}} \tag{14}$$

$$= \frac{\alpha_s}{4\pi}\, \eta \left(\frac{1}{\epsilon} I_{t\bar{t}}^{(-1)} + 2\log\left(\mu\, M_t\right) I_{t\bar{t}}^{(-1)} + I_{t\bar{t}}^{(0)}\right) \tag{15}$$

with $\eta = (s - 2M_t^2)/M_t^2$ and

$$I_{t\bar{t}}^{(-1)} = \frac{\log(-\xi_-) - \log(\xi_+)}{\xi_+ - \xi_-} \tag{16}$$

$$\begin{aligned}
I_{t\bar{t}}^{(0)} = \frac{1}{2(\xi_+ - \xi_-)} \Bigg(& \pi^2 + 2(\log(\xi_+) - i\pi) \log\left(\frac{\xi_-}{\xi_- - \xi_+}\right) \\
& + 4\log(-\Delta_t)(\log(-\xi_+) - \log(-\xi_-)) + \log^2(\xi_+ - \xi_-) - \log^2(\xi_- - \xi_+) \\
& + \log(-\xi_-)\left(4\log\left(\frac{\Delta_t}{\Delta_t + \Delta_{\bar{t}}\xi_-}\right) - 2\log\left(\frac{\xi_+}{\xi_+ - \xi_-}\right) + \log(-\xi_-)\right) \\
& - 2\log^2\left(\frac{\Delta_{\bar{t}}}{\Delta_t + \Delta_{\bar{t}}\xi_+}\right) + 2\log^2\left(\frac{\Delta_{\bar{t}}}{\Delta_t + \Delta_{\bar{t}}\xi_-}\right) \\
& + i\left(4(\pi + i\log(\xi_+))\log\left(\frac{\Delta_t}{\Delta_t + \Delta_{\bar{t}}\xi_+}\right) + (2\pi + i\log(\xi_+))\log(\xi_+)\right) \\
& - 4\mathrm{Li}_2\left(\frac{\Delta_{\bar{t}}\xi_+}{\Delta_t + \Delta_{\bar{t}}\xi_+}\right) + 4\mathrm{Li}_2\left(\frac{\Delta_{\bar{t}}\xi_-}{\Delta_t + \Delta_{\bar{t}}\xi_-}\right) \\
& + 2\mathrm{Li}_2\left(\frac{\xi_+}{\xi_+ - \xi_-}\right) - 2\mathrm{Li}_2\left(\frac{\xi_-}{\xi_- - \xi_+}\right)\Bigg)
\end{aligned} \tag{17}$$

where $\xi_\pm = \frac{\eta \pm \sqrt{\eta^2 - 4 + i o_+}}{2}$.

$$I_{qb}(p_t, p_q, p_b, M_t; \epsilon, \mu) =$$

$$-16\pi\, i\, \alpha_s \tilde{\mu}^{2\epsilon}(p_q.p_b) \int \frac{d^dk}{(2\pi)^d} \frac{1}{k^2} \frac{1}{-2k.p_q} \frac{1}{-2k.p_b} \frac{\Delta_t}{\Delta_t - 2k.p_t} \tag{18}$$

$$= \frac{\alpha_s}{2\pi}\left(-\frac{1}{\epsilon^2} - \frac{1}{\epsilon}\log\left(\frac{s_{qt}\, s_{bt}}{M_t^2 s_{qb}}\right) + \mathrm{Li}_2\left(1 - \frac{s_{qt}\, s_{bt}}{M_t^2 s_{qb}}\right) - \frac{5}{12}\pi^2\right)\left(-\frac{\Delta_t}{\mu M_t}\right)^{-2\epsilon} \tag{19}$$

$$I_{t\bar{b}}(p_t, p_{\bar{t}}, p_{\bar{b}}, M_t; \epsilon, \mu) =$$

$$16\pi\, i\, \alpha_s \tilde{\mu}^{2\epsilon}(p_t.p_{\bar{b}})\, \Delta_t \int \frac{d^dk}{(2\pi)^d}\, \frac{1}{k^2}\, \frac{1}{2k.p_{\bar{b}}}\, \frac{1}{\Delta_t - 2k.p_t}\, \frac{1}{\Delta_{\bar{t}} + 2k.p_{\bar{t}}} \tag{20}$$

$$= -\frac{\alpha_s}{2\pi}\, \Delta_{\bar{t}} \left(\frac{1}{\epsilon} I_{t\bar{b}}^{(-1)} + 2\log(\mu\, M_t)\, I_{t\bar{b}}^{(-1)} + I_{t\bar{b}}^{(0)} \right) \tag{21}$$

with

$$I_{t\bar{b}}^{(-1)} = \frac{\log(-\xi_4) + \log(-\Delta_t) - \log(-\Delta_{\bar{t}})}{\xi_4 \Delta_t + \Delta_{\bar{t}}} \tag{22}$$

and

$$
\begin{aligned}
I^{(0)}_{t\bar{b}} = -\frac{1}{6(\Delta_t\xi_4+\Delta_{\bar{t}})}\Big(&7\pi^2 - 6i\pi\log(\xi_4) - 6\log(\xi_-)\log(\xi_4)\\
&+ 6\log(-\xi_-)(\log(-\Delta_{\bar{t}}) - \log(-\Delta_t\xi_- - \Delta_{\bar{t}}))\\
&+ 6\log(-\xi_+)(\log(-\Delta_{\bar{t}}) - \log(-\Delta_t\xi_+ - \Delta_{\bar{t}}))\\
&- 3\log^2(-\xi_- + \xi_4) + 6\log(\xi_-)\log(-\xi_- + \xi_4)\\
&+ 3\log^2(-\xi_+ + \xi_4) - 6\log(-\xi_4)\log(-\xi_+ + \xi_4)\\
&+ 3(\log(-\Delta_t) - \log(-\Delta_t\xi_- - \Delta_{\bar{t}}))^2 + 3(\log(-\Delta_t) - \log(-\Delta_t\xi_+ - \Delta_{\bar{t}}))^2\\
&+ 6\log^2(\Delta_t\xi_4 + \Delta_{\bar{t}}) - 6\log^2(-\Delta_{\bar{t}})\\
&+ 12\log(-\Delta_{\bar{t}})(-\log(-\Delta_t\xi_4 - \Delta_{\bar{t}}) + \log(-\Delta_t) + \log(\xi_4))\\
&- 6\mathrm{Li}_2\left(\frac{\xi_-}{\xi_- - \xi_4}\right) + 6\mathrm{Li}_2\left(\frac{\xi_4}{\xi_4 - \xi_+}\right)\\
&+6\mathrm{Li}_2\left(\frac{\Delta_t\xi_-}{\Delta_{\bar{t}} + \Delta_t\xi_-}\right) + 6\mathrm{Li}_2\left(\frac{\Delta_t\xi_+}{\Delta_{\bar{t}} + \Delta_t\xi_+}\right) + 12\mathrm{Li}_2\left(\frac{\Delta_{\bar{t}}}{\Delta_{\bar{t}} + \Delta_t\xi_4}\right)\Big)
\end{aligned}
\tag{23}
$$

and $\xi_4 = \frac{s_{4\bar{t}}}{s_{4t}} - io_+$.

$$
\begin{aligned}
&I_{b\bar{b}}(p_t, p_{\bar{t}}, p_b, p_{\bar{b}}, M_t; \epsilon, \mu) =\\
&16\pi\, i\, \alpha_s\tilde{\mu}^{2\epsilon}(p_b.p_{\bar{b}})\, \Delta_t\, \Delta_{\bar{t}} \int \frac{d^dk}{(2\pi)^d}\, \frac{1}{k^2}\, \frac{1}{-2k.p_b}\, \frac{1}{2k.p_{\bar{b}}}\, \frac{1}{\Delta_t - 2k.p_t}\, \frac{1}{\Delta_{\bar{t}} + 2k.p_{\bar{t}}}
\end{aligned}
\tag{24}
$$

An analytical expression for this was found in terms of a decomposition of the pentagon into the soft boxes I_{qb} and $I_{t\bar{b}}$. This decomposition takes the form

$$
\begin{aligned}
&I_{b\bar{b}}(p_t, p_{\bar{t}}, p_b, p_{\bar{b}}, M_t; \epsilon, \mu) = \\
&= -\frac{\alpha_s}{2\pi}\Delta_t\Delta_{\bar{t}}\Big(- \epsilon\, b_1\, I_5^{6-2\epsilon} \\
&+ b_2\, I_{t\bar{b}}(p_t, p_{\bar{t}}, p_{\bar{b}}, M_t; \epsilon, \mu) + b_3\, I_{t\bar{b}}(p_{\bar{t}}, p_t, p_b, M_t; \epsilon, \mu) \\
&+ b_4\, I_{qb}(p_{\bar{t}}, p_b, p_{\bar{b}}, M_t; \epsilon, \mu) + b_5\, I_{qb}(p_t, p_{\bar{b}}, p_b, M_t; \epsilon, \mu)\Big)\,, \qquad (25)
\end{aligned}
$$

where

$$b_1 = \frac{4\, C_t\, C_{\bar{t}} - C_{t\bar{t}}^2}{W_{t\bar{t}}} \qquad (26)$$

$$b_2 = \frac{-2C_t\, s_{\bar{b}t}\, \Delta_t - C_{t\bar{t}}\, s_{\bar{b}\bar{t}}\, \Delta_t + C_{t\bar{t}}\, s_{\bar{b}t}\, \Delta_{\bar{t}} + 2C_{\bar{t}}\, s_{\bar{b}\bar{t}}\, \Delta_{\bar{t}}}{W_{t\bar{t}}} \qquad (27)$$

$$b_3 = \frac{2C_t\, s_{bt}\, \Delta_t + C_{t\bar{t}}\, s_{b\bar{t}}\, \Delta_t - C_{t\bar{t}}\, s_{bt}\, \Delta_{\bar{t}} - 2C_{\bar{t}}\, s_{b\bar{t}}\, \Delta_{\bar{t}}}{W_{t\bar{t}}} \qquad (28)$$

$$b_4 = \frac{s_{b\bar{b}}\,(2C_t\, \Delta_t - C_{t\bar{t}}\, \Delta_{\bar{t}})}{W_{t\bar{t}}} \qquad (29)$$

$$b_5 = \frac{s_{b\bar{b}}\,(2C_{\bar{t}}\, \Delta_{\bar{t}} - C_{t\bar{t}}\, \Delta_t)}{W_{t\bar{t}}} \qquad (30)$$

$$W_{t\bar{t}} = 2\left(C_t\, \Delta_t^2 - C_{t\bar{t}}\, \Delta_t\, \Delta_{\bar{t}} + C_{\bar{t}}\, \Delta_{\bar{t}}^2\right) \qquad (31)$$

$$C_t = M_t^2\, s_{b\bar{b}} - s_{b\bar{t}}\, s_{\bar{b}\,t} \qquad (32)$$

$$C_{\bar{t}} = M_t^2\, s_{b\bar{b}} - s_{bt}\, s_{\bar{b}\,t} \qquad (33)$$

$$C_{t\bar{t}} = s_{b\bar{t}}\, s_{\bar{b}t} + s_{bt}\, s_{\bar{b}\bar{t}} - s_{b\bar{b}}\, s_{t\bar{t}}. \qquad (34)$$

The expression for $I_5^{6-2\epsilon}$ is given by

$$I_5^{6-2\epsilon} = -\frac{1}{2\epsilon}\frac{1}{s_{b\bar{b}}M_t^2 - s_{b\bar{t}}\,s_{\bar{b}\bar{t}}}\left(\log\left(\frac{s_{b\bar{t}}\,s_{\bar{b}\bar{t}}}{M_t^2\,s_{b\bar{b}}}\right) I_{5,0}\right.$$
$$\left. + I_{5,1}(\xi_3) + I_{5,1}(1/\xi_4) - I_{5,1}(\zeta_+) - I_{5,1}(\zeta_-)\right), \tag{35}$$

where

$$I_{5,0} = \frac{\log(-Z_+) - \log(-Z_-)}{Z_- - Z_+} \tag{36}$$

$$\begin{aligned} I_{5,1}(x_z) = \frac{1}{Z_- - Z_+}\Bigg(&\mathrm{Li}_2\left(\frac{Z_-}{Z_- - \mathrm{Re}(x_z)}\right) - \mathrm{Li}_2\left(\frac{Z_+}{Z_+ - \mathrm{Re}(x_z)}\right) \\ &+ \frac{1}{2}\left(\log^2(\mathrm{Re}(x_z) - Z_+) - \log^2(\mathrm{Re}(x_z) - Z_-)\right) \\ &+ \log\left(1 - \frac{\mathrm{Re}(x_z)}{Z_-}\right)\left(\log\left(1 - \frac{\mathrm{Re}(x_z)}{Z_-}\right) - \log\left(-\frac{1}{Z_-}\right) + i\pi\right) \\ &- \log^2\left(1 - \frac{\mathrm{Re}(x_z)}{Z_+}\right) + \left(\log\left(-\frac{1}{Z_+}\right) - i\pi\right)\log\left(1 - \frac{\mathrm{Re}(x_z)}{Z_+}\right) \\ &- 2i\pi(1 - \theta(-\mathrm{Im}(x_z)))\Big\{\log(\mathrm{Re}(x_z) - Z_-) \\ &- \log(\mathrm{Re}(x_z) - Z_+) - \log(-Z_-) + \log(-Z_+)\Big\}\Bigg) \end{aligned} \tag{37}$$

and

$$Z_{\pm} = \frac{1}{2\left(M_t^2 - s_{b\bar{t}}\, s_{\bar{b}t}/s_{b\bar{b}}\right)} \left(M_t^2(\zeta_- + \zeta_+) - \frac{s_{b\bar{t}}\, s_{\bar{b}t}}{s_{b\bar{b}}}(\xi_3 + 1/\xi_4) \right.$$
$$\pm \left[-4 \left(M_t^2 - \frac{s_{b\bar{t}}\, s_{\bar{b}t}}{s_{b\bar{b}}} \right) \left(M_t^2\, \zeta_- \zeta_+ - \frac{s_{b\bar{t}}\, s_{\bar{b}t}}{s_{b\bar{b}}} \frac{\xi_3}{\xi_4} \right) \right.$$
$$\left. \left. + \left(M_t^2(\zeta_- + \zeta_+) - \frac{s_{b\bar{t}}\, s_{\bar{b}t}}{s_{b\bar{b}}}(\xi_3 + 1/\xi_4) \right)^2 \right]^{1/2} \right) \tag{38}$$

$$\zeta_{\pm} = \frac{s_{t\bar{t}} \pm \left(s_{t\bar{t}} - 4M_t^4 + io_+\right)^{1/2}}{2M_t^2}. \tag{39}$$

References

[1] F. Abe *et al.*, "Observation of top quark production in $\bar{p}p$ collisions," *Phys.Rev.Lett.*, vol. 74, pp. 2626–2631, 1995, hep-ex/9503002. 1

[2] S. Abachi *et al.*, "Observation of the top quark," *Phys.Rev.Lett.*, vol. 74, pp. 2632–2637, 1995, hep-ex/9503003. 1

[3] G. Aad *et al.*, "Observation of a new particle in the search for the Standard Model Higgs boson with the ATLAS detector at the LHC," *Phys.Lett.*, vol. B716, pp. 1–29, 2012, 1207.7214. 1

[4] S. Chatrchyan *et al.*, "Observation of a new boson at a mass of 125 GeV with the CMS experiment at the LHC," *Phys.Lett.*, vol. B716, pp. 30–61, 2012, 1207.7235. 1

[5] M. E. Peskin and D. V. Schroeder, "An Introduction to quantum field theory," 1995. 3

[6] M. Bohm, A. Denner, and H. Joos, "Gauge theories of the strong and electroweak interaction," 2001. 3

[7] N. Kidonakis, "Single top production at the Tevatron: Threshold resummation and finite-order soft gluon corrections," *Phys.Rev.*, vol. D74, p. 114012, 2006, hep-ph/0609287. 5

[8] N. Kidonakis, "Differential and total cross sections for top pair and single top production," 2012, 1205.3453. 5

[9] S. Alekhin, A. Djouadi, and S. Moch, "The top quark and Higgs boson masses and the stability of the electroweak vacuum," 2012, 1207.0980. 6

[10] L. J. Dixon, "Calculating scattering amplitudes efficiently," 1996, hep-ph/9601359. 10

[11] M. E. Peskin, "Simplifying Multi-Jet QCD Computation," 2011, 1101.2414. 10

[12] M. L. Mangano and S. J. Parke, "Multiparton amplitudes in gauge theories," *Phys.Rept.*, vol. 200, pp. 301–367, 1991, hep-th/0509223. 11, 12

[13] R. Kleiss and W. J. Stirling, "Spinor Techniques for Calculating $p\bar{p} \to W^{\pm} \,/\, Z_0$ + Jets," *Nucl.Phys.*, vol. B262, pp. 235–262, 1985. 13

[14] C. Schwinn and S. Weinzierl, "Scalar diagrammatic rules for Born amplitudes in QCD," *JHEP*, vol. 0505, p. 006, 2005, hep-th/0503015. 13

[15] S. Badger, R. Sattler, and V. Yundin, "One-Loop Helicity Amplitudes for $t\bar{t}$ Production at Hadron Colliders," *Phys.Rev.*, vol. D83, p. 074020, 2011, 1101.5947. 13, 70

[16] G. 't Hooft and M. Veltman, "Regularization and Renormalization of Gauge Fields," *Nucl.Phys.*, vol. B44, pp. 189–213, 1972. 14

[17] S. Weinzierl, "Equivariant dimensional regularization," 1999, hep-ph/9903380. 14

[18] Z. Kunszt, A. Signer, and Z. Trocsanyi, "One loop helicity amplitudes for all $2 \to 2$ processes in QCD and N=1 supersymmetric Yang-Mills theory," *Nucl.Phys.*, vol. B411, pp. 397–442, 1994, hep-ph/9305239. 15

[19] A. Signer and D. Stockinger, "Using Dimensional Reduction for Hadronic Collisions," *Nucl.Phys.*, vol. B808, pp. 88–120, 2009, 0807.4424. 15, 26, 27

[20] M. Beneke and V. A. Smirnov, "Asymptotic expansion of Feynman integrals near threshold," *Nucl.Phys.*, vol. B522, pp. 321–344, 1998, hep-ph/9711391. 15

[21] B. Jantzen, "Foundation and generalization of the expansion by regions," *JHEP*, vol. 1112, p. 076, 2011, 1111.2589. 15

[22] R. K. Ellis and G. Zanderighi, "Scalar one-loop integrals for QCD," *JHEP*, vol. 0802, p. 002, 2008, 0712.1851. 17

[23] F. Bloch and A. Nordsieck, "Note on the Radiation Field of the electron," *Phys.Rev.*, vol. 52, pp. 54–59, 1937. 19, 24

[24] T. Kinoshita, "Mass singularities of Feynman amplitudes," *J.Math.Phys.*, vol. 3, pp. 650–677, 1962. 19, 24

[25] T. Lee and M. Nauenberg, "Degenerate Systems and Mass Singularities," *Phys.Rev.*, vol. 133, pp. B1549–B1562, 1964. 19, 24

[26] A. Sirlin, "Theoretical considerations concerning the Z0 mass," *Phys.Rev.Lett.*, vol. 67, pp. 2127–2130, 1991. 23

[27] A. Sirlin, "Observations concerning mass renormalization in the electroweak theory," *Phys.Lett.*, vol. B267, pp. 240–242, 1991. 23

[28] M. Beneke and V. M. Braun, "Heavy quark effective theory beyond perturbation theory: Renormalons, the pole mass and the residual mass term," *Nucl.Phys.*, vol. B426, pp. 301–343, 1994, hep-ph/9402364. 23

[29] I. I. Bigi, M. A. Shifman, N. Uraltsev, and A. Vainshtein, "The Pole mass of the heavy quark. Perturbation theory and beyond," *Phys.Rev.*, vol. D50, pp. 2234–2246, 1994, hep-ph/9402360. 23

[30] M. Beneke, "A Quark mass definition adequate for threshold problems," *Phys.Lett.*, vol. B434, pp. 115–125, 1998, hep-ph/9804241. 23, 24, 77

[31] Z. Kunszt and D. E. Soper, "Calculation of jet cross-sections in hadron collisions at order α_s^3," *Phys.Rev.*, vol. D46, pp. 192–221, 1992. 26, 31

[32] S. Catani and M. Seymour, "A General algorithm for calculating jet cross-sections in NLO QCD," *Nucl.Phys.*, vol. B485, pp. 291–419, 1997, hep-ph/9605323. 26, 30, 31, 33, 34, 87

[33] J. C. Collins, D. E. Soper, and G. F. Sterman, "Heavy Particle Production in High-Energy Hadron Collisions," *Nucl.Phys.*, vol. B263, p. 37, 1986. 28

[34] J. C. Collins, D. E. Soper, and G. F. Sterman, "Factorization of Hard Processes in QCD," *Adv.Ser.Direct.High Energy Phys.*, vol. 5, pp. 1–91, 1988, hep-ph/0409313. 28

[35] P. M. Nadolsky, H.-L. Lai, Q.-H. Cao, J. Huston, J. Pumplin, *et al.*, "Implications of CTEQ global analysis for collider observables," *Phys.Rev.*, vol. D78, p. 013004, 2008, 0802.0007. 29

[36] A. Martin, W. Stirling, R. Thorne, and G. Watt, "Parton distributions for the LHC," *Eur.Phys.J.*, vol. C63, pp. 189–285, 2009, 0901.0002. 29, 94

[37] A. Guffanti, "NNPDF2.1: Including heavy quark mass effects in NNPDF fits," *AIP Conf.Proc.*, vol. 1369, pp. 21–28, 2011. 29

[38] W. Giele and E. N. Glover, "Higher order corrections to jet cross-sections in $e^+ e^-$ annihilation," *Phys.Rev.*, vol. D46, pp. 1980–2010, 1992. 32

[39] S. Catani, S. Dittmaier, M. H. Seymour, and Z. Trocsanyi, "The Dipole formalism for next-to-leading order QCD calculations with massive partons," *Nucl.Phys.*, vol. B627, pp. 189–265, 2002, hep-ph/0201036. 33, 34, 87

[40] S. Frixione, Z. Kunszt, and A. Signer, "Three jet cross-sections to next-to-leading order," *Nucl.Phys.*, vol. B467, pp. 399–442, 1996, hep-ph/9512328. 33, 38

[41] R. Frederix, S. Frixione, F. Maltoni, and T. Stelzer, "Automation of next-to-leading order computations in QCD: The FKS subtraction," *JHEP*, vol. 0910, p. 003, 2009, 0908.4272. 33, 38

[42] P. Nason, S. Dawson, and R. K. Ellis, "The Total Cross-Section for the Production of Heavy Quarks in Hadronic Collisions," *Nucl.Phys.*, vol. B303, p. 607, 1988. 45

[43] P. Nason, S. Dawson, and R. K. Ellis, "The One Particle Inclusive Differential Cross-Section for Heavy Quark Production in Hadronic Collisions," *Nucl.Phys.*, vol. B327, pp. 49–92, 1989. 45

[44] W. Beenakker, H. Kuijf, W. van Neerven, and J. Smith, "QCD Corrections to Heavy Quark Production in $p\bar{p}$ Collisions," *Phys.Rev.*, vol. D40, pp. 54–82, 1989. 45

[45] W. Beenakker, W. van Neerven, R. Meng, G. Schuler, and J. Smith, "QCD corrections to heavy quark production in hadron hadron collisions," *Nucl.Phys.*, vol. B351, pp. 507–560, 1991. 45

[46] M. L. Mangano, P. Nason, and G. Ridolfi, "Heavy quark correlations in hadron collisions at next-to-leading order," *Nucl.Phys.*, vol. B373, pp. 295–345, 1992. 45

[47] W. Bernreuther, A. Brandenburg, Z. Si, and P. Uwer, "Top quark pair production and decay at hadron colliders," *Nucl.Phys.*, vol. B690, pp. 81–137, 2004, hep-ph/0403035. 45

[48] K. Melnikov and M. Schulze, "NLO QCD corrections to top quark pair production and decay at hadron colliders," *JHEP*, vol. 0908, p. 049, 2009, 0907.3090. 45, 70

[49] J. M. Campbell and R. K. Ellis, "Top-quark processes at NLO in production and decay," 2012, 1204.1513. 45, 97

[50] V. S. Fadin, V. A. Khoze, and A. D. Martin, "Interference radiative phenomena in the production of heavy unstable particles," *Phys.Rev.*, vol. D49, pp. 2247–2256, 1994. 46, 47, 52, 99, 112

[51] K. Melnikov and O. I. Yakovlev, "Top near threshold: All α_s corrections are trivial," *Phys.Lett.*, vol. B324, pp. 217–223, 1994, hep-ph/9302311. 46, 47, 52, 99, 112

[52] A. Denner and S. Dittmaier, "The Complex-mass scheme for perturbative calculations with unstable particles," *Nucl.Phys.Proc.Suppl.*, vol. 160, pp. 22–26, 2006, hep-ph/0605312. 48

[53] R. G. Stuart, "General renormalization of the gauge invariant perturbation expansion near the Z0 resonance," *Phys.Lett.*, vol. B272, pp. 353–358, 1991. 49, 58

[54] A. Aeppli, G. J. van Oldenborgh, and D. Wyler, "Unstable particles in one loop calculations," *Nucl.Phys.*, vol. B428, pp. 126–146, 1994, hep-ph/9312212. 49, 51, 58

[55] G. Bevilacqua, M. Czakon, A. van Hameren, C. G. Papadopoulos, and M. Worek, "Complete off-shell effects in top quark pair hadroproduction with leptonic decay at next-to-leading order," *JHEP*, vol. 1102, p. 083, 2011, 1012.4230. 51

[56] A. Denner, S. Dittmaier, S. Kallweit, and S. Pozzorini, "NLO QCD corrections to WWbb production at hadron colliders," *Phys.Rev.Lett.*, vol. 106, p. 052001, 2011, 1012.3975. 51

[57] A. Denner, S. Dittmaier, S. Kallweit, and S. Pozzorini, "NLO QCD corrections to off-shell top-antitop production with leptonic decays at hadron colliders," 2012, 1207.5018. 51

[58] J. Alcaraz Maestre *et al.*, "The SM and NLO Multileg and SM MC Working Groups: Summary Report," 2012, 1203.6803. 52

[59] A. Chapovsky, V. A. Khoze, A. Signer, and W. J. Stirling, "Nonfactorizable corrections and effective field theories," *Nucl.Phys.*, vol. B621, pp. 257–302, 2002, hep-ph/0108190. 54, 69

[60] M. Beneke, A. Chapovsky, A. Signer, and G. Zanderighi, "Effective theory calculation of resonant high-energy scattering," *Nucl.Phys.*, vol. B686, pp. 205–247, 2004, hep-ph/0401002. 54

[61] M. Beneke, P. Falgari, C. Schwinn, A. Signer, and G. Zanderighi, "Four-fermion production near the W pair production threshold," *Nucl.Phys.*, vol. B792, pp. 89–135, 2008, 0707.0773. 54

[62] P. Falgari, P. Mellor, and A. Signer, "Production-decay interferences at NLO in QCD for t-channel single-top production," *Phys.Rev.*, vol. D82, p. 054028, 2010, 1007.0893. 54, 56, 74, 77, 82, 97, 110, 125

[63] P. Falgari, F. Giannuzzi, P. Mellor, and A. Signer, "Off-shell effects for t-channel and s-channel single-top production at NLO in QCD," *Phys.Rev.*, vol. D83, p. 094013, 2011, 1102.5267. 54, 56, 82, 97, 110

[64] W. Beenakker, F. A. Berends, and A. Chapovsky, "Radiative corrections to pair production of unstable particles: results for $e^+ e^- \to$ four fermions," *Nucl.Phys.*, vol. B548, pp. 3–59, 1999, hep-ph/9811481. 58

[65] J. M. Campbell, R. Ellis, and F. Tramontano, "Single top production and decay at next-to-leading order," *Phys.Rev.*, vol. D70, p. 094012, 2004, hep-ph/0408158. 70, 87

[66] T. Hahn, "The CUBA library," *Nucl.Instrum.Meth.*, vol. A559, pp. 273–277, 2006, hep-ph/0509016. 94

[67] S. D. Ellis and D. E. Soper, "Successive combination jet algorithm for hadron collisions," *Phys.Rev.*, vol. D48, pp. 3160–3166, 1993, hep-ph/9305266. 94

[68] S. Catani, Y. L. Dokshitzer, M. Seymour, and B. Webber, "Longitudinally invariant K_t clustering algorithms for hadron hadron collisions," *Nucl.Phys.*, vol. B406, pp. 187–224, 1993. 94

[69] M. Beneke, P. Falgari, S. Klein, J. Piclum, C. Schwinn, *et al.*, "Inclusive top-pair production phenomenology with TOPIXS," *JHEP*, vol. 1207, p. 194, 2012, 1206.2454. 97

[70] T. Aaltonen *et al.*, "Evidence for a Mass Dependent Forward-Backward Asymmetry in Top Quark Pair Production," *Phys.Rev.*, vol. D83, p. 112003, 2011, 1101.0034. 112

[71] V. M. Abazov *et al.*, "Forward-backward asymmetry in top quark-antiquark production," *Phys.Rev.*, vol. D84, p. 112005, 2011, 1107.4995. 112

[72] J. H. Kuhn and G. Rodrigo, "Charge asymmetry of heavy quarks at hadron colliders," *Phys.Rev.*, vol. D59, p. 054017, 1999, hep-ph/9807420. 113

[73] T. Aaltonen *et al.*, "Combination of the top-quark mass measurements from the Tevatron collider," *Phys.Rev.*, vol. D86, p. 092003, 2012, 1207.1069. 115